PART III.

INTER-DEPARTMENTAL RESEARCH ACTIVITIES – SELECTED HIGHLIGHTS

Design of Precipitation in Lean Maraging-TRIP Steels

J. Millán[1], S. Sandlöbes[1], T. Hickel[2], D. Ponge[1], P. Choi[1], J. Neugebauer[2], D. Raabe[1]

[1] Department of Microstructure Physics and Alloy Design
[2] Department of Computational Materials Design

"Maraging steels" combine ultrahigh strength and high fracture toughness by hardening an essentially carbon-free martensitic matrix with nano-sized inter-metallic precipitates. Typical applications are in the fields of aircrafts and aerospace, where maraging steels meet the high requirements of minimum weight while ensuring high reliability [1]. The formation of a high volume fraction of homogeneously distributed precipitates such as Ni_3Ti or Ni_3Mo requires alloying with a high amount of expensive Ni, typically in the range of 18 wt.%.

Our approach is to combine a maraging treatment with Fe−Mn alloys and a significantly reduced Ni-content to obtain an alloy combining ultrahigh strength and sufficient ductility. As reported elsewhere [2] remarkable improvement of toughness and ductility in Fe-Mn alloys can be obtained via a partial re-austenitization.

Choosing a high Mn content of 6-12 wt.% allows reducing the Ni content (and if necessary other elements) and supports the formation of precipitates by providing a high supersaturation.

Possible intermetallic phases are NiMn or the Heusler phase Ni_2MnAl. NiMn can form with B2 and Ni_2MnAl with either $L2_1$ or B2 structure. As both structures are based on the bcc lattice, coherency between matrix and particles is possible. This ensures low nucleation energy and favors a very fine distribution in the bcc matrix by homogeneous nucleation.

To design lean maraging TRIP steels, which are reinforced by these precipitates, we employ high resolution experimental characterization methods in combination with *ab initio* theoretical calculations.

The *ab initio* calculations were performed to determine the Al content that promotes the precipitation of either NiMn or Ni_2MnAl. To this aim we determined the lattice constants and formation enthalpies of the two competing phases, including the dependence on the individual alloying elements. Fig. 1 reveals that for incoherently incorporated precipitates (no constraints of the lattice constant, dashed line) the B2-NiMn phase is preferred up to 4.2 at.% (2.1 wt.%) Al content. In the case of coherency (lattice constant constraint to the matrix, solid line) the B2-NiMn phase is preferred up to 2.4 at.% (1.2 wt.%) Al content. At higher Al alloying the precipitation of $L2_1$-Ni_2MnAl is favoured.

Based on these theoretical predictions we produced two different steels: Steel L-Al (0.01C−12Mn−2Ni−0.14Al−1Ti−1Mo wt.%) has a low Al content and steel H-Al (0.01C−12Mn−3Ni−1.28Al wt.%) an Al content above the critical value determined by the *ab initio* prediction. Both steels were homogenized, quenched and aged (450°C for 65 h).

TEM and APT analyses of the steels reveal the existence of nano-sized precipitates in the α' martensite in both alloys, Fig. 2. In the APT images iso-concentration surfaces at 10 at.% Ni are displayed in green to distinguish between matrix and precipitates. Ni and Mn atoms are shown by green and yellow dots respectively. Fe atoms are omitted in these reconstructions. Both characterization methods show that precipitates of different sizes and dispersion are formed in the different steels.
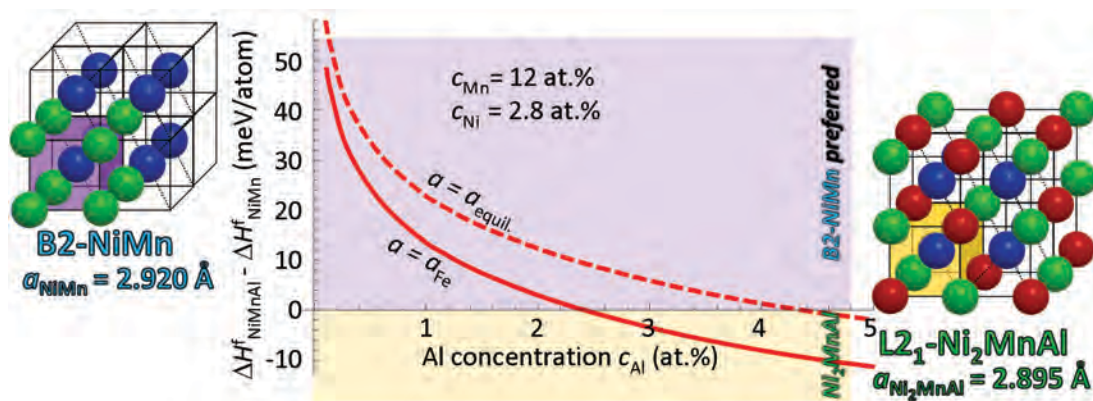
Fig. 1: *Difference of formation enthalpies of both phases. The concentrations of Mn and Ni are fixed, the concentration of Al is varied. Solid line: Precipitates are forced to the lattice constant of Fe (2.835 Å). Dashed line: Precipitates adopt the equilibrium lattice constants of NiMn or Ni_2MnAl.*
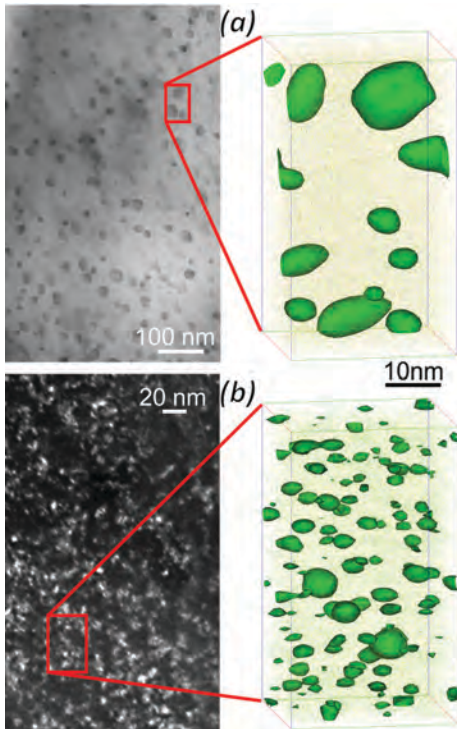
Fig. 2: *TEM images (left side) and APT reconstructions (right side) showing size and spatial distribution of the nano-sized precipitates in the martensitic matrix after aging at 450°C for 65 hours. (a) steel L-Al (0.14 wt.% Al), (b) steel H-Al (1.28 wt.% Al).*

In steel H-Al with higher Al content (1.28 wt.% Al) the precipitates (Ø 3-5 nm) are much finer than in steel L-Al (Ø 10-20 nm) and the number density of precipitates is 18-times higher in steel H-Al.

Selected area diffraction in the TEM investigation revealed that the structure of the precipitates in steel L-Al is B2. In contrast, in steel H-Al both structures, namely, L2$_1$ and B2 are observed.

The chemical composition of the precipitates in both steels was analyzed by APT. The average concentrations over all precipitates in the analyzed sample volumes were determined by means of the proximity histogram method. Fig. 3 shows the resulting concentration profiles between precipitates and martensitic matrix in L-Al (Fig. 3(a)), and H-Al (Fig. 3(b)). From these analyses it is evident that the precipitates have different Mn and Al concentrations: The precipitates formed in steel L-Al have an average chemical composition of 50 at.% Ni, 35 at.% Mn, 2.5 at.% Al and 5 at.% Ti. In steel H-Al precipitates with average concentrations of 50 at.% Ni, 20 at.% Mn and 20 at.% Al are formed. The stoichiometric relationships of the precipitates indicate that in L-Al NiMn particles (with substitution by Ti and Al) are precipitated, in H-Al Ni$_2$MnAl precipitates are formed.

The combined TEM and APT analysis reveals that low Al alloying (0.14 wt.% Al in L-Al) leads to precipitation of NiMn with B2 structured precipitates and high Al alloying (1.28 wt.% Al in H-Al) yields the formation of Ni$_2$MnAl precipitates with L2$_1$ structure as predicted by *ab initio* simulations. Hardness measurements revealed a much stronger hardening effect in the steel H-Al which contains Ni$_2$MnAl precipitates.

We have, therefore, demonstrated that the combination of *ab initio* calculations and high resolution microstructure characterization by TEM and APT enables the design of advanced lean maraging TRIP steels with tailored properties.

References

1. Malakondaiah, G.; Srinitlas, M.; Rama Rao, P.: Prog. Mater. Sci. 42 (1997) 209.

2. Dmitrieva, O.; Ponge, D.; Inden, G.; Millán, J.; Sietsma, J.; Choi, P.; Raabe, D.: Acta Mater. 59 (2011) 364.
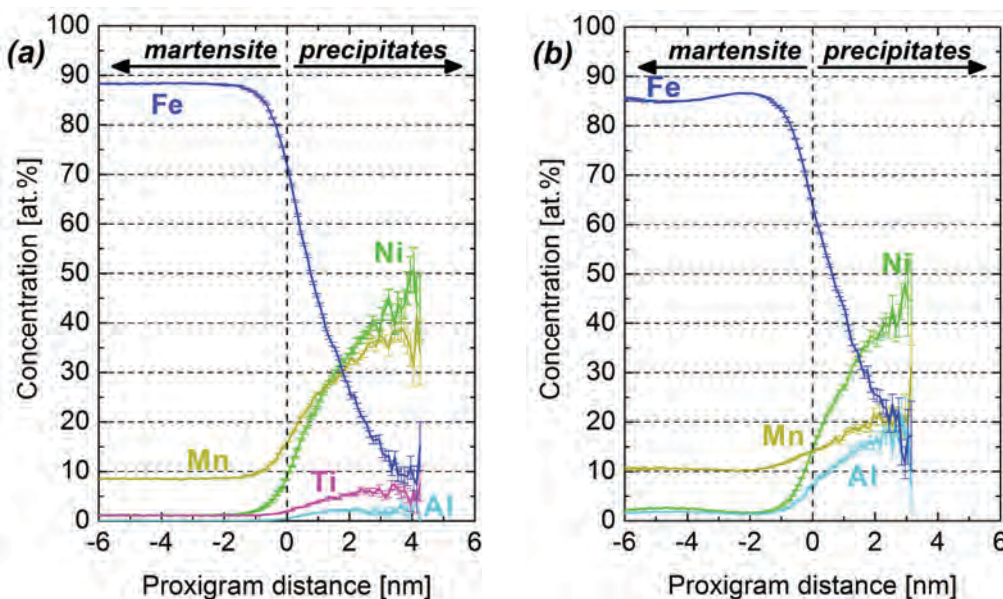
Fig. 3: *Average chemical composition gradients between martensitic matrix and precipitates as calculated by the proximity histogram method. Aged alloys at 450°C for 65 hours; (a) steel L-Al (0.14 wt.% Al), (b) steel H-Al (1.28 wt.% Al).*

Scale-Bridging Analysis and Design of Novel Mn–C–Al Weight-Reduced Steels

H. Springer, J.B. Seol, I. Gutierrez, D. Raabe

Department of Microstructure Physics and Alloy Design

A novel class of steels containing high amounts of manganese (Mn), aluminium (Al) and carbon (C) – also referred to as 'Triplex' steels – offers a low mass density, improved corrosion resistance, high strength and excellent ductility in comparison to conventional steels for structural engineering applications. Profound changes of their mechanical properties can be achieved via aging of the material. More specific, κ–Al(Fe,Mn)$_3$C carbides were found to precipitate from the mainly austenitic matrix, growing from C-enriched areas most probably formed via spinodal decomposition during quenching [1,2]. Further development of high strength Mn–C–Al weight reduced steels necessarily involves the investigation and understanding of both fundamental phenomena as well as more application related parameters. The use of high-throughput bulk combinatorial design methods together with high resolution characterisation techniques applied in a scale-bridging approach enables a rapid maturation of such nano-particle hardened steels. First observations revealed that some of the observed hardening phenomena were highly composition dependent. Determining the optimum material composition and microstructural state by use of conventional metallurgical synthesis and processing methods, however, is often too time-consuming for probing a wider range of chemical compositions each combined with a large matrix of thermomechanical routes. For this reason a systematic but accelerated screening of different compositions and heat treatment variants of such steels was introduced.

The novel bulk rapid alloy prototyping (RAP) approach [3] enables for the first time a systematic and simultaneous evaluation of the compositional and thermomechanical trends associated with the change in the Al content for a group of 30Mn–1.2C (wt.%) Triplex steels. Five alloy compositions each

exposed to nine different heat treatments were synthesized, processed and evaluated within 35 hours. The mechanical properties of these 45 different material conditions are shown in Fig. 1 in terms of the yield strength (a), ultimate tensile strength (b), total elongation under tensile load (c), and indentation hardness (d). Pronounced trends in the mechanical behaviour of the materials can be clearly distinguished, associated with the changes in chemical composition and aging parameters: Without the addition of Al the most favourable mechanical properties are obtained for the as-homogenised state. As with Mn–C TWIP steels exhibiting similar properties, the embrittlement during aging can be related to the formation of coarse pearlitic particles on the grain boundaries [4]. High amounts of Al (~8 wt.%), on the other hand, show pronounced strengthening during aging, related to the formation and growth of κ carbides. Alloys with intermediate Al concentrations (about 2 to 6 wt.%) do not reveal mechanical properties on the same level compared to the aforementioned extreme cases in their respective optimal conditions. On the other hand, a much
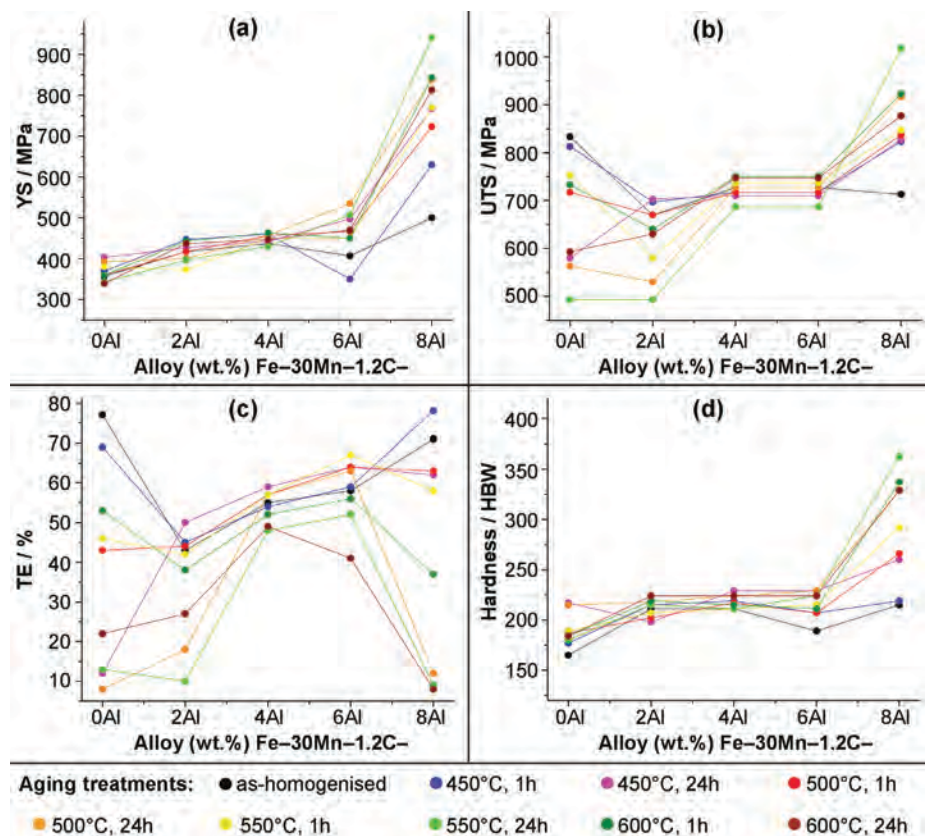

Fig. 1: *Overview of the mechanical properties of 30Mn–1.2C (wt.%) based steels obtained by high throughput bulk combinatorial screening as a function of Al concentration and applied ageing treatment: (a) Yield stress (YS), (b) ultimate tensile stress (UTS), (c) total elongation (TE), (d) hardness.*
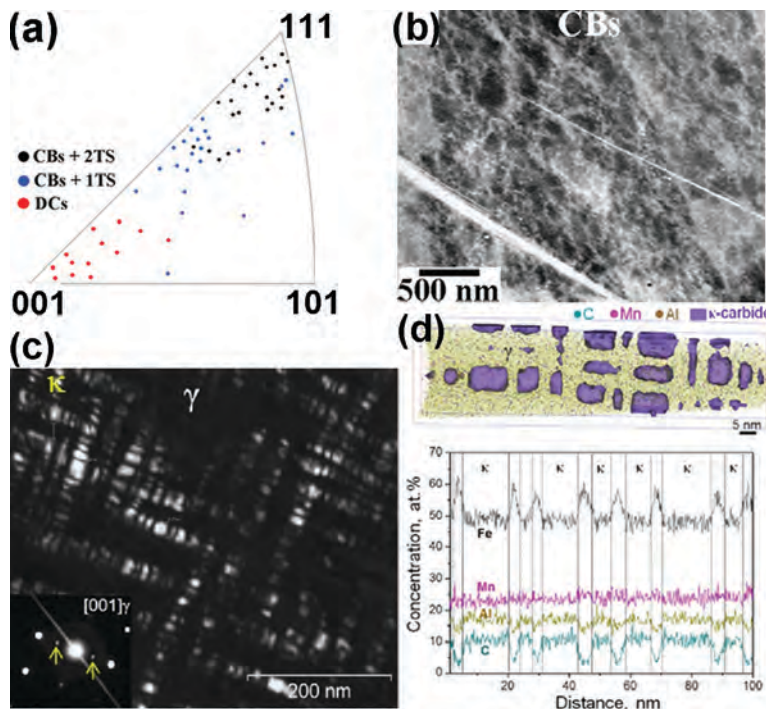
Fig. 2: *High resolution characterisation of a 30Mn–1.2C–2Al (wt.%) steel: (a) Crystallographic orientation dependence of the deformation microstructure; CB: cell blocks, TS twinning system, DC: dislocation cells, (b) ECCI image of CBs, (c) DF-TEM image of nano-sized carbides, (d) 3D-APT reconstructed volume and 1D composition profile of κ carbides.*

true strain, the average cell block size in <111> and <112> oriented grains is 220 ± 50 nm, Fig. 2(b).

Additional nano-structural investigations via TEM and APT give insight into the structural and chemical interactions between matrix and precipitated κ-carbides within Mn–C–Al light weight steels. Fig. 2(c) shows a dark field TEM micrograph and the corresponding selected area diffraction (SAD) pattern of an Fe–30Mn–1.2C–8Al (wt. %) alloy after aging of 600 ºC for 24 h followed by tensile deformation to 15 %. The resultant microstructure is composed of an austenitic matrix containing κ-carbides of cuboidal shape (size ~20 × 10 nm) surrounded by micro- and nano-channels. SAD of the [001]γ zone axis confirmed that the κ-carbides have a cube-cube orientation relationship with the matrix, namely [100]γ//[100]κ, similar to that of γ/γ' interfaces in nickel-base superalloys. Clear {100} superlattice reflections of the κ-phase are caused by an ordering process of interstitial C at the body centered site of the κ-phase with an L'1$_2$ type crystal structure. Fig. 2(d) displays a reconstructed APT map of C (blue) for the aging treated sample and the corresponding iso-surface (purple) of 0.9 at.% C. Both the C-enriched features and the nano-channels as shown in the TEM image in Fig. 2(c) can be detected in the APT data. Using 1-D composition profiles, the partitioning of solutes to different phases can be quantified in terms of an enrichment factor, ε = (at.% in κ-phase) / (at.% in austenite). The ε value for Mn is substantially lower than for Al and C. It seems that Mn atoms are energetically stable inside either the intermetallic κ or austenite phase. This means that the partitioning of solutes to κ-carbides can be controlled by the abutting phase [8]. APT results suggest that during the decomposition of austenite into κ, both matrix (austenite) and product phase (κ-carbide) compete for Mn.

smaller influence of the aging parameters on the tensile behaviour can be observed in these cases.

The corresponding understanding of the underlying strain hardening mechanisms of Fe–Mn–Al–C alloys requires investigating the microstructure using high resolution characterisation techniques (Fig. 2). The application of the recently developed SEM/EBSD-based ECCI set-up [5] to the characterisation of deformation structures of high-Mn lightweight steels has brought new insights into the respective strain hardening mechanisms [6,7]. Fig. 2(a) shows the grain orientation dependence of the deformation structure in a Fe–30Mn–1.2C–2Al (wt.%) steel, tensile-deformed to 0.3 true strain with a strength of 1.15 GPa. Three types of grains can be systematically distinguished: The first group of grains are characterized by a dislocation cell structure with low deformation twinning activity. These grains occupy an area fraction of about 10 % and are oriented close to <001>//TA (tensile axis) within an angular range of about 15° (red dots in Fig. 2(a)). The average cell size in these grains is 180 ± 40 nm and their shapes depend on the number of slip systems activated. The second group represents grains that contain combined dislocation and twin substructures formed by dislocation cell blocks and lamellar twin structures. They reach about 30 area% and have <112>//TA orientation (±15°; blue dots in Fig. 2(a)). The third group contains grains which build up complex substructures consisting of dislocation cell blocks and multiple-twin substructures. These grains, which are oriented close to <111>//TA with about 15° scatter (black dots in Fig. 2(a)), are the most frequent grains with about 60 area %. At 0.3

References

1. Frommeyer, G.; Brüx, U.: Steel Res. Int. 77 (2006) 633.
2. Choo, W.K.; Kim, J.H.; Yoon, J.C.: Acta Mater. 45 (1997) 4877.
3. Springer, H.; Raabe, D.: Acta Mater. 60 (2012) 4950.
4. Bouaziz, O. ; Allain, S. ; Scott, C.P. et al. : Curr. Opin. Solid State Mater. Sci. 15 (2011) 141.
5. Gutierrez-Urrutia, I. ; Zaefferer, S.; Raabe, D.: Scr. Mater. 61 (2009) 737.
6. Gutierrez-Urrutia, I. ; Raabe, D.: Acta Mater. 59 (2011) 6449.
7. Gutierrez-Urrutia, I. ; Raabe, D.: Acta Mater. 60 (2012) 5791.
8. Seol, J.B.; Raabe, D.; Choi, P.; Park, H.S.; Kwak, J.H.; Park, C.G.: Scr. Mater. 2012, *in press*, DOI 10.1016/j.scriptamat.2012.08.013.

Nano-Diffusion Controls Macro-Deformation of High Strength Steels

S. Sandlöbes[1], T. Hickel[2], A. Dick[2], I. Bleskov[2], J. Neugebauer[2], D. Raabe[1]

[1] Department of Microstructure Physics and Alloy Design
[2] Department of Computational Materials Design

Advanced structural materials can have extraordinary mechanical properties due to the interplay of deformation processes on different length scales. During a transformation induced plasticity (TRIP) the atomic structure adapts to an external strain by performing a martensitic phase transformation. Alternatively, materials showing twinning induced plasticity (TWIP) make use of twin boundary formation. In both cases the material responds to plastic deformation by locally adapting the sequence of atomic layers in the region affected. This is only possible, if the stacking fault energies (SFE) are sufficiently low. Changing the chemical composition of a material is the most suitable strategy for adjusting the SFE and in this way purposely designing materials with tailored mechanical properties. Particularly promising are austenitic steels, in which the face-centred cubic (fcc) crystal structure is stabilized by Mn [1].

Carbon is another element with a high relevance for deformation mechanisms in steels. However, the available experimental investigations on the dependence of the SFE on the carbon content seem to be inconsistent: Previously published transmission electron microscopy (TEM) experiments show only a very slight change of the SFE with the C content in steels [2], whereas XRD experiments suggest a strong increase of the SFE in austenitic steels [3] (Fig. 1). Within this article we argue that this discrepancy is due to nano-diffusion processes (diffusion over a few neighbouring sites) in the vicinity of the stacking fault – a result, which was only achievable by combining an in-depth theoretical understanding with new ideas for *in situ* TEM experiments.

Ab initio methods are considered to be particularly suitable if accurate chemical trends for structural quantities like the SFE are needed [4]. We have therefore investigated the role of interstitial carbon, performing both supercell calculations that explicitly contain stacking faults as well as bulk calculations used as input for an approximate (ANNNI = Axial Next-Nearest Neighbour Ising) model [5]. A large number of concentrations and configurations of C atoms has been considered. All these calculations are remarkably consistent with each other and in particular with those experiments that show an enormous increase of the SFE with the carbon content (Fig. 1).

The *ab initio* calculations shown in Fig. 1 are performed for a homogenous C distribution throughout the sample, i.e., ignore possible changes of the local chemistry due to the formation of the stacking fault (Fig. 2a). This assumption is well justified in the undeformed state and will prevail after the formation of stacking faults, if C remains trapped in the octahedral sites and is dragged with the lattice during the diffusionless rearrangement of the metal atoms. This is a realistic scenario at room temperature, since at these temperatures the diffusion of C in fcc Fe is known to be negligible. To estimate the local gradients in the carbon chemical potential induced by forming an intrinsic stacking fault (ISF) we have performed supercell calculations that contain such a
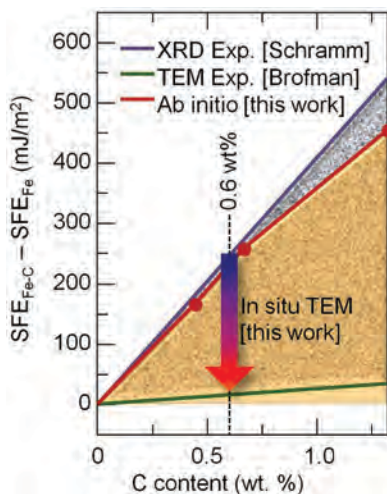
Fig. 1: *Dependence of the stacking fault energy (SFE) in steels on the C content. The experimental range of values (textured area) is constraint by XRD experiments (blue line, [3]) and TEM experiments (green line, [2]). Our ab initio results for the Fe-C system yield at T = 0 K a strong increase of the SFE with C content (red line), but imply a reduction of the SFE with increasing temperature (orange area). The arrow indicates the concentration for which in situ (temperature dependent) TEM experiments have been performed in this work. Within the displayed range a reduction of the SFE by 30-40 % has been directly observed.*
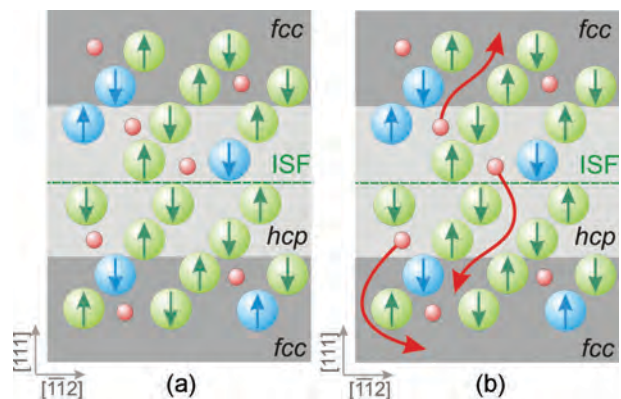
Fig. 2: *Two scenarios for the distribution of C in the vicinity of an intrinsic stacking fault (ISF). (a): C is homogeneously distributed, (b): nano-diffusion of C out of the hcp region occurs.*
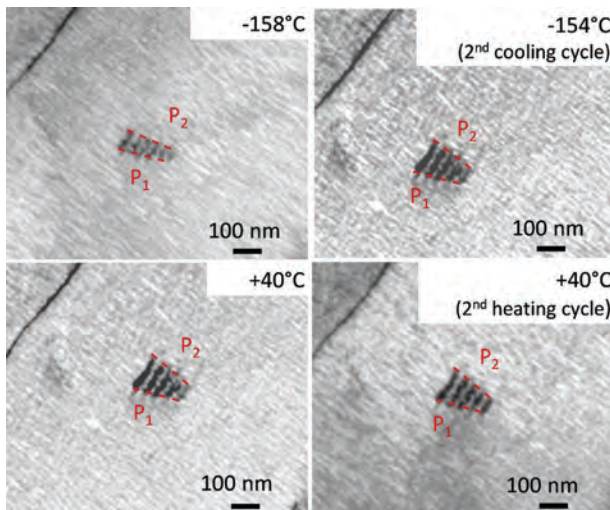
Fig. 3: *Change of the dissociation width in Fe-22Mn-0.6C during in-situ cooling and heating in the TEM. The oscillation contrast of the stacking fault of the pre-deformed sample (0.5 % eng. strain) was obtained under adjusted diffraction conditions. During the first cooling-heating cycle (left micrographs) the dissociation width of the partial dislocations has increased. A further cooling-heating cycle (right micrographs) did not cause significant changes in the stacking fault width.*

defect. The calculations clearly show that there is a significant thermodynamic driving force to out-diffuse C from the local hcp region that is formed next to an ISF (Fig. 2b). This out-segregation of solute elements away from the defect is opposite to the conventional well-known Suzuki effect. We therefore termed it anti-Suzuki effect. This effect sets in when the C atoms become mobile, i.e., at sufficiently high temperatures. The C depleted SF-region, as a consequence, has an energy similar to a steel with low/zero C content.

The above described mechanisms become crucial when probing such a situation by electron optical methods: The irradiation of solids by an electron beam via TEM induces scattering events, which can result in an energy exchange between electrons and matter. The influence on possible temperature-activated mechanisms due to the interaction with the electron beam is, however, typically not taken into account when measuring SFEs. We argue that depending on the TEM set-up and the investigated steel these scattering events can locally yield diffusion of C during the measurement, allowing them to follow the strong thermodynamic driving force identified by the calculations. In contrast, XRD measurements generally do not lead to enhanced diffusion. Together with our *ab initio* data this nicely explains why TEM (where nano-diffusion is expected to be active) and XRD (where it is inactive) show the qualitative differences displayed in Fig. 1.

To verify that the electron beam can have a dramatic effect on C diffusion during observation, we performed *in situ* cooling-heating experiments in the TEM. Before starting the measurement we cooled down the sample using liquid nitrogen in a TEM cooling holder. In this way the mobility of C is

in comparison to a room temperature measurement additionally limited, which should reduce the impact of scattering events with the electron beam. Even with this setup the C diffusion cannot be completely suppressed, yielding an uncontrollable reduction of the SFE already at this stage. However, the effect became much more pronounced, when the sample was *in situ* heated to 40 °C during the investigation of a region of interest, i.e. partial dislocations that form a SF, while keeping the same position and orientation. We find in all our *in situ* experiments that the dissociation width of the partial dislocations bounding the stacking fault then increases by about 40-60 % during heating (see Fig. 3). This corresponds to a decrease of the SFE by 30-40 % (lower part of the arrow in Fig. 1) The observation is consistent with the theoretical interpretation: The electron beam activates local C diffusion out of the stacking fault thus enabling the C atoms in the ISF to diffuse to the neighbouring fcc phase during the TEM investigation.

In principle, a large number of further concepts could be used to explain this change of the SFE – all of which have been excluded in additional investigations. A thermodynamic explanation was for example ruled out by *ab initio* based calculations, showing that the pure temperature dependence would yield an increase rather than a decrease of the SFE with heating. Most important is, however, that thermodynamic as well as other concepts would result into a reversible behaviour. In contrast to this, all our *in situ* TEM experiments for which we have performed additional cooling-heating cycles consistently show no significant further change of the SFE after the first cycle (Fig. 3).

We conclude from our combined *ab initio* simulations and *in situ* TEM measurements that a nano-diffusion of C atoms in the region of the stacking fault (anti-Suzuki effect) is responsible for the observed change of the local SFE. Combining DFT calculations and TEM measurements reveals that only the local carbon content plays a decisive role for the local SFE. This result provides direct insight into atomic scale mechanisms that allow one to tailor diffusion and segregation effects by appropriate alloying and thermal treatment, a prerequisite to design microstructures with adaptive deformation mechanisms.

References

1. Frommeyer, G.; Brüx, U.; Neumann, P.: ISIJ Int. 43 (2003) 438.

2. Brofman, P.J.; Ansell, G.S.**:** Metall. Trans. 9A (1978) 879.

3. Schramm, R.E.; Reed, R.P.: Metall. Trans. 6A (1975) 1345.

4. Gebhardt, T.; Music, D.; Ekholm, M.; Abrikosov, I.A.; Vitos, L.; Dick, A.; Hickel, T.; Neugebauer, J.; Schneider, J.M.: J. Phys.: Condens. Matter 23 (2011) 246003.

5. Abbasi, A.; Dick, A.; Hickel, T.; Neugebauer, J.: Acta Mater. 59 (2011) 3041.

Atomic Scale Analysis of the Origin of the Strength of Pearlite

Y.J. Li [1,2], S. Goto [3], C. Borchers [2], P. Choi [1], M. Herbig [1], S. Zaefferer [1], A. Kostka [1],
J. von Pezold [4], A. Nematollahi [4], B. Grabowski [4], J. Neugebauer [4],
R. Kirchheim [1,2], D. Raabe [1]

[1] Department of Microstructure Physics and Alloy Design,
[2] Institute for Materials Physics, Georg-August-University of Göttingen, Germany,
[3] Department of Materials Science and Engineering, Faculty of Engineering and Resource Science, Akita University, Japan,
[4] Department of Computational Materials Design

Pearlitic steel subjected to heavy cold-drawing exhibits tensile strengths above 6 GPa [1] being the strongest structural bulk alloy known. Despite great potential for engineering applications (*e.g.*, suspension bridge cables, tire cords, springs), the correlation between the enormous strength and the microstructure is a matter of debate. The relevant mechanisms include the refinement of lamellar spacing, cementite decomposition, and formation of nanoscaled dislocation substructures. To evaluate these mechanisms it is necessary to precisely assess the concentration change of C atoms in ferrite and cementite upon cold-drawing. We have studied the redistribution of alloying elements and the spacing between phase and subgrain boundaries using atom probe tomography (APT) and transmission electron microscopy (TEM) [2]. In parallel, we have conducted first principles simulations to elucidate the physical origin of the extraordinarily high C concentration in ferrite [3]. This hybrid experimental-theoretical approach is a solid basis for revealing the origin of the strength of pearlite.

Our experimental results clearly show that the C concentration in cementite decreases with decreasing thickness of the cementite lamellae (Fig. 1a). This indicates the important role of dislocation drag in the decomposition of cementite which can be explained by an increasing interface-to-volume ratio [2]. Our first principles calculations support this statement. Fig. 1b shows that thermodynamics alone cannot account for the high C concentration in ferrite, leaving the dislocation drag as the most probable solution [3]. First theoretical results for dislocation drag are shown in Fig. 2. In particular, we present the potential energy surface of a C atom around a dislocation. This type of energy surface is a powerful tool allowing to investigate the preferential sites and diffusion barriers of an interstitial atom (here C interstitial) in a host matrix (here Fe). Fig. 2 shows that in the dislocation core region an energy 'tunnel' opens (indicated by the arrow) which corresponds to a lower energy level than in the bulk. This means that C atoms are more stable in the core region and can thus be trapped by a moving dislocation. This is a possible explanation for dislocation drag and thus, in general, our results support C enrichment of ferrite by dislocation drag.

Another important question we could recently clarify is: what generates high strengths at strains >3.5? Increasing strength at strains from 0 to 3.5 is attributed to the refinement of interlamellar spacing
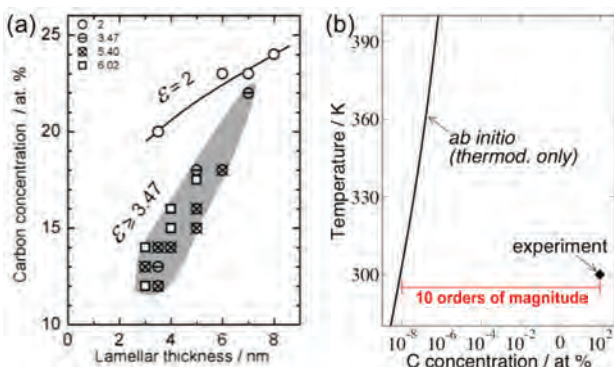
Fig. 1: *(a) Experimental C concentration in cementite as a function of the lamellar thickness. (b) Ab initio temperature dependence of C concentration based on a thermodynamic assessment [3], i.e., excluding the drag effect of dislocations. The difference to the experimental concentration is 10 orders of magnitude.*
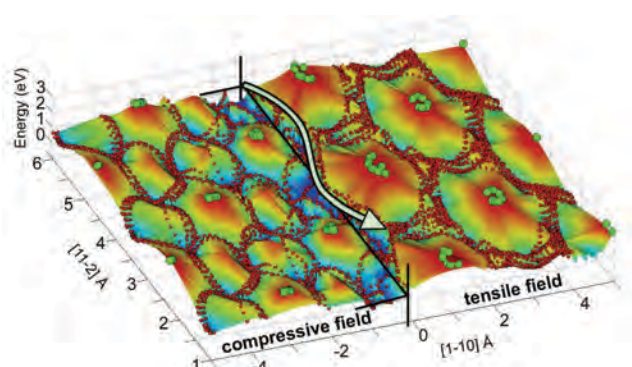
Fig. 2: *Energy surface for a C atom diffusing in an edge dislocation in bcc Fe obtained with empirical potentials. The green spheres indicate Fe atoms from several layers projected onto a single plane. The red dots indicate the diffusion paths of a C atom from one interstitial site to the neighbouring.*
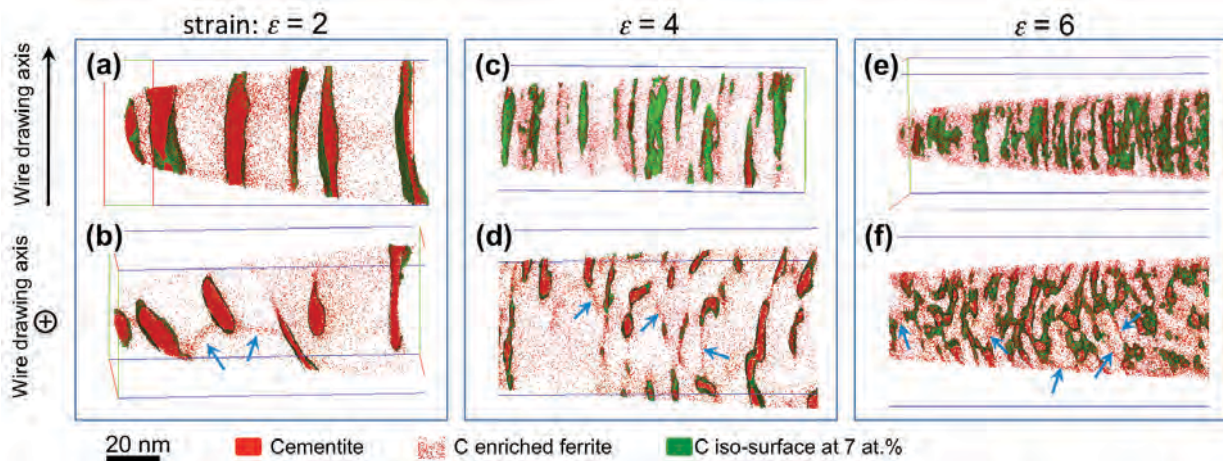
Fig. 3: *APT results for true drawing strains 2 (a,b), 4 (c,d), and 6 (e,f) and for longitudinal (a,b,c) and cross-sectional (d,e,f) views of drawn wires. Blue arrows mark some of the (sub)grain boundaries containing excess C.*

and an increasing C concentration in the ferritic regions. At ε > 3.5, however, the C concentration saturates [2], while interfaces gradually lose their

Fig. 4: *Nanoscaled dislocation substructures characterized by (a) APT and (b) TEM (bright-field) in the transverse cross-section of a cold-drawn (ε = 6) hypereutectoid pearlitic wire after annealing at 350°C for 0.5h. The green-colored iso-concentration surfaces for 7 at.% C show spheroidization of the originally lamellar cementite during annealing. A dislocation array forming a low-angle grain boundary (LAGB) is marked.*

strengthening effect due to decomposition and fragmentation of cementite. Fig. 3 shows that in this high strain regime the subgrain size decreases strongly with strain (see blue arrows) providing a possible explanation for the high strength. To support this statement, APT and TEM observations were performed on the ε = 6 wire after annealing which allows a clearer identification. Fig. 4a indeed demonstrates a high density of subgrains. We can exclude that these subgrains were formed during annealing, as low angle grain boundaries are observed (Fig. 4b) which indicates that recovery rather than recrystallization takes place during annealing, since primary recrystallization would lead to high-angle grain boundaries. The observation also indicates that the dislocation substructures have already been formed during cold drawing and that they contribute to the strength of pearlite at ε > 3.5.

References

1. Li, Y.J.; Choi, P.; Goto, S.; Borchers, C.; Raabe, D.; Kirchheim, R.: Acta. Mater. 60 (2012) 4005.

2. Li, Y.J.; Choi, P.; Borchers, C.; Westerkamp, S.; Goto, S.; Raabe, D.; Kirchheim, R.: Acta. Mater. 59 (2011) 3965.

3. Nematollahi, A.; von Pezold, J.; Neugebauer, J.; Raabe, D.: "Thermodynamics of carbon solubility in ferrite and vacancy formation in cementite in strained pearlite", Acta Mater., *submitted*.

SELECTED HIGHLIGHTS

Phase Formation, Phase Stability and Evolution of the Microstructure in Al-rich Ti−Al

M. Palm[1], N. Engberding[1], F. Stein[1], K. Kelm[2], S. Irsen[3]

[1] Department of Microstructure Physics and Alloy Design / Department of Structure and Nano-/Micromechanics of Materials
[2] German Aerospace Center (DLR), Cologne, Germany
[3] Research center caesar, Bonn, Germany

Ti−Al based alloys comprise a new class of light-weight alloys with outstanding high specific strength, which enables application up to about 800 °C. Alloys are successfully used for the production of exhaust valves, turbo charger rotors and compressor blades. Though consisting out of two inherently brittle intermetallic phases, TiAl + Ti_3Al lamellar microstructures have been designed, which yield sufficient ductility combined with high strength. Because oxidation resistance at high temperatures is still insufficient, Al-rich TiAl alloys have come into focus recently. It has been shown that also in these alloys lamellar TiAl + r-$TiAl_2$ microstructures can be generated [1] by which mechanical properties may improve [2]. However, lacking knowledge about phase formation and phase stability in the Al-rich part of the Ti−Al system hampered any aimed alloy development.

In order to clarify phase formation and stability in the Al-rich part of the Ti−Al system, a couple of Ti-60 at.% Al alloys have been produced by different techniques to generate different initial microstructures. Kinetics were studied by annealing for varying times and different temperatures. Quenched microstructures were analysed by light-optical, scanning electron (SEM), and transmission electron microscopy (TEM) and *in situ* heating and cooling experiments through differential thermal analysis (DTA) and TEM have been performed to verify results obtained on the quenched samples [3].

In Al-rich TiAl, which becomes supersaturated in Al during cooling, two metastable phases, Ti_3Al_5 and h-$TiAl_2$, form (Fig. 1) [4]. Ti_3Al_5 forms instantly on cooling while h-$TiAl_2$ is not present in all as-processed alloys but may only form after a short term anneal, e.g. 900 °C/1 h. That Ti_3Al_5 forms ordered domains within TiAl (Fig. 2) [3,5] while h-$TiAl_2$ is always present as a separate phase, explains the more spontaneous formation of Ti_3Al_5 [3].

On prolonged annealing below the transformation temperature, the Ti_3Al_5 domains coarsen and form a tweed-like Ti_3Al_5 + TiAl microstructure [6]. DTA investigations show that the transformation temperature for the dissolution of Ti_3Al_5 depends on the prior annealing time, which can be explained by increasing interfacial energies through the development of distinct phase interfaces with increasing annealing time [3].
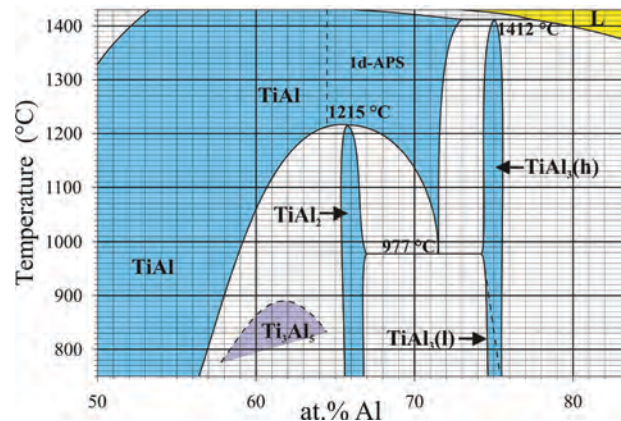
Fig. 1: *Al-rich part of the Ti–Al system showing the stability ranges of TiAl, Ti_3Al_5 and $TiAl_2$ [4].*

The instant formation of the metastable phases can be explained by a crystallographic analysis. A Bärnighausen tree analysis shows that group-subgroup relations exist between the structures of TiAl and Ti_3Al_5 and between TiAl and h-$TiAl_2$, i.e. both transformations are order/disorder transformations, while no such relation does exist for TiAl and r-$TiAl_2$ [7].
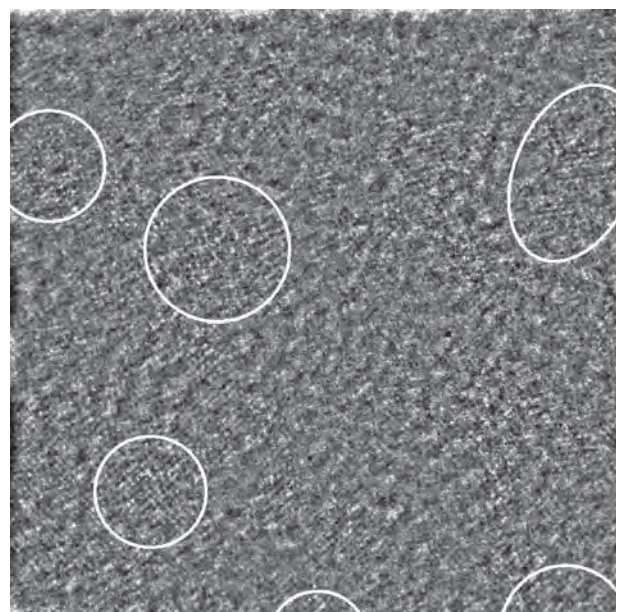
Fig. 2: *Fourier filtered high-resolution [001] TEM image (HRTEM) of as-processed Ti-59.7Al showing local Ti_3Al_5-type ordering (encircled areas) [3].*
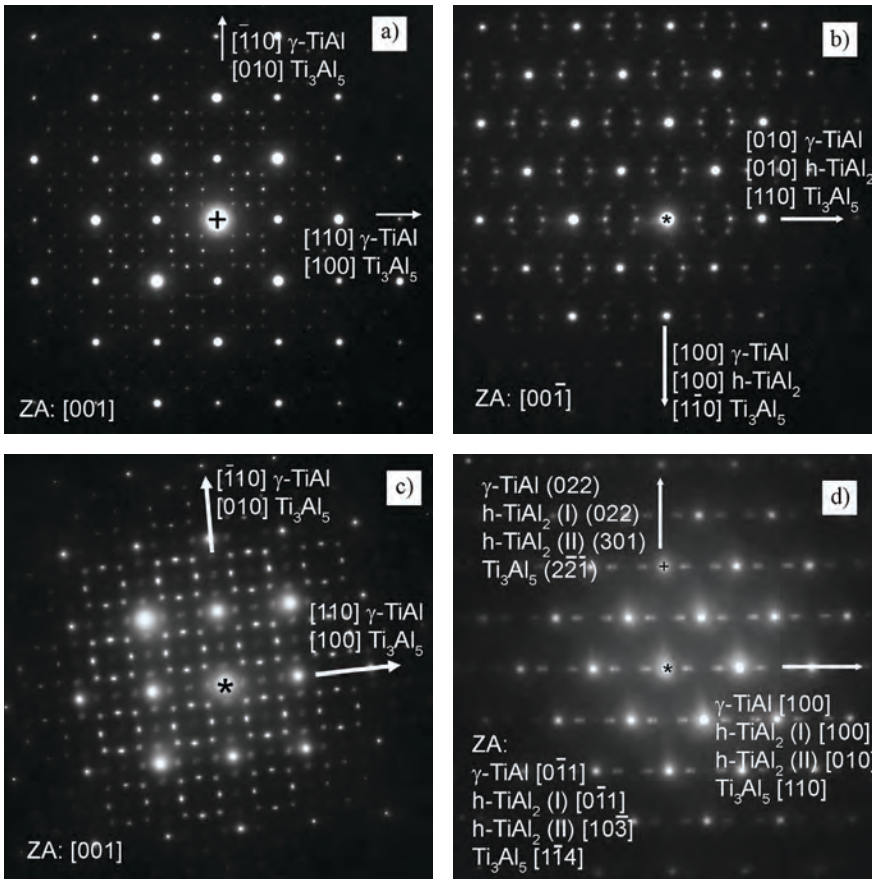
Fig. 3: *TEM selected area diffraction (SAED) patterns of differently processed alloys in the as-received condition a) Ti-59.7Al centrifugally cast; b) Ti-59.5Al, c) Ti-60.0Al, and d) Ti-60.5Al levitation melted [3].*

The transformation from metastable h-TiAl$_2$ to r-TiAl$_2$ can happen simultaneously by two different mechanisms, a continuous [8] and a discontinuous one [9], which are characterised by distinct orientation relationships of the resulting r-TiAl$_2$ + TiAl microstructure (Figs. 3-4). The investigation of the kinetics of both reactions reveals that at least at 900 °C the discontinuous reaction proceeds quicker than the continuous one [3].

Also the evolution of the microstructure is crucially affected by the initial microstructure in the as-processed alloys. For an alloy of the same composition and with the same heat treatment a fully lamellar r-TiAl$_2$ + TiAl microstructure can only develop if no h-TiAl$_2$ had been present at grain boundaries in the as-processed alloy because supersaturation with Al is apparently a prerequisite for the formation of a fully lamellar r-TiAl$_2$ + TiAl microstructure [3].

Fig. 4: *Illustration of a {310}$_{h-TiAl2\ (I)}$ //{310}$_{h-TiAl2\ (II)}$ rotational twin boundary between the two differently oriented types of h-TiAl$_2$. A projection of a slab with a thickness of six unit cells on the (001) plane is shown [3].*

References

1. Palm, M.; Stein F.: in Kim, Y.W.; Dimiduk, D.M.; Loretto, M.H.; (Eds). Gamma titanium aluminides 1999. Warrendale: TMS; 1999. p. 161.

2. Stein, F.; Zhang, L.C.; Palm, M.; Sauthoff, G.: in Hemker K.J. et al.; (Eds). Structural intermetallics 2001. Warrendale: TMS; 2001. p. 495.

3. Palm, M.; Engberding, N.; Stein, F.; Kelm, K.; Irsen, S.: Acta Mater. 60 (2012) 3559.

4. Schuster, J.C.; Palm, M.: J. Phase Equilib. Diffus. 27 (2006) 255.

5. Sturm, D.; Heilmaier, M.; Saage, H.; Paninski, M.; Schmitz, G.J.; Drevermann, A.; Palm, M.; Stein, F.; Engberding, N.; Kelm, K.; Irsen, S.: Mater. Sci. Eng. A 510-511 (2009) 373.

6. Stein, F.; Zhang, L.C.; Sauthoff, G.; Palm, M.: Acta Mater. 49 (2001) 2919.

7. Kelm, K.; Aguilar, J.; Drevermann, A.; Schmitz, G.J.; Palm, M.; Stein, F.; Engberding, N.; Irsen, S.: Mater. Res. Soc. Symp. Proc. 1128 (2009) 135.

8. Loiseau, A.; Vannuffel, C. : Phys. Status Solidi A 107 (1988) 655.

9. Zhang, L.C.; Palm, M.; Stein, F.; Sauthoff, G.: Intermetallics 9 (2001) 229.

S E L E C T E D   H I G H L I G H T S

Design of Ductile Mg Alloys Based on Combined *Ab Initio* and Experimental Methods

S. Sandlöbes [1], M. Friák [2], Z. Pei [2], L. Zhu [2], F. Wang [1], J. Chen [1], S. Zaefferer [1], J. Neugebauer [2], D. Raabe [1]

[1] Department of Microstructure Physics and Alloy Design
[2] Department of Computational Materials Design

Magnesium based alloys are attractive for many engineering structural applications owing to their low mass density and high specific strength. However, wide industrial application of Mg is limited by its poor room temperature formability, which is caused by pronounced basal slip and a strong basal texture. Hence, the von Mises criterion requiring five independent deformation modes is not fulfilled. In hcp crystals deformation along the crystal c-axis can only be accommodated by the activation of non-basal slip and deformation twinning. Single-phase solid-solution Mg−Y alloys show an increase in room-temperature ductility by about 5 times compared to conventional Mg alloys, while maintaining a comparable strength and well balanced work hardening. Using 3-D EBSD (Electron Backscatter Diffraction) orientation microscopy to calculate the density of geometrically necessary dislocations (Fig. 1) and transmission electron microscopy (TEM) [1] we show that this ductility increase is related to higher activities of <c+a> dislocation slip providing a <c>-deformation component in Mg−Y.

We show by joint TEM measurements and *ab initio* calculations that this enhanced activation of out-of-basal-plane shear modes through the addition of Y to Mg is correlated to a significantly decreased I_1 intrinsic stacking fault energy (SFE) [3]. Both approaches show that the I_1 SFE is decreasing with increasing Y concentration (Fig. 2). The reduction of the I_1 SFE can be used to explain the ductility increase in the Mg−Y system: The enhanced ductility is caused by a high activity of pyramidal <c+a> dislocations as slip modes out of the basal plane. The nucleation of <c+a> dislocations is the critical step in

(a)   <a> basal & prismatic screw

(b)   <c+a> pyramidal screw & edge

GND density log [m⁻²]
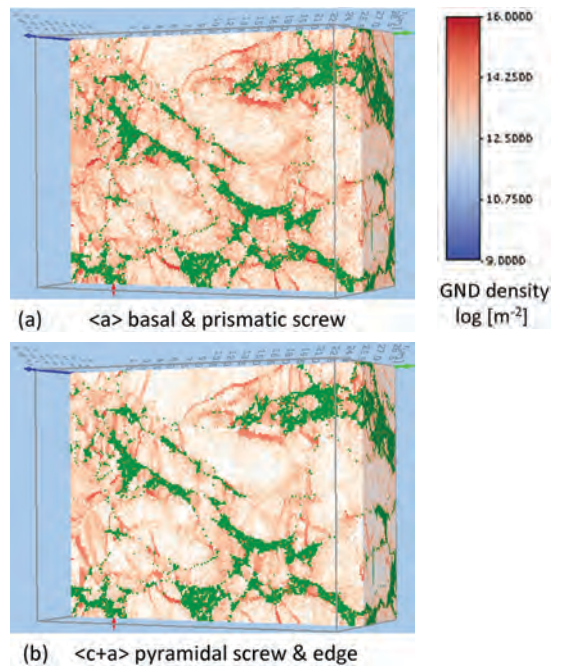
Fig. 1: *3D EBSD-based orientation microscopy on 30 % cold rolled Mg−3Y (wt.%) displaying the local density of geometrically necessary dislocations (GND) calculated using the Nye tensor approach. Green areas indicate deformation bands [2].*

providing out-of-basal-plane shear. This is associated with the stacking fault I_1 (SFI_1): the sessile SFI_1, whose energy decreases with Y alloying, is bound by pyramidal partial dislocation. This enables the formation of dislocation structures on pyramidal planes.
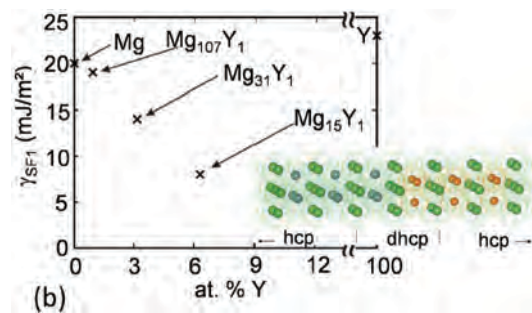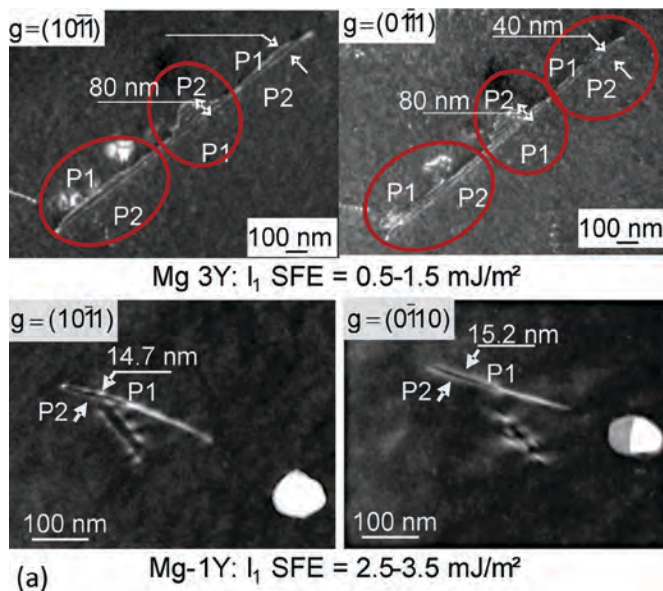
Fig. 2: *(a) TEM micrographs showing the SFI_1 in Mg−3Y and Mg−1Y (wt.%) for the different diffraction vectors g; P1 and P2 are the bounding partial dislocations, respectively. (b) Ab initio calculated SFI_1 energies of Mg−Y alloys [3].*
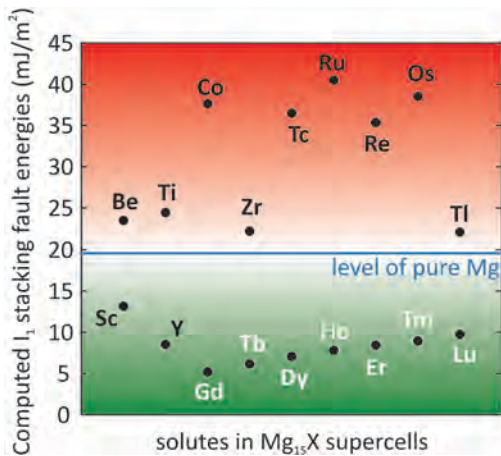
Fig. 3: *Theoretically predicted values of I_1 SFEs in Mg−X alloys for lanthanides (white) and non-lanthanides (black).*

According to the nucleation model of Yoo et al. [4] we suggest that the SFI_1 acts as heterogeneous nucleation source for pyramidal <c+a> dislocations. In summary, the addition of Y causes a reduction of the I_1 SFE which leads to the formation of stable SFI_1. They provide sources for <c+a> dislocations.

The identification of the I_1 SFE as guiding parameter for ductility provides a systematic approach to identify further favourable alloying elements. Following this approach we have performed *ab initio* calculations of the I_1 SFE of various Mg−X solid solution alloys (17 in total), Fig. 3. We focused on solutes with hcp structures in elemental state, i.e. matching the crystal phase of Mg [2]. To predict the SFI_1 energies, we combined a supercell computational approach with the Axial Next Nearest Neighbor Ising (ANNNI) model [5]. All seven hcp lanthanides reduce the I_1 SFE similar to Y (Fig. 3). In contrast, out of 10 non-lanthanide solutes, only Sc alloying reduces the I_1 SFE.

Based on these theoretical suggestions we produced five new binary single-phase Mg−X alloys adding elements which were calculated by DFT to decrease the I_1 SFE (X; Dy, Tm, Tb, Er, Ho). Tensile testing of the as-homogenized alloys reveals a significant enhancement of the room temperature ductility without a reduction of strength, Fig. 4, nicely verifying the theoretical predictions.

The optical photographs in Fig. 4 show pure Mg and Mg−3Tb (exemplary for all five new alloys) after cold rolling. The observed ductility of the newly designed alloys up to cold-rolling thickness reductions above 40 % reveals the ability of the alloys to accommodate strain along the crystal c-axis. Contrary, pure Mg starts fracturing during cold rolling already after a 10 % thickness reduction along macroscopic shear bands. The EBSD-KAM (Kernel Average Misorientation) maps in Fig. 4 display the local orientation gradients, i.e. strain distribution, in the deformation microstructures. They clearly reveal that the shear bands in pure Mg are resulting from strain localization which is due to an insufficient number of available deformation mechanisms. In contrast, the new Mg alloys exhibit homogeneous strain distribution during deformation. This finding proves the activity of non-basal deformation systems, i.e., non-basal dislocation slip in the new ductile Mg alloys.

In conclusion, we demonstrate that combining *ab initio* calculations with advanced experimental characterization methods facilitates the identification and understanding of critical microstructure parameters as basis for advanced materials design of complex structural engineering materials.

References

1. Sandlöbes, S.; Zaefferer, S.; Schestakow, I.; Yi, S.; Gonzales-Martinez, R.: Acta Mater. 59 (2011) 429.
2. Chen, J.; Zaefferer, S.; Konijnenberg, P.: Proc. 9th Int. Conf. Mg alloys and their applications (2012) 553.
3. Sandlöbes, S.; Friák, M.; Dick, A.; Zaefferer, S.; Yi, S.; Letzig, D.; Pei, Z.; Zhu, L.-F.; Neugebauer, J.; Raabe, D.: Acta Mater. 60 (2012) 3011.
4. Yoo, M.H.; Agnew, S.R.; Morris, J.R.; Ho, K.M.: Mater. Sci. Eng. A 310-321 (2001) 87.
5. Dick, A.; Hickel, T.; Neugebauer, J.: Steel Research Int. 80 (2009) 603.

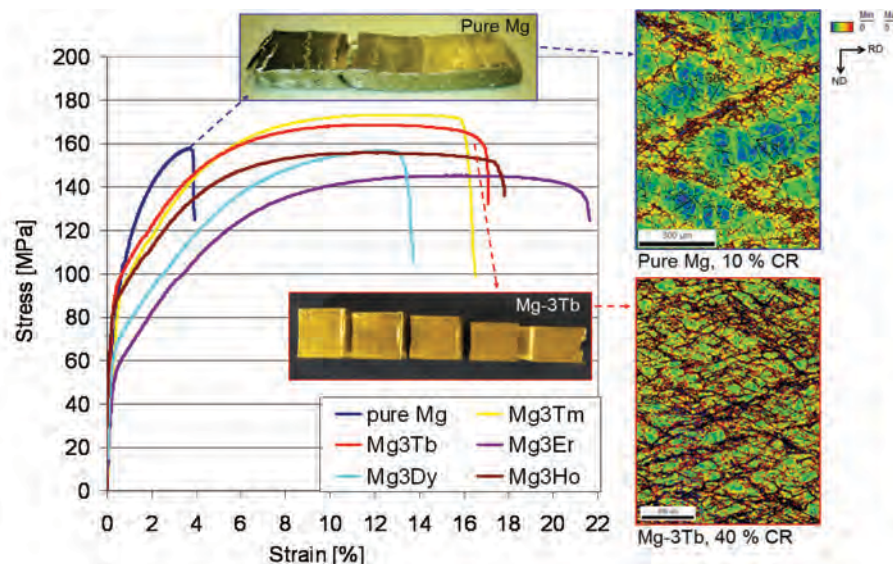**Fig. 4:** *Tensile stress-strain (engineering strain) curves of the newly designed Mg alloys in as-homogenized conditions in comparison to pure Mg. The optical photographs show the alloys after cold rolling (CR) to different thickness reductions. The EBSD-KAM (Kernel Average Misorientation) maps on the right side display the local orientation gradients, i.e. the strain distribution, from 0° to 5° misorientation.*

Theoretical-Experimental Investigation of Gum Metal Plasticity

*C. Tasan[1], E. Plancher[1], S. Sandlöbes[1], H. Springer[1], D. Raabe[1],
B. Grabowski[2], L. Huang[2], D. Ma[2], M. Friak[2], J. Neugebauer[2]*

[1] Department of Microstructure Physics and Alloy Design
[2] Department of Computational Materials Design

"Gum metal" is a Ti-Nb based alloy developed by a new design strategy that employs *ab initio* simulations to locate vanishing elastic constants resulting in excellent mechanical behavior [1]. The connection between the vanishing elastic constants and the superior mechanical properties is not yet fully understood: while a novel "dislocation-free" and "ideal-bulk-shear" plasticity mechanism had originally been proposed [1], subsequent studies refuted this provocative assumption [2]. The conflict is due to limitations of the employed theoretical and experimental methods. Theoretically, the main shortcoming is the discrepancy with experimental reality: whereas experiments primarily focus on complex compositions (e.g., Ti−Nb−Ta−Zr−O), theoretical approaches are restricted to the simple binary Ti-Nb system [3], with further simplifications due to finite temperature approximations. Experimentally, the variety and complex interplay of the reported mechanisms [2] require to go beyond the typically used post mortem analysis by employing *in situ* investigations.

The new Adaptive Structural Materials (ASM) group (see p. 13) combines on an equal footing state-of-the-art finite temperature *ab initio* expertise and multiscale *in situ* experiments being well suited for these challenges. Our approach to the gum metal problem involves a systematic purification of experimental conditions while improving the theoretical models to overcome the discrepancy between experimental complexity and theoretical simplification. Following this strategy, gum metal compositions with and without oxygen are produced and mechanically tested to verify the critical role of oxygen. To identify the nature of the ideal bulk shear mechanism, samples are *in situ* tested in an as-solution treated condition, since this provides a well-defined microstructure compared to the complex heavily cold-worked marble like structures typically analysed. Following key observations can be drawn from our data: (i) in the absence of oxygen, the specific gum metal properties are lost. (ii) The dominant deformation mechanism is ω transformation-assisted nano-twinning rather than the proposed ideal bulk shear (Fig. 1a-d). Note that the latter conclusion crucially relies on the high-end multi-scale *in situ* experimental techniques available to the ASM group (see also caption of Fig. 1). In future steps, to further
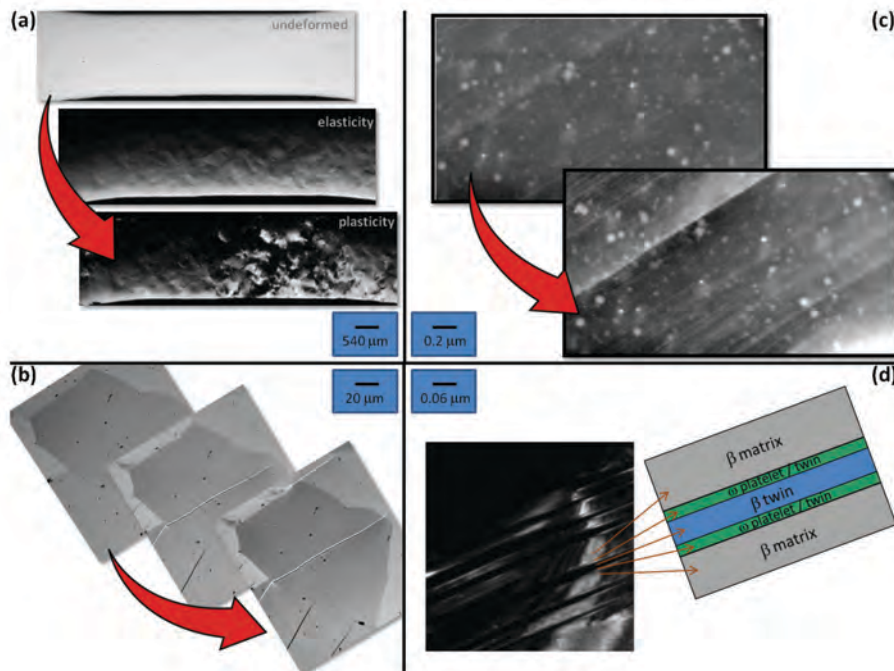
Fig. 1: *(a) In situ stereomicroscope testing reveals a significant density of deformation steps on the pre-polished surface. (b) In situ SEM experiments with SE imaging show that these steps, similar to those reported in gum metals earlier [1], have different morphologies than dislocation slip traces or macroscopic twins observed in β-titanium alloys. (c) In situ SEM experiments with BSE imaging reveal that each of the faults has a lamellar morphology consisting of many nano-layers, (d) which are identified in TEM as an internal lamellar-like structure composed of {112}<111> β nano-twins and deformation induced ω phase.*
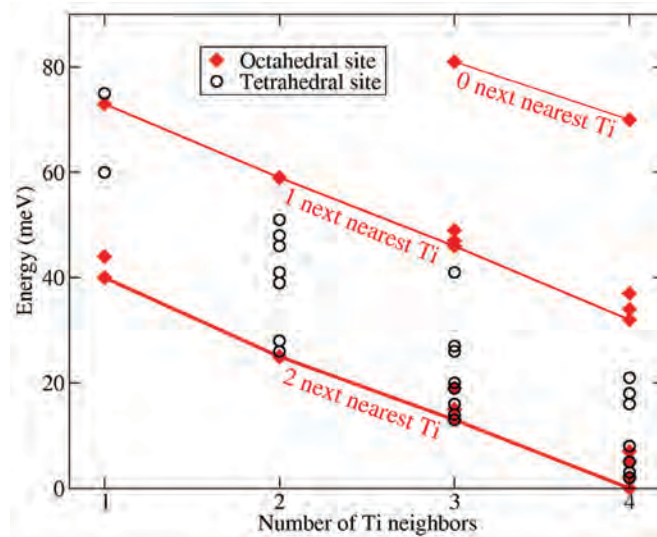
Fig. 2: *Ab initio results of the energetics of an oxygen interstitial in Ti-Nb. Energies for a tetrahedral and an octahedral site are shown as a function of the number of Ti neighbors and relative to the most favorable site. For the tetrahedral site, the x-axis refers to the first shell of atoms around the interstitial. For the octahedral site, where the first two shells are needed for an adequate description, the x-axis refers to the second shell while the number of Ti atoms in the first shell is indicated in the figure. The lines are a guide to the eye emphasizing the preference of the O atom to be in a Ti-rich environment.*

increase the connection to theory, simpler Ti−Nb + O ternary alloys of systematically varying composition and thermo-mechanical treatment will be analysed with our *in situ* methods.

Following our experimental findings and additional literature observations [4] regarding the importance of oxygen, the first theoretical steps are directed towards *ab initio* investigations of the energetics of oxygen in Ti−Nb. Fig. 2 shows results for interstitial oxygen in Ti−23 at.%Nb, specifically, for the octahedral and tetrahedral sites as function of the local environment. The relevance of this figure is given by the fact that Ti−Nb is expected to be disordered at finite temperatures and hence the oxygen atom will have different local environments available which can be occupied according to their energies. The simulations reveal three main conclusions: (i) most tetrahedral sites are unstable with respect to the octahedral site. (ii) The O atom prefers a Ti rich environment and (iii) the overall energy scale of the various sites is rather small, suggesting that various sites will be available to the oxygen atom at higher temperatures. Following the strategy noted above, next theoretical steps aim at increasing the theoretical complexity by considering the role of the metastable ω phase and the influence of oxygen on ω stability. A crucial ingredient in this respect is the specific expertise of the ASM group in carrying out accurate *ab initio* simulations at finite temperatures.

In the long term, once the mechanisms and atomistic variables of the gum effect are understood, we plan to use our finite temperature *ab initio* methodology to create maps of instabilities as function of temperature, strain, and composition (Fig. 3), in order to guide the experimental design of new-generation gum alloys with further improved properties.
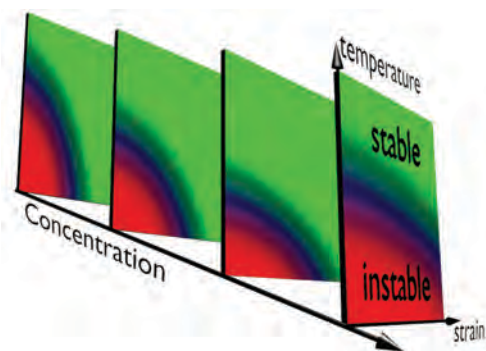
Fig. 3: *Schematics of our long-term goal: a 4D representation of an instability map (in terms of elastic constants) as function of different variables (e.g., temperature, strain, and concentration).*

References

1. Saito, T.; Furuta, T.; Hwang, J.H.; Kuramoto, S.; Nishino, K.; Suzuki, N.; Chen, R.; Yamada, A.; Ito, K.; Seno, Y.; Nonaka, T.; Ikehata, H.; Nagasako, N.; Iwamoto, C.; Ikuhara, Y.; Sakuma, T.: Science 300 (2003) 464.

2. Talling, R.J.; Dashwood R.J.; Jackson M.; Dye D.: Acta Mater. 57 (2009) 1188.

3. Nagasako N.; Asahi R.; Hafner J.: Phys. Rev. B 85 (2012) 24122.

4. Tane, M.; Nakano, T.; Kuramoto, S.; Hara, M.; Niinomi, M.; Takesue, N.; Yano, T.; Nakajima, H.: Acta Mater. 59 (2011) 6975.

Investigations of the Thermal Stability of the Interface Formed during Explosive Cladding of Hastelloy B3 to Stainless Steel

A. Kostka [1], A. Szczepaniak [2], D. Raabe [2]

[1] Max Planck Fellow Research Group on High Temperature Materials
[2] Department of Microstructure Physics and Alloy Design

Metallurgical processes governing microstructure formation in the interface regions of heterogeneous joints are very complex and their understanding requires precise characterization under well defined welding conditions [1]. In this context joints of alloys from the Ni−Mo Hastelloy B family to steel are of high interest from an engineering standpoint owing to their huge relevance in the engineering design of advanced solutions where the combination of high thermal stability and exceptional corrosion resistance is demanded. Alloys from the Hastelloy B family (Ni-base alloy with Mo content up to 32 wt.%) are successfully used for many years, however, they suffer a serious drawback when welding is applied. One of the most important problems is an intergranular brittle fracture mode, where the cracks appear on the surface of the Hastelloy B2 after applied post-welding heat treatment [2]. Thus, a detailed microstructure-oriented understanding and property optimization of the underlying interfaces of the joints between dissimilar bulk metals are essential for the design of modern metallic compounds.

The aim of this investigation is to characterize and better understand the graded microstructures at the bonding zone and their metallurgical formation processes with regard to the mechanical behavior of the cladded joints between Hastelloy B3 (improved thermal stability with respect to the B2 family by optimization residual alloying elements) and austenitic stainless steel [3].

Explosive joining processing leads to (i) intense and localized plastic deformation, (ii) high localized stresses and (iii) high local temperature increase causing both melting and rapid solidification [4]. Fig. 1a shows the microstructure of the interface
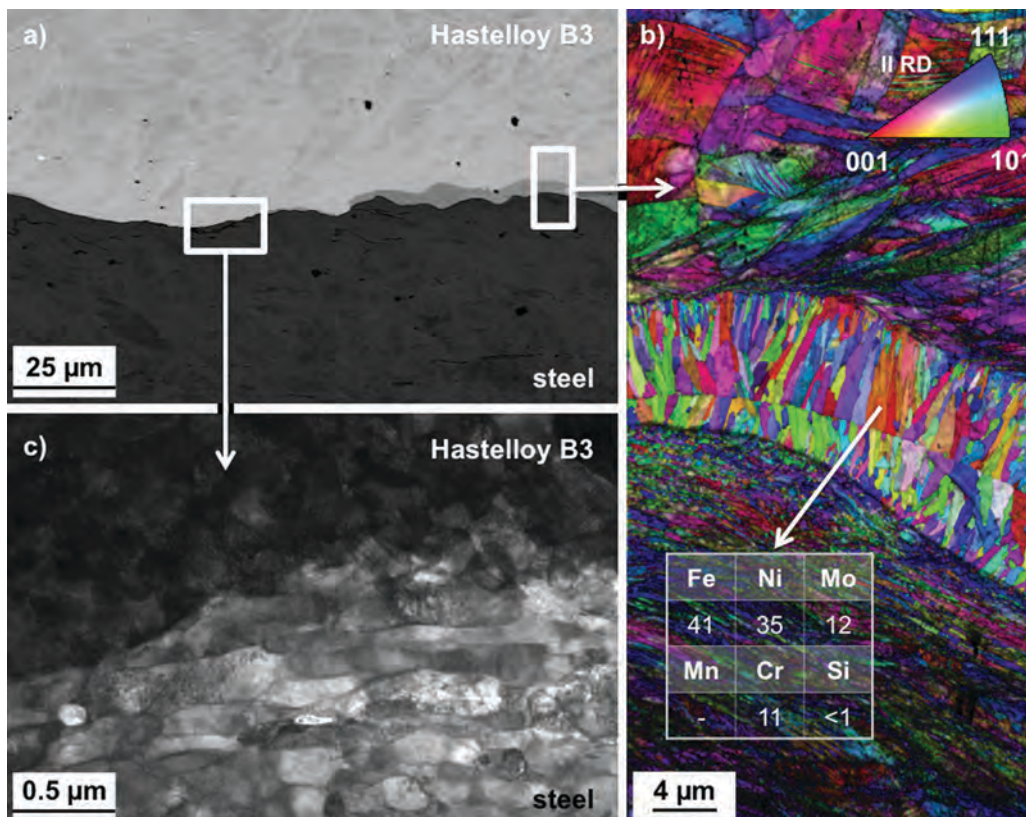
Fig. 1: *Analysis of the interface region of the clad: a) SEM (SE) micrograph showing the bond zone and melt pockets; b) inverse pole figure map revealing the microstructure development around the solidified material and its chemical composition (wt.%); c) TEM (BF) micrograph showing direct bonding between joined components (absence of a reaction layer).*
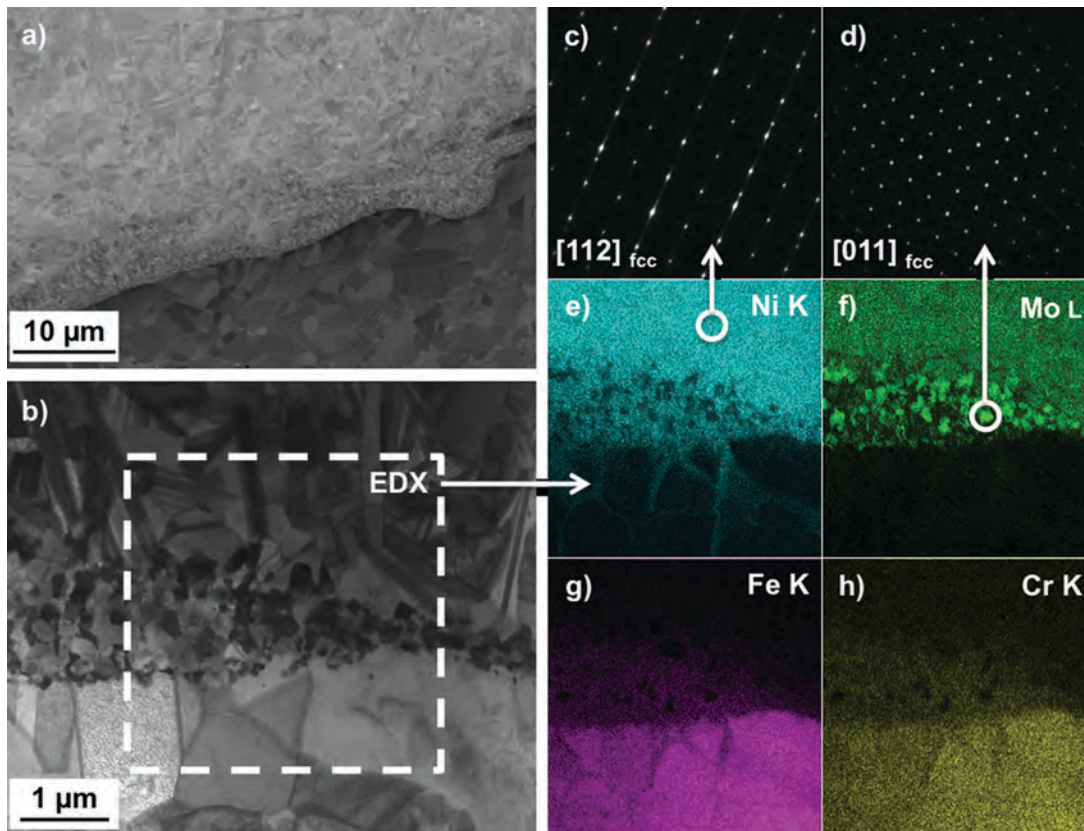
Fig. 2: *Evolution of the interface region of the clad after subsequent heat treatment (750°C, 1h, air cooling): a) SEM (SE) micrograph reveals recovery of both parent materials; b) STEM (BF) micrograph reveals presence of twins in the B3 Hastelloy; c) selected area electron diffraction from the B3 Hastelloy and d) precipitated Mo-rich (82 wt.%) phase; e-h) EDX element maps from the highlighted region in b).*

region after cladding. The interface does not reveal a regular wavy morphology (which is otherwise typical of explosive cladding process) but is partially flat. Localized melted regions (Fig. 1b) adjacent to the interface are identified in terms of their characteristic solidification-elongated grain shapes and a strong chemical inhomogeneity resulting from the intense chemical mixing of the joined components. Less than 25% of the interface length consists of melted and solidified regions (measured on the surface parallel to the welding direction at a distance of 1000 μm), thus the dominant type of the interface consists of strongly deformed parent material. TEM examination of this type of interface (Fig. 1c) reveals direct bonding and absence of any reaction products.

The effect of an applied heat treatment (750°C, 1h, air cooling) is presented in Fig. 2. Both parent materials recovered and small Mo-rich precipitates [4] appear at the interface. Acquired EDX maps indicate strong diffusion of Cr from the austenitic steel towards the region of Mo precipitations and Ni from the Hastelloy towards the steel up to 1 μm deep.

The amount of strain accumulated during collision of the joined plates leads to massive coldworking and strain hardening. The applied heat treatment significantly enhances diffusion processes as well as recovery and recrystallization and associated chemical reactions leading to the formation of complex new non-equilibrium phases.

In the following part of the project the correlations between the resulting microstructures and mechanical properties will be investigated in order to identify which of the microstructural constituents formed at the interface region are essential for damage initiation in these complex material compounds.

References

1. Song, J.; Kostka, A.; Veehmayer M.; Raabe D.: Mater. Sci. Eng. A 528 (2011) 2641.

2. Brooks, C.; Wang Y.: Metallography 23 (1989) 57.

3. According to EN 10088-2.

4. DuPont, J; Lippold J.; Kiser S.: in: Welding Metallurgy and Weldability of Nickel-Base Alloys, A John Wiley & Sons, INC., Publication Hoboken, New Jersey 2009.

Application of 3-Dimensional EBSD-Based Orientation Microscopy

S. Zaefferer, P.J. Konijnenberg, D. Raabe

Department of Microstructure Physics and Alloy Design

3D orientation microscopy based on a combination of electron backscatter diffraction (EBSD) and serial sectioning with a focused ion beam (FIB) offers a number of unique features for microstructure characterization, in particular the full, 5-parameter grain boundary description but also, for example, the description of the 3D morphology of crystals, or the determination of geometrically necessary dislocation (GND) densities. 3D EBSD data sets can be analysed in two approaches, either as volume pixels (voxels) or by reconstructing interfaces and boundaries.

Voxel-based description of 3D data

After measurement, 3D EBSD data exist first as unconnected voxels. When describing crystalline microstructures it is important to group these voxels into crystallites or subgrains. To this end the measured sections first have to be aligned such that subsequent sections fit together in an optimum manner. Alignment procedures for shifts of complete sections as well as unsystematic misalignments due to drift during the EBSD measurements have been developed.

After slice alignment a segmentation algorithm is used to group voxels into grains. An example for a rendered voxel-based microstructure is displayed in form of an EBSD pattern quality (PQ) map in Fig. 1a for a tensile-deformed low-alloyed TRIP steel. The volume outlined by dashed lines is rendered as an inverse pole figure (IPF) voxel map in Fig.1b for one deformed ferrite grain. A particularly interesting analysis with respect to deformation and phase transformation is the calculation of GND densities according to Nye [1] and Kröner [2]. Fig. 1c displays the total GND density calculated for a fraction of the volume marked in Fig. 1a, in comparison to a 3D KAM (kernel average misorientation) map of the same volume, displayed in Fig. 1d. While the KAM map represents the orientation gradient at every position, the GND map represents, in principle, the curvature of the orientation field.

5 parameter grain boundary characterization

3D orientation microscopy can be used to describe the crystallographic nature of interfaces. If one disregards the atomistic level, grain boundaries are comprehensively described by 5 parameters, that is the misorientation across the boundary (3 parameters) and the crystallographic orientation of one of the interface normals (2 parameters) (see, e.g., Rohrer [3]).
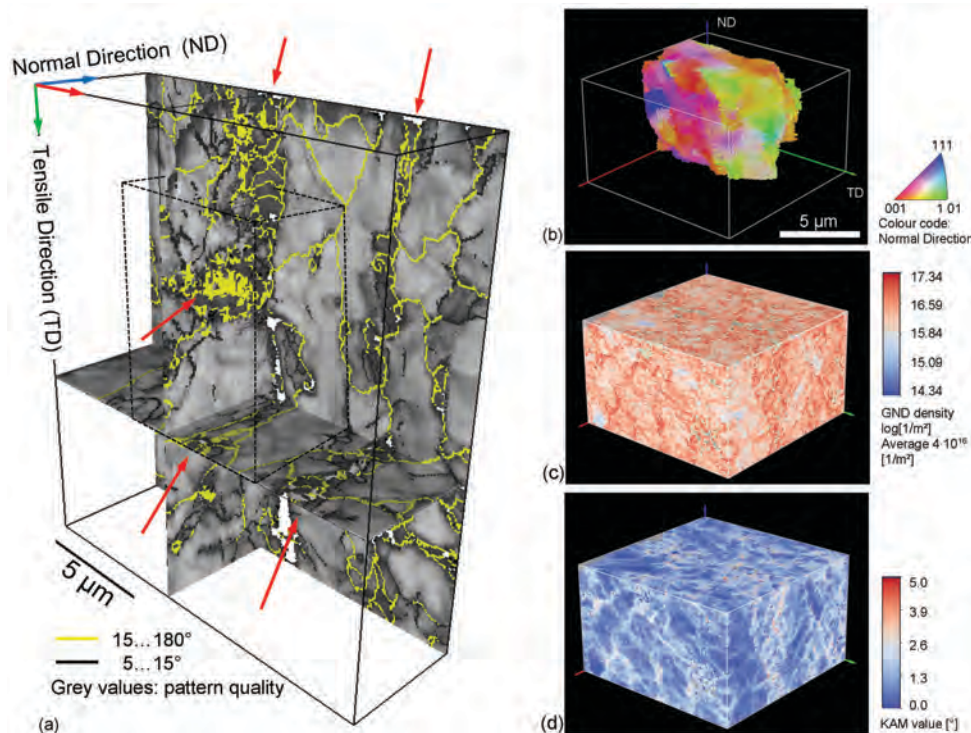
Fig. 1: *(a) 3D EBSD pattern quality mapping obtained from a low alloyed TRIP steel deformed in a tensile test almost to fracture (measurement: 60 slices à 100 nm distance). The position of martensite bands is indicated by red arrows. Yellow and black lines indicate large-angle (>15°) and medium-angle (5…15°) grain boundaries. (b)-(d)Voxel-based display of the area marked by dashed lines in fig. (a). (b) Inverse pole figure (IPF) plot of the sheet normal direction (ND) of one grain in the structure. (c) 3D plot of the density of geometrically necessary dislocations (GND) (in log 1/m²)). (d) 3D plot of the kernel average misorientation (in degree) calculated for direct neighbours.*
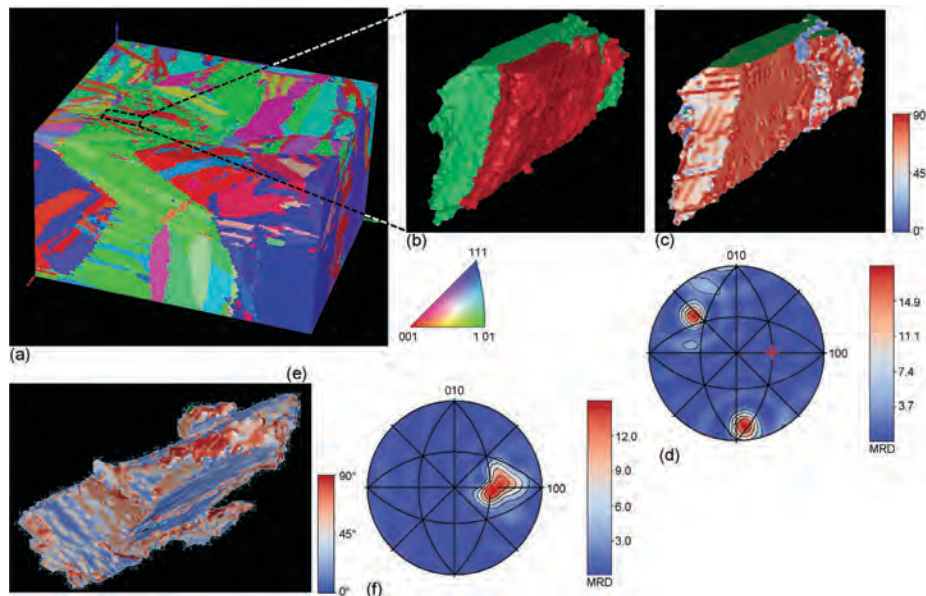
Fig. 2: *3D display of the microstructure of an Fe-28% Ni alloy (material supplied by N. Tsuji, Kyoto University). (a) The full block of material displayed as IPF map of the sample normal direction. (b) Two neighbouring plates of lenticular martensite taken from (a). (c) Twist-tilt character plot of the interface between the grains in (b). (d) Grain boundary normal pole figure of the interface from fig. (c) indicating the position of the misorientation rotation axis as red cross. Both grain boundaries have tilt character. (e) Twist-tilt plot of the interface between two other grains. (f) Grain boundary normal pole figure of the grains in (e) indicating a pure twist boundary.*

Boundary reconstruction is composed of two sequential steps; identifying the boundary surface and subsequently translating this surface into a mesh of triangles. A well-known method for boundary reconstruction is the Marching Cubes (MC) algorithm [4] which has been applied for boundary reconstruction from orientation voxels before [5]. The ambiguities inherent to the MC algorithm can be solved by disassembling each cube into unambiguous tetrahedra, resulting in the so-called Marching Tetrahedra (MT) algorithm [6] which has been implemented in our software.

The as-meshed surface structure still requires smoothing because of its inherent roughness and artefacts due to a poor slice alignment. We developed a smoothing strategy [7] which is inspired by computer models for grain growth simulation as implemented in a vertex model by Barrales [8].

In our model, in contrast to classical vertex models, the number of grains must stay constant (thus no topological changes) and quadruple junctions are not allowed to move. All boundaries and triple lines are treated each with a uniform mobility and surface energy. We refer to this approach as a Constrained Vertex Model (CVM) method.

The described algorithms have been employed for the analysis of some selected grain boundaries in a fully martensitic Fe 28% Ni alloy, Fig. 2a. After the grain structure was established the boundary structure was meshed with the MT method and smoothed using the CVM method. In order to describe the grain boundary character three grains were isolated from the microstructure, Figs. 2b and e. The mean disorientation between the grains amounts to about 55°[101] between the grains in Fig. 2b and

53°[323] between the grain in (e) and its (not shown) neighbour. Both grain misorientations correspond to typical disorientations between two Nishiyama-Wassermann variants. The grain boundaries are shown in Figs. 2c and 2e, where the colour code indicates the boundary character in terms of the angle between the disorientation rotation axis and the grain boundary normal. The boundary character is twist if both vectors are parallel and tilt if both vectors are perpendicular. This situation is shown more quantitatively in the pole figures of the boundary normal vectors in Figs. 2d and 2f. The misorientation axis is marked by a cross. Note, that the distinction between twist and tilt boundaries enables an essential geometrical classification of small angle interfaces. Its physical relevance for boundaries with large angle misorientations is, however, limited.

References

1. Nye, J.F.: Acta Metall. 1 (1953) 153.

2. Kröner, E.: Continuum Theory of Defects. Physics of Defects, North-Holland, Amsterdam (1981).

3. Rohrer, G.S.: J. Am. Ceram. Soc. 94 (2011) 633.

4. Lorensen, W.E.; Cline, H.E.: Computer Graphics 21 (4) (1987) 163.

5. Dillon, S.J.; Lee, S.; Rollett, A.D.; Rohrer, G.S.: Microsc. Microanal. 14 Suppl. S2 (2008) 978.

6. Dillard, S.; Bingert, J.; Thoma, D.; Hamann, B.: IEEE TVCG 13 (6) (2007) 1528.

7. Konijnenberg, P.J.; Zaefferer, S.; Lee, S-B.; Rollett, A.D.; Rohrer, G.S.; Raabe, D.: Mater. Sci. Forum 702-703 (2011) 475.

8. Barrales-Mora, L.A.: "2D and 3D Grain growth Modeling and Simulation", Ph.D. thesis, Cuvillier Verlag Göttingen (2008).

Microstructure Effects on Hydrogen Embrittlement in Austenitic Steels: A Multidisciplinary Investigation

S. Evers[1], T. Hickel[2], M. Koyama[3], R. Nazarov[2], M. Rohwerder[1], J. Neugebauer[2], D. Raabe[3], M. Stratmann[1]

[1] Department of Interface Chemistry and Surface Science, [2] Department of Computational Materials Design
[3] Department of Microstructure Physics and Alloy Design

Hydrogen atoms, which can be absorbed into steel during production and service, often have a detrimental embrittling effect on the mechanical properties of iron and steels. It is meanwhile known that hydrogen embrittlement (HE) is also affected by the microstructure of the material. Consequently, previous indications that hydrogen atoms are trapped by vacancies, dislocations, and grain boundaries led at MPIE to investigations of superabundant vacancy formation, hydrogen-enhanced local plasticity (HELP), and hydrogen-enhanced decohesion (HEDE). Despite these efforts, any proof of a HE mechanism to be active in a given steel sample has so far been a formidable task, which cannot be achieved by a single method. A direct experimental observation of hydrogen impurities is difficult due to the low solubility and high mobility of hydrogen in steels, whereas pure theoretical investigations are challenged by the complexity and diversity of microstructural features present in steels.

We therefore follow a multidisciplinary strategy to derive a deeper understanding of HE in steels. This strategy combines novel potentiometric methods based on the Kelvin probe technique to detect the local hydrogen content in materials (GO department), *ab initio* determination of the same quantities including the local behaviour at grain boundaries (CM department), and characterization of hydrogen induced materials failure (MA department) using orientation-optimized electron channelling contrast imaging (ECCI). Selected findings of these investigations and their relevance for austenitic steels are summarized in the following:

The crucial idea for the new **hydrogen detection method** is the observation that hydrogen dissolved in a palladium matrix leads to the formation of a hydrogen electrode on the palladium surface, even in dry atmospheres. The origin is the presence of a nanoscopic water layer adsorbed on the surface, enabling the formation of a corresponding electrochemical double layer [1, 2]. As the electrode potential for the hydrogen electrode depends logarithmically on the activity of H in Pd, this potentiometric method is extremely sensitive especially at low activities.

The idea can be employed for the investigation of steels (and various other materials) by evaporating a thin film of Pd on their surface. Since the chemical potential of H in iron-based materials is much higher than in Pd, H diffuses into the Pd film. Time dependent measurements of this accumulation can be used to perform extremely sensitive and laterally resolved measurements of H permeation through and its presence in materials. In the latter case an effective "activity" of H is measured, providing information about depth and density of traps sites. Main challenges of this method are the need for an exact calibration of the potential-concentration correlation for H in the evaporated Pd films, the precise calibration of the Kelvin probe tip in the dry nitrogen measurement atmosphere, as well as its long term stability.

As an example the measurement of H in a H-charged austenitic steel sample, comprised of mainly austenitic and ferritic grains, is shown in Fig. 1. It can be seen that the austenite contains much more H, as the potential decreases much faster over the austenite grains. Especially active sites are located at boundaries between ferrite and austenite.

An additional insight into the relevance of the different phases and their boundaries has been
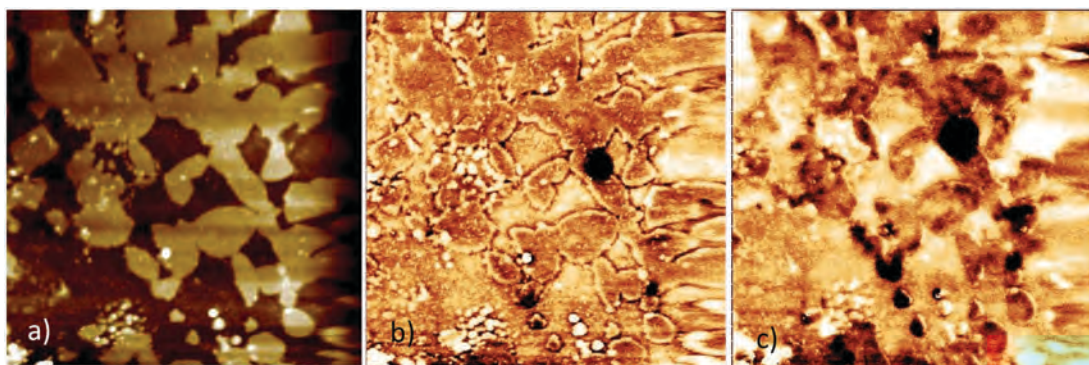
Fig.1: *Detecting hydrogen on a 50×50 µm² surface area of a H charged austenitic steel after evaporation of a 100 nm Pd film. a) A topographic image obtained by AFM indicates austenitic (due to surface preparation topographically higher) and ferritic (lower, i.e., darker) regions. b) and c) Potential maps of this area obtained after 28 h and 44 h in the Kelvin probe mode. Above the austenites the potential decreases faster than above the ferrites due to the larger amount of stored hydrogen. The dark spots in b)-c) indicate sites with especially high hydrogen concentrations (traps).*
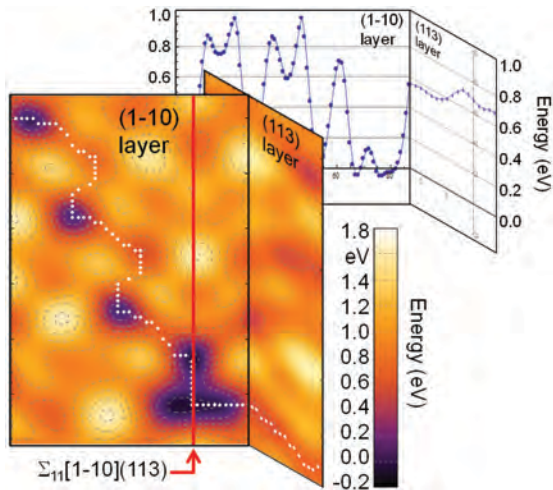
Fig. 2: *Potential energy surface for a single H interstitial next to a Σ_{11}[1-10](113) grain boundary in fcc iron. The minimum energy path for a diffusion in a (1-10)/(113) plane perpendicular/parallel to the boundary is indicated by white dots. In the upper part the corresponding energies along the same path are plotted.*

Fig. 3: *ECCI micrograph for the crack propagation in Fe–18Mn–1.2C austenitic steel. The cracks initiate at a grain boundary, where deformation twins are intercepting. The crack propagation afterwards continues along the deformation twins.*

obtained by **ab initio calculations** based on density functional theory (DFT). They clearly confirm the increased solubility of H in austenite grains as compared to the ferrite grains. Mn yields further increase of the austenite solubility by straining the lattice (volume effect). One of the new insights obtained by the calculations is that small amounts of further alloying elements (like Ca, Nb, Si, Ti, and in particular Mo) considerably enhance the preference of H for austenite [3].

In order to understand the experimental results on microstructures, we have additionally used DFT to study the solubility and diffusion of hydrogen in austenite twin and grain boundaries [4]. We generally find that the solution energy of H strongly depends on the local coordination and that it is in this case only moderately correlated with the actual volume of the interstitial site. Within open structures, such as the Σ_{11}[1-10](113) fcc grain boundary, various different interstitial sites are favorable for the incorporation of H atoms, providing effective trapping centres (Fig. 2). Only if these traps are filled by other H atoms, efficient diffusion channels along (113) planes might become active. We further find that the critical strain required to fracture the material is reduced by the presence of hydrogen in this grain boundary. For twin boundaries, the DFT calculations show that interstitial H atoms are actually slightly repelled. As origin for this unusual and unexpected behaviour the structural similarity between the octahedral interstial configurations in the twins and in austenitic bulk has been identified.

These theoretical insights are highly relevant for experiments, which *investigate the fracture mode* in austenitic steels. For this purpose the recently developed orientation-optimized ECCI method has proven to be particularly useful to reveal deformation twins and complex dislocation substructures in TWIP steel. The actual measurements have been performed for a H charged Fe–18Mn–1.2C austenitic steel [5], for which the tensile ductility was drastically reduced by H charging during tensile testing. The central region of these samples, which have not been reached by hydrogen, showed a ductile fracture surface. In contrast, a brittle fracture surface was observed from the surface down to about 150 μm. The facet size of the brittle fracture areas is about 50 μm, which corresponds to the grain size, indicating that intergranular fracture was caused by H charging.
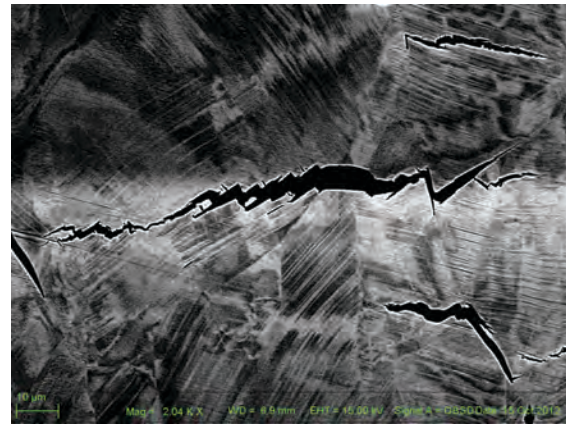
An advantage of the employed ECCI method is that in addition to the cracks primary and secondary deformation twins on (11-1) and on (1-11) planes become visible with bright contrast (Fig. 3). The measurements therefore revealed that cracks typically occur at grain boundaries with intercepting primary deformation twins. The stress concentration at these points and the reduction of the cohesive energy by hydrogen loading apparently yields crack initiation. While the primary fracture mode is intergranular, one additionally observes crack propagation following primary and secondary deformation twin boundaries (Fig. 3). Since the *ab initio* calculations predict that perfect twin boundaries are not sensitive to H, the stresses due to the interception of twins with grain boundaries or of primary with secondary twins need to be responsible for such a transgranular fracture along twin boundaries. Being crucially important, because deformation twinning is essentially required to achieve the superior mechanical properties of TWIP steels, further investigations of this effect are currently performed.

References

1. Senöz, C.; Evers, S.; Stratmann, M.; Rohwerder, M.: Electrochem. Comm. 13 (2011) 1542.

2. Evers, S.; Rohwerder, M.: Electrochem. Comm. 24 (2012) 85.

3. Nazarov, R.; Hickel, T.; Neugebauer, J.: *in preparation.*

4. Du, Y.A.; Ismer; L., Rogal, J.; Hickel, T.; Neugebauer,J.; Drautz, R.: Phys. Rev. B 84 (2011) 144121.

5. Koyama,M.; Akiyama, E.; Sawaguchi, T.; Raabe, D.; Tsuzaki, K.: Scr. Mater. 66 (2011) 459.

Absence of an Intrinsic Mobility for Grain Boundary Migration

C.P. Race, J. von Pezold, J. Neugebauer

Department of Computational Materials Design

The migration of grain boundaries in polycrystalline materials plays a crucial role in the evolution of microstructure in processing and application. A clear picture of how grain boundaries move is necessary for a full understanding of the mechanical properties of materials and will help enable the design of new materials to meet current technological challenges.

Direct simulation of the evolution of the grain boundaries in a polycrystal under realistic conditions lies beyond the timescales achievable with atomistic simulation techniques such as classical molecular dynamics (MD). MD is thus frequently used rather as a tool to explore fundamental properties of isolated grain boundaries in bicrystals. These properties can then form inputs to larger length and time scale models.

This reductive approach gives rise to the concept of an "intrinsic mobility" of a grain boundary of a given geometry: a constant of proportionality between the velocity with which the boundary moves and the thermodynamic driving force for its motion. MD simulations (and experiments) in bicrystals might then be used to map out these intrinsic mobilities as functions of grain boundary structure.

The study of grain boundary migration with MD is still in its infancy and many mysteries remain to be solved. In particular, little is known in detail about grain boundary migration mechanisms. We have therefore undertaken extensive investigations of a model boundary – the [111] $\Sigma 7$ symmetric tilt boundary – in order to understand its migration mechanism and how this affects the measured mobility.

We have focused in particular on the smooth (i.e. at temperatures below the roughening transition) flat (i.e. curvature-free) boundaries frequently used as a basis for measuring intrinsic mobility in simulations and experiment. By extending our analysis to larger system sizes and smaller driving forces than those typically used, we find that key assumptions about the migration kinetics do not hold. The boundary velocity v is not proportional to the driving force (Fig. 1a) and instead shows a finite threshold force for migration and an upward curvature. An Arrhenius plot of $\ln(v)$ against inverse temperature ($1/T$) (Fig. 1b) reveals that there is no single activation energy barrier for grain boundary migration: the barrier depends both on the driving force and on the temperature. We find that the grain boundary velocity depends strongly on the system size (Fig. 1c).

As the origin of this unexpected behaviour, we have identified that at the mesoscale the migration mechanism involves the formation and growth of islands of crystal volume transformed from the thermodynamically disfavoured to the favoured orientation (Fig 2a). Thus the migration of smooth flat boundaries involves a homogeneous nucleation process: for migration to take place an island of migrated material must form of sufficient radius r that the free energy cost of creating the edge of the island is compensated by the free energy gain of the island volume in the more stable orientation. The need to stabilise a critical nucleus naturally explains the threshold driving force for motion evident in Fig. 1a. As the driving force for migration is increased,
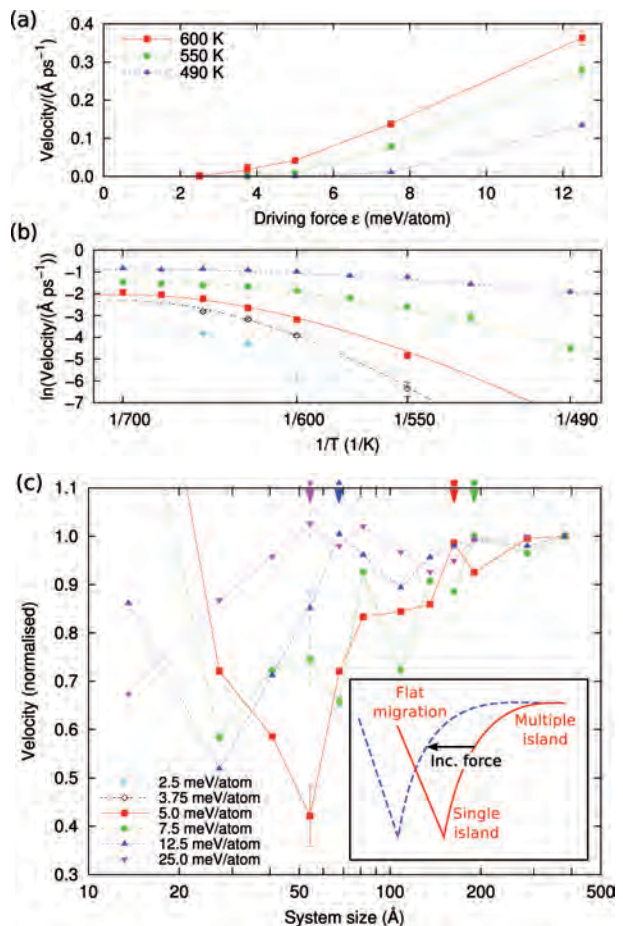
Fig. 1: *Results of MD simulations of our grain boundary. (a) The velocity as a function of driving force at several temperatures.(b) An Arrhenius plot of the velocity as a function of temperature for several driving forces (symbols are as for the key in figure (c)). The lines are predictions of the island free energy model. (c) The normalised velocity at 600 K as a function of system size (cell dimension in grain boundary plane) and driving force.*
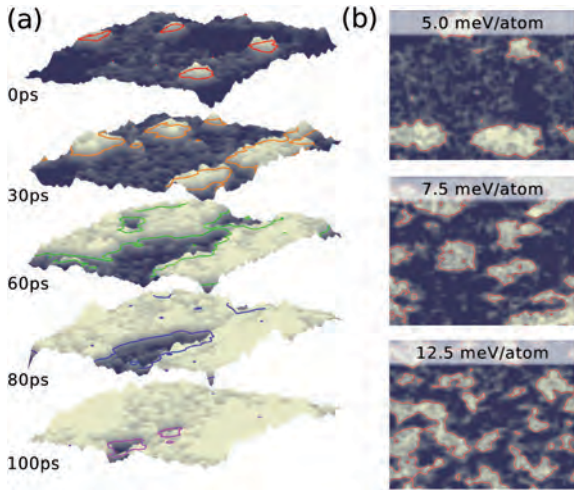
Fig. 2: *Snapshots of a migrating grain boundary surface for a large system (340 Å by 420 Å) with a driving force of 5.0 meV/atom at 600 K. (b) Snapshots of islands as a function of driving force.*

the size and energy of critically stable nuclei will decrease (Fig. 2b), explaining the upward curvature in the velocity with force.

We can model the excess free energy of an island nucleus of radius r as

$$\Delta F(r,T,P_D) = 2\pi r(\gamma - T\sigma) - \pi r^2 dP_D$$

where T is the temperature, P_D the driving pressure, d the height of the island, γ the energy per unit length of the island edge and σ the corresponding entropy density. We can obtain $\gamma = 31.5$ meVÅ^{-1} from molecular statics calculations of relaxed islands (Fig. 3a). The edge entropy is modelled as $\sigma = \gamma/T_C$, where $T_C = 700$ K is the boundary roughening temperature. This model, free of fitted parameters,

accurately predicts the shape of the Arrhenius curves of $\ln(v)$ against $1/T$ at varying driving force (Fig. 1b).

For migration by island nucleation and growth, the excess free energy of a critical island nucleus can be identified with the activation energy for boundary motion. This barrier will be $\Delta F^* = \pi\gamma^2(1 - T/T_C)^2/P_D d$. Crucially, we see that the activation energy has an inverse dependence on the driving force for motion. We have verified this inverse dependence with MD simulations at low driving forces (Fig. 3b).

Our simulation results and analysis reveal that the activation energy for the motion of smooth, flat grain boundaries is inversely proportional to the driving force. Realistic driving forces are typically around 10^{-3} meV/atom (10^{-2} MPa), compared with a minimum of 1 meV/atom (10 MPa) accessible in simulations. Thus in the experimental (zero-force) limit the activation energy is infinite and the migrated grain boundary is never stabilised. An important and fully unexpected result of this study is that smooth, flat grain boundaries are thus immobile and the concept of an "intrinsic mobility" is meaningless. Of course, real grain boundaries are never perfectly flat: at high temperatures they become rough [1] and in all cases they contain structural defects such as extrinsic secondary grain boundary dislocations and steps [2]. Both effects remove the requirement for homogeneous island nucleation and so enable boundary migration.

References

1. Olmsted, D.L.; Foiles, S.M.; Holm, E.A.: Scr. Mater. 57 (2007) 1161.

2. Merkle, K.L.; Thompson, L.J.; Phillipp, F.: Phys. Rev. Lett. 88 (2002) 225501.
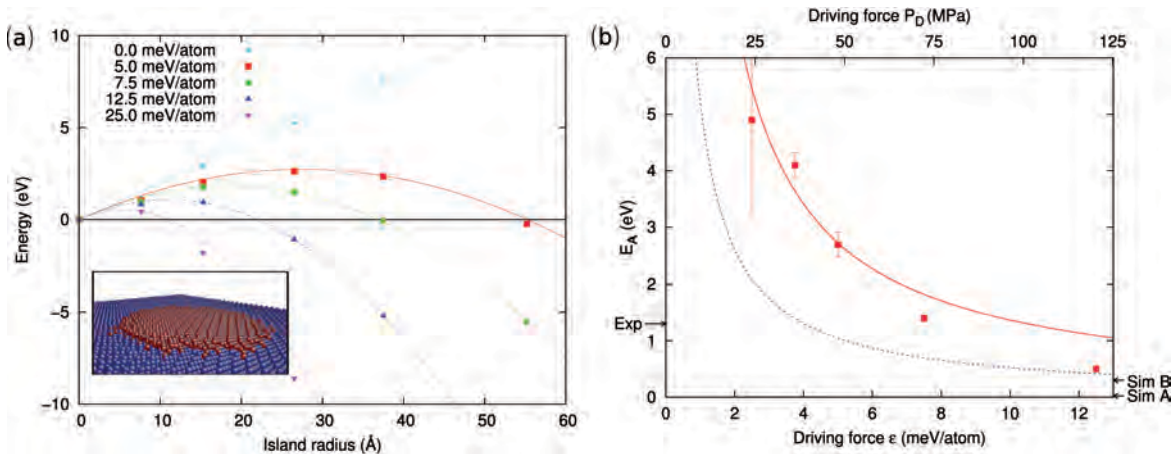
Fig. 3:. *(a) Nucleation barrier as a function of island radius. The symbols mark the results of static atomistic calculations using an EAM potential (see inset, island emphasised in red). The curves show the predictions of the simple model of island energy. (b) Activation barrier to form a stable nucleus as a function of the driving force. The symbols mark the energy barrier from boundary migration simulations; The red line shows the zero temperature free energy barrier $F^*(T = 0)$ predicted by the island model and the blue line an effective energy barrier at 550 K to enable comparison with literature benchmarks, shown on left and right axes.*

Element-Resolved Corrosion Analysis of Fe-Based Bulk Metallic Glasses

J. Klemm [1], M.J. Duarte [1,2], S.O. Klemm [1], A.M. Mingers [1], M. Stratmann [1],
P.P. Choi [2], D. Raabe [2], K.J.J. Mayrhofer [1], F.U. Renner [1]

[1] Department of Interface Chemistry and Surface Engineering
[2] Department of Microstructure Physics and Alloy Design

The complex elemental mixture in modern alloy systems often allows for extraordinary mechanical properties, but also constitutes a major challenge in corrosion science. Since all metals and compounds are fundamentally unique in their electrochemical behavior, the interactions between alloy constituents are decisive for the stability and applicability of materials. The individual role of each metal atom in macroscopic corrosion phenomena is important, and therefore requires element-resolved testing methods to fundamentally understand the underlying process. However, this element-specific perspective is strongly affected by the environment of metal atoms in the alloy. Under this aspect, particularly interesting are amorphous alloys or bulk metallic glasses (BMG) [1] which completely lack long range order [1,2]. This causes a perfectly homogeneous distribution of different elements in the matrix, an extremely rare feature in crystalline alloys due to the chemical segregation during phase formation.

In this study, the amorphous Fe-based model system $Fe_{50}Cr_{15}Mo_{14}C_{15}B_6$ was gradually crystallized by thermal heat treatment, characterized on the near-atomic scale by atom probe tomography (APT), and investigated with a novel element-resolved corrosion testing methodology in various states of crystallinity. This methodology allows following the effect of crystallization or chemical partitioning on the corrosion behavior and clarifies the element-specific dissolution, both being key challenges in modern corrosion science.

Fig. 1 shows the effect of an electrochemical corrosion test, where the samples were polarized for 1000 s in 0.1 M H_2SO_4 at each individual break-down potential, on the surface topography of amorphous, partially nanocrystalline (620°C) and fully nanocrystallized (800°C) specimens. The amorphous sample only displays a minor change in topography (A). The partially nanocrystalline (620°C) surface demonstrates then a severe surface roughening on the nanometer length-scale. Finally, the fully nano-crystalline sample is covered by deep etch pits (C).

Phases with different elemental composition are evident from X-ray diffraction and APT, revealing local chemical changes in the material. To investigate the complex multi-element corrosion performance and clarify the topographic effects observed with atomic force microscopy (AFM), a micro-electrochemical scanning flow cell (SFC) [3] was coupled to a highly
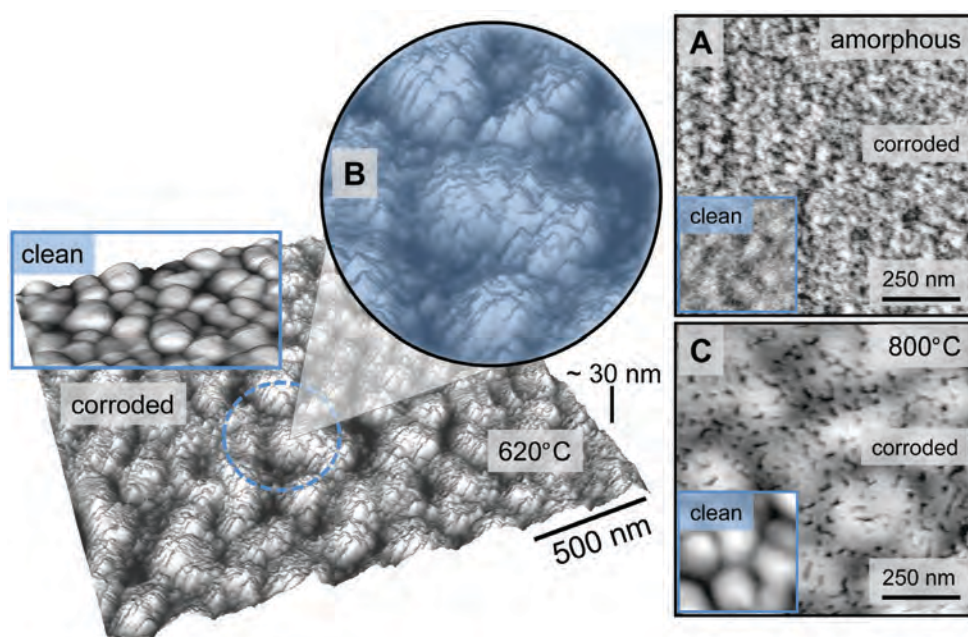

Fig. 1: *(A) AFM topography imagesof rough surfaces after corrosion test and corresponding clean surfaces (left corner, with blue edges) of (A) amorphous sample (B) 620°C sample (C) 800°C sample.*
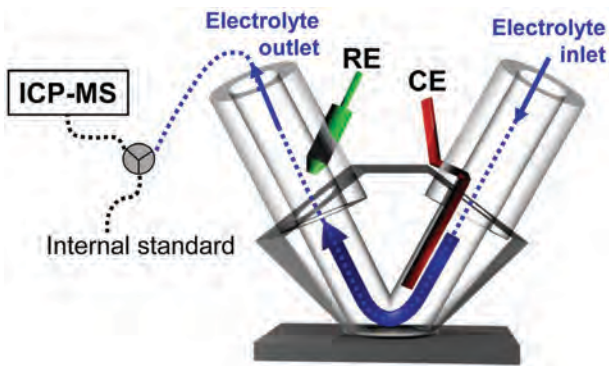
Fig. 2: *Schematic figure of the SFC coupled to an ICP-MS setup.*

sensitive ICP-MS (inductively coupled plasma mass spectrometry) [4,5] recording metal dissolution in real time. The setup is sketched in Fig. 2.

The corrosion behavior of the different alloys was investigated by linear sweep experiments in 0.1 M H_2SO_4 (Fig. 3 A-C black line). The results show a clear transition from a passive state limited by transpassive Cr dissolution (for amorphous and 620°C) to an early breakdown governed by Mo dissolution (for 800°C). The coupling of the SFC to the ICP-MS enables a direct comparison between the electrochemical (current density, i_m) and the analytical data (dissolution current density, i_{Diss}).The measured concentrations were converted into current density by application of Faraday's law [4,6]. The sum of all three individual elemental dissolution current densities, $i_{Diss,Me}$ with Me = Fe, Cr, Mo, (grey dashed lines in Fig. 3 A-C) show a good agreement with the measured current density i_m for all three samples. Interestingly, significant changes are observed for the element-specific dissolution stoichiometry derived from the profiles, compared with the bulk material composition (Fig. 3 D-F).For the amorphous sample the main species dissolved is Fe with understoichiometric dissolution of Cr in the low potential range up to 700 mV, indicating enrichment of Cr at the outer passive layer. At higher potentials, i.e. the passive range, both Mo and Cr dissolve in equivalent ratio. An even higher contribution of Fe and Mo is observed in the sample annealed at 620 °C. Cr dissolves stoichiometrically only at the breakdown. At last, a very strong contribution of Mo approaching to the Fe signal is detected in the fully crystalline alloy, with Cr being distinctly minor.

The fully amorphous material thus shows chromium enrichment with low initial current densities. Accordingly, those surfaces remain comparably smooth. The partially crystalline alloy shows an enhanced dissolution of Fe and Mo throughout the polarization test, originating from Cr-depletion in the matrix confirmed by APT. The existence of nanoscopic, stable phases in a Cr-depleted matrix leads to a roughening, clearly observed in AFM. The etch pits observed for the fully crystalline samples however can be attributed to a Cr-depleted Mo-rich phase, which prevents passivity. The level of insights gained from element resolved corrosion tests and the synergies with other methods of surface science prove this concept to be highly valuable for modern corrosion research.
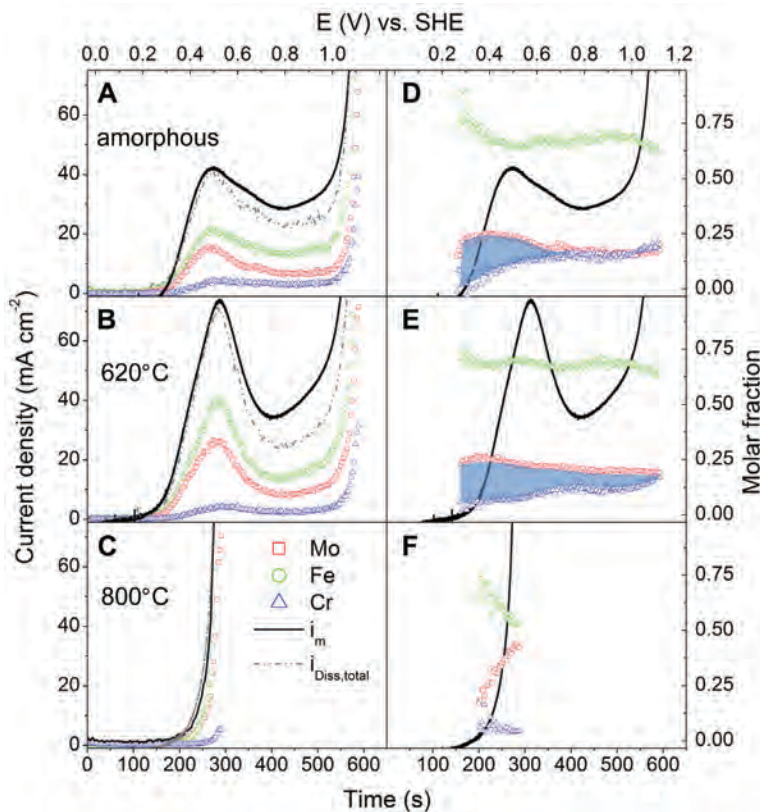
Fig. 3: (*A-C*): *Potential sweep data i_m (black continuous line) and online-ICP-MS dissolution profiles converted into dissolution current densities in 0.1M H_2SO_4 for the three samples. (D-F): Potential sweep data, i_m, with overlaid dissolution stoichiometry expressed as molar fractions of Fe, Cr and Mo. The difference between Mo and Cr dissolution is highlighted in blue (D-E).*

References

1. Inoue, A.: Acta Mater. 48 (2000) 279.

2. Greer, A.L.: Science 267 (1995) 1947.

3. Klemm, S.O.; Schauer, J.-C.; Schuhmacher, B.; Hassel, A.W.: Electrochim. Acta 56 (2011) 4315.

4. Klemm, S.O.; Topalov, A.A.; Laska, C.A.; Mayrhofer, K.J.J.: Electrochem. Commun. 13 (2011) 1533.

5. Homazava, N.; Ulrich, A.; Krähenbühl, U.: Spectrochim. Acta Part B: Atomic Spectrosc. 63 (2008), 777.

6. Ogle, K., Mokaddem, M.; Volovitch, P.: Electrochim. Acta 55 (2010) 913.

Surface Cracking on Cu−Au Surfaces

G.N. Ankah[1], D. Ma[2], M. Nellessen[2], D. Raabe[2], F.U. Renner[1]

[1] Department of Interface Chemistry and Surface Engineering, [2] Department of Microstructure Physics and Alloy Design

Cracking of structural materials is undoubtedly a very dangerous, often catastrophic issue in structural materials. For the understanding of the cracking behavior of materials the nucleation and initial growth is of special importance and often the decisive step for the evolution of a macroscopic crack. This is true on one hand, for cracking processes inside the bulk as it may occur during aging of materials. On the other hand many cracks initiate and start on the surface or the surface-near region as for example in the case of stress-corrosion cracking (SCC). Cracking is difficult to predict, both theoretically and experimentally. Typically, cracking events become only visible when they have already grown to a considerable size and the (atomic-scale) initiation and nucleation is not captured.

SCC is an often catastrophic failure process that occurs with specific alloys and environments that otherwise show a low corrosion rate. Many materials are susceptible to SCC but naturally high strength structural materials are of particular importance. Historically, the problem was observed in brass materials and Cu−Au alloys have been addressed as model systems for SCC in the last century. Although a longstanding topic in fundamental research there is no conclusive insight and many debates in the literature remain [1-3].

In this respect our recent discovery of microcracks on thiol-inhibited Cu−Au alloy surfaces during dealloying opens a promising way to address the cracking behavior and in particular crack initiation in alloys [4,5]. Compression studies using micropillars by Cynthia Volkert et al. showed active 111 slip modes in pure Au while nanoporous Au showed a foam-like behaviour [6,7]. Astonishingly the cracks on the thiol-modified Cu_3Au surfaces possessed a nanoporous Au core with a clear sign of crystallographic fracture directions along the surface (Fig. 1). The different thiols used (from left to right) include benzeneselenol, hexadecanethiol (HDT) and mixed-aminobenzenethiol (m-ABT). The number of occurring cracks was observed to depend on the kind of initial surface treatment and the crack density varied strongly with surface orientation as shown in Fig. 2a (next page). Fig. 2b is a cross-sectional micrograph showing the morphology of one such crack within the nanoporous material.

The cracks that are observed might develop from the stressed ultrathin Au-rich film which then extends into the nanoporous material. The developing stress might be expected to be large since the thiol self-assembled films suppress the surface mobility of the Au atoms. In contrast to the localized corrosion of the inhibited systems, clean Cu_3Au selectively dissolves
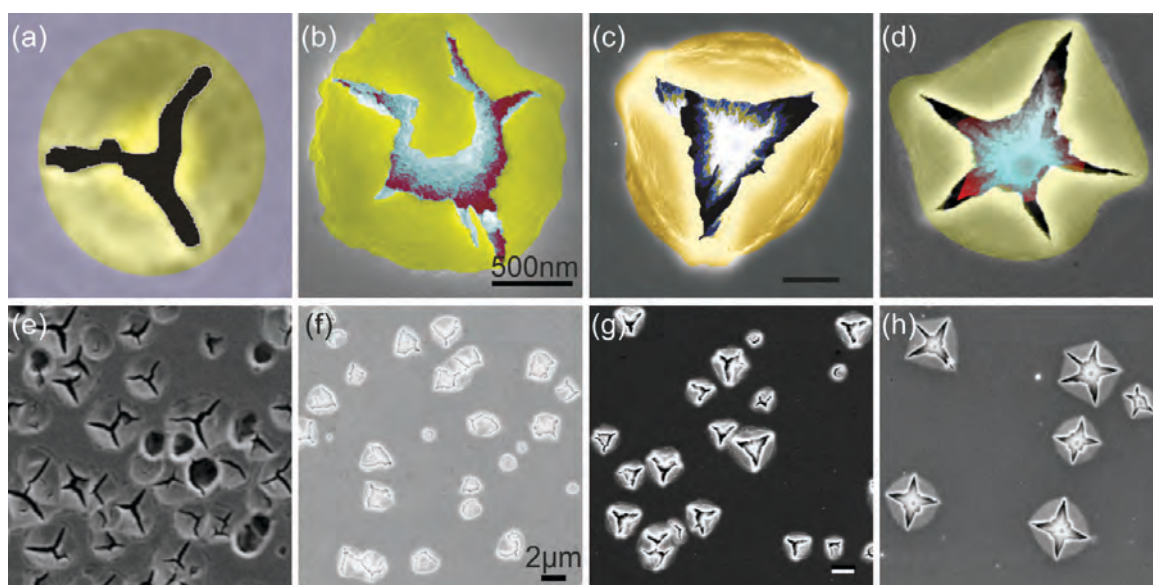

Fig. 1: *SEM images showing cracks on differently treated single and polycrystalline Cu_3Au surfaces after dealloying in 0.1 M H_2SO_4: benzeneselenol (a and e), hexadecanethiol (b and f), and mixed-aminobenzenethiol (c, d, g and h) modified surfaces.*
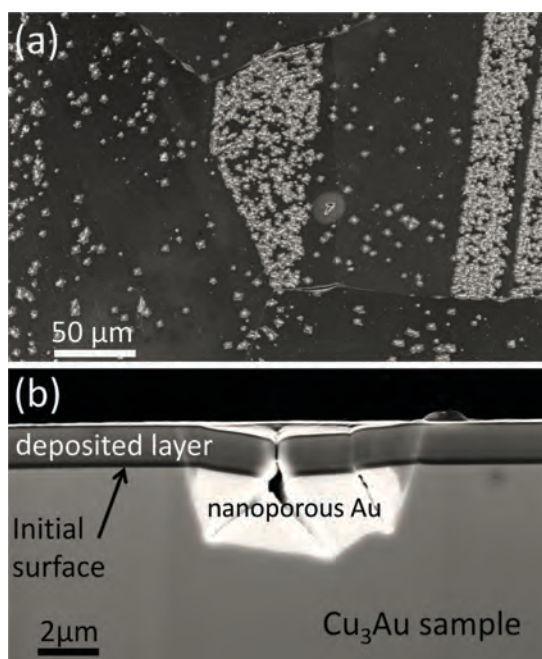
Fig. 2: *Scanning electron micrographs of a dealloyed Cu_3Au polycrystalline sample. (a) Plane view showing grains with different crack densities. (b) Cross-section showing one specific crack that extends into the nanoporous material.*

and forms a homogeneous nanoporous structure. According to surface and cross-sectional analysis with EBSD, (110) grains were determined to have the highest density of cracks.

In a first step the stress development of the nanoporous gold and the Cu_3Au matrix is described by a simple model solved by finite element method: we assume a half sphere will develop into porous Au from the surface of bulk Cu_3Au. The development of porous Au is mimicked by shrinking the half sphere
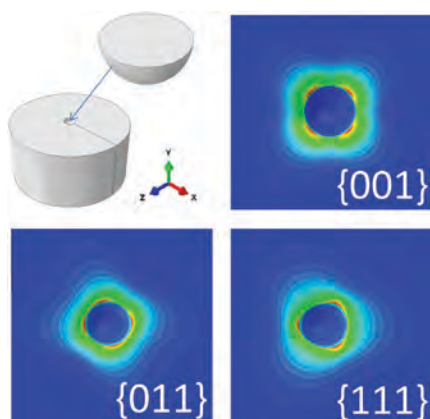
down to 70% of its original volume. Anisotropic elastic properties are assigned to both porous Au and Cu_3Au. The crystallographic orientation of Au and Cu_3Au are the same. For simplicity the ultrathin stacking reversed gold top layer is neglected. As shown in Fig. 3, during the shrinkage of the half sphere, stress concentration is built up in certain crystallographic directions. For instance, when (111) plane is parallel to the surface, the stress concentration will be in [$\bar{2}$ 1 1], [$\bar{1}$ $\bar{1}$ 2], and [$\bar{1}$ 2 $\bar{1}$] directions, where the elastic stiffness is the highest.

Finally, the present work shows that the Cu_3Au system evolves with "pronounced" microscopic failure when functionalized e.g. with thiol self-assembled films. This leads to a build-up of stresses, which are released abruptly hence generating cracks. Why the crack density is particularly high for the (110) orientated surfaces is still being investigated and one approach to better understand this effect is to conduct corresponding micromechanical simulations using an anisotropic elastic finite element model. Using a Cu_3Au (111) single crystal, the crack tips with a common origin were found to follow a threefold rotational symmetry of the fcc-like Cu_3Au (111) surface pointing to {110} cracks for selenole and {111} for thiol-modified surfaces. Many significant issues are still open for future research in this field of cracking during selective dissolution, including atomistic simulations, correlation with SCC, or a comparative study with other systems such as Cu−Pd or Ag−Au. The observed crack behavior in inhibited dealloying process as provided in this report may be of great importance to understanding crack initiation in general, especially if atomistic modeling contributes in establishing this concept.

Fig. 3: *Von Mises Stress Contour plots showing the stress concentration distribution (color code: red is high and blue is low).*

References

1. Newman, R.C.: Corr. Sci. 50 (2008) 1807.

2. Friedersdorf, F.; Sieradzki, K.: Corrosion 52 (1996) 331.

3. Kaiser, H.; Eckstein, G.A.: Corrosion of alloys, in: Encyclopedia of Electrochemistry, Vol.4, Wiley-VCH, Weinheim, 2003.

4. Pareek, A.; Borodin, S.; Bashir, A.; Ankah, G.N.; Keil, P.; Eckstein, G.A.; Rohwerder, M.; Stratmann, M.; Gründer, Y.; Renner F.U.: J. Am. Chem. Soc. 133 (2011) 18264.

5. Renner, F.U.; Stierle, A.; Dosch, H.; Kolb, D.M.; Lee, T. L.; Zegenhagen, J.: Phys. Rev. B. 77 (2008) 235433.

6. Volkert, C.A.; Lilleodden, E.T.: Philos. Mag. 86 (2006) 5567.

7. Volkert, C.A.; Lilleodden, E.T.; Kramer D.; Weissmüller J.: Appl. Phys. Lett. 89 (2006) 061920.

Fundamental Studies on Novel Self-Healing Concepts for Corrosion Protection of Galvanized Steel

A. Vimalanandan, T.H. Tran, M. Rohwerder

Department of Interface Chemistry and Surface Engineering

Corrosion is a widespread problem with significant economic impact. Its consequences are also a loss of resources, energy, and the release of toxic substances to the environment. The latter aspect does not refer only to metallic cations (such as nickel) but also to corrosion inhibitors. Corrosion inhibitors are added to organic coatings applied for corrosion protection, the main measure for achieving efficient corrosion control for application in the automotive, aerospace, construction and appliances industries. The release of the inhibitors, however, does not occur in a controlled way. Instead, the inhibitors are continuously leached out of the coating. If corrosion in a defect occurs, they are then available for suppressing it. If there is no corrosion, they are fully released into the environment, continuously. Most of the current inhibitors are in discussion to be environmentally detrimental. Obviously, the best concept would be coatings that are capable of case triggered (i.e. only when corrosion occurs) release of active agents that stop corrosion and heal the corresponding defect (self-healing). Such coatings would not release great quantities of chemicals to the environment and still provide a superior corrosion protection. The idea of our research on intelligent corrosion protection is to develop coating systems that can do that. The best trigger is the change of potential. Conducting redox polymers are sensitive to changes in potential. However, their safe application for corrosion protection, especial on the technically very relevant zinc is a problem where the formation of an insulating layer leads to de-activation of the conducting polymer [1]. The research on developing reliable coating systems for intelligent release of active agents from conducting polymer is currently carried out within the framework of a DFG project (Heapocrates), in close cooperation with the Max-Planck-Institut für Polymerforschung (Prof. Landfester, Dr. Crespy). One of the main problems for achieving good self-healing is to store sufficient active agents for also closing defects larger than a pinhole. Synergy between components stored in the zinc coating, zinc cation themselves and components stored in the organic or hybrid inorganic-organic coating is the approach investigated in the framework of the MPG-FhG funded Project "ASKORR" in order to achieve this. As a first step synergetic effects between compounds stored in silica capsules in the zinc coating [2] with zinc cations released by zinc corrosion were investigated on exposed iron (defect down to the iron).

The zinc coating dissolves to protect steel while the oxygen reduction takes place on steel which causes a pH gradient on it. Close to zinc the pH is
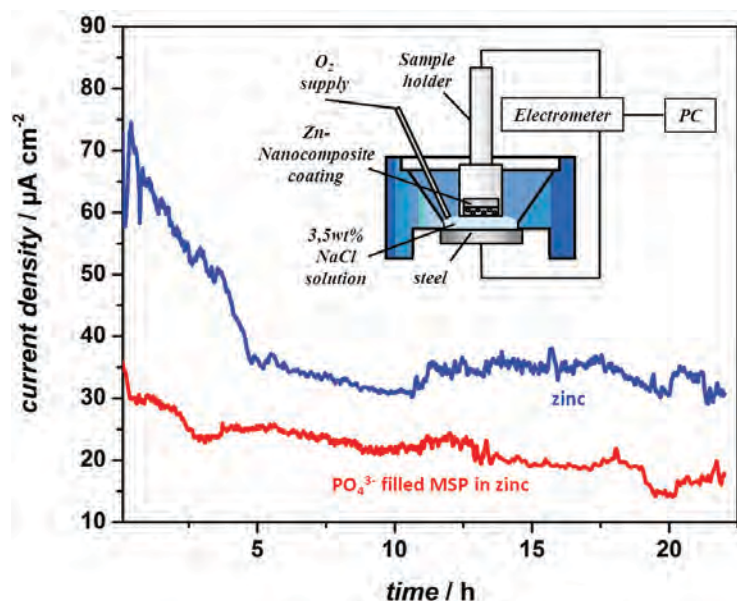

Fig. 1: *Experimental set-up for the galvanic current measurement and results showing the suppression of current density by phosphate loaded MSP embedded inside the zinc layer.*
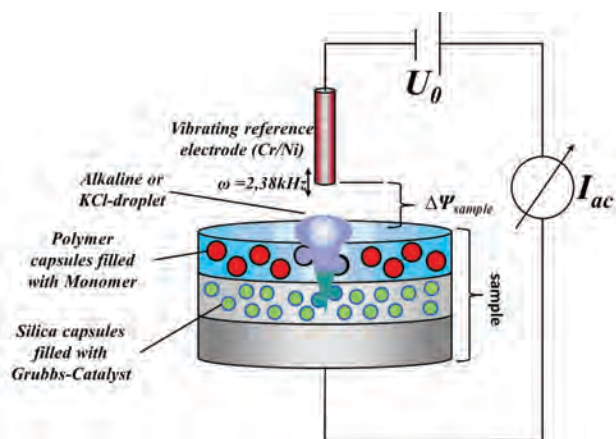
Fig. 2: *Experimental set-up of the self-healing experiments: the corrosion potential in the small scratch is monitored by Kelvin probe. Light blue: organic coating, grey: zinc coating.*
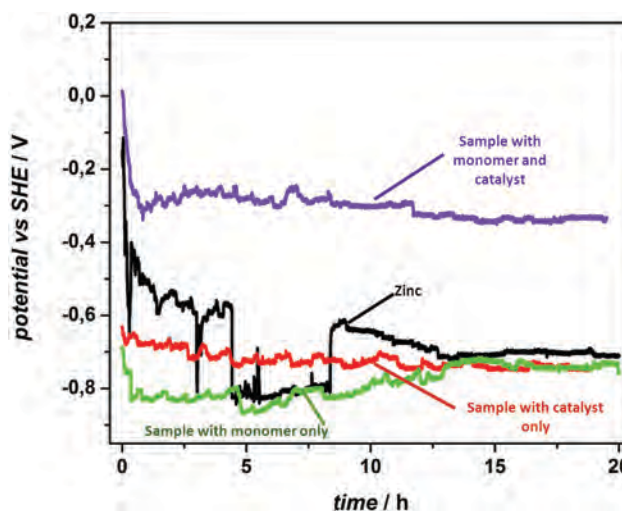

Fig. 3: *Proof-of-principle of the self-healing concept by polymerization. Only the sample with monomer and catalyst shows a self-healing behavior (passive potential). Reference measurements without or with just one component show constant active behavior.*

slightly acidic to neutral, further away the pH is highly alkaline. Hence, only at these alkaline pH the silica particles are dissolved and the stored inhibitors are released and can react with zinc cations to form a better protective corrosion product layer (see Fig. 1). The important point is: unlike release from classic pigments the release is delayed in time, by the diffusion of the capsules to the alkaline steel surface and hence the inhibitor is not consumed at the edge of the defect, where they are of little use, but right in the defect. This example shows how intelligent corrosion inhibition may be realized in future. However, full self-healing also requires the growth of a new organic coating in the defect. The best way is release of monomers and their targeted polymerization in the defect (and only there). This is done in the following way: polymerization catalysts are stored in silica capsules inside the zinc coating, where these reactive components can be stored for years without danger of de-activation by oxygen from the air. As they are released time-delayed, the monomers released from capsules in the primer have time to diffuse to the defect where the targeted polymerization will occur, leading to full coverage of the defect. One of the central topics of current research, in close cooperation with the project partners, is to find the optimal capsule systems for the primer: ideally conducting polymers or other redox active capsule materials should be used. In first test experiments, the capsule opening was just mechanically induced at the edge of the scratch through the coating. As in these experiments the amount of available active agents is very low (it should be higher, if release as a consequence of corrosion triggered delamination is triggered from a broader area surrounding the defect), experiments were focused on simulating atmospheric corrosion conditions where just a small amount of electrolyte is present at the defect. For this the experiments were controlled by Kelvin probe (see Fig. 2). After intense research and optimizing steps, successful self-healing was achieved (see Fig. 3). Better performance is expected when broader triggered release can be achieved by use of redox active capsules in the primer. Conducting polymer capsules modified by spacer groups to prevent deactivation are currently successfully developed in Heapocrates and additional redox active capsule materials tested within ASKORR.

References

1. Rohwerder, M.; Isik-Uppenkamp, S.; Amarnath, C.A.: Electrochim. Acta 56 (2011) 1889.

2. Khan, T.R.; Erbe, A.; Auinger, M.; Marlow, F.; Rohwerder, M.: Sci. Technol. Adv. Mater. 12 (2011) 055005.

SELECTED HIGHLIGHTS

Understanding the Mechanism of the Oxygen Reduction Reaction

I. Katsounaros[1], W.B. Schneider[2,3], J.C. Meier[1], U. Benedikt[2],
P.U. Biedermann[1], A.A. Auer[2], K.J.J. Mayrhofer[1]

[1] Department of Interface Chemistry and Surface Engineering
[2] Max-Planck-Institut für Chemische Energiekonversion, Department of Theoretical Chemistry, Mülheim an der Ruhr, Germany
[3] Ruhr-Universität Bochum, Center for Electrochemical Sciences, Bochum, Germany

The oxygen reduction reaction (ORR) is a fundamental reaction related to various disciplines such as energy conversion, material dissolution or biology. Recently, particular interest focused on its essential role in fuel cells or lithium-air batteries. However, the mechanism of the ORR on metal surfaces remains unclear. The distinction between the ORR mechanisms is based on the number of proton-coupled electron transfer steps that precede the O–O bond breaking step (Fig. 1). Among these mechanisms, hydrogen peroxide can be formed as an intermediate of ORR only by the 2nd associative mechanism. Indeed, hydrogen peroxide has been detected under certain conditions during ORR, but it remains unclear whether it is a key intermediate of the dominant ORR mechanism or a side-product [1]. A detailed understanding of the interaction of H_2O_2 with metal surfaces is essential on the road to understanding the ORR mechanism.

In weakly adsorbing electrolytes such as $HClO_4$, the total rate of H_2O_2 decomposition on polycrystalline Pt is controlled by mass transport, in the potential region between +0.2 V_{RHE} and +1.5 V_{RHE}. In this region, the currents in the cyclic voltammograms (CVs) scale with the thickness of the diffusion layer and with the bulk concentration of H_2O_2 [2,3]. In addition, electrolysis experiments performed under potentiostatic conditions indicate that the rate of decrease of H_2O_2 concentration with time is diffusion-limited, regardless of the applied potential. This means that during ORR in such a system,
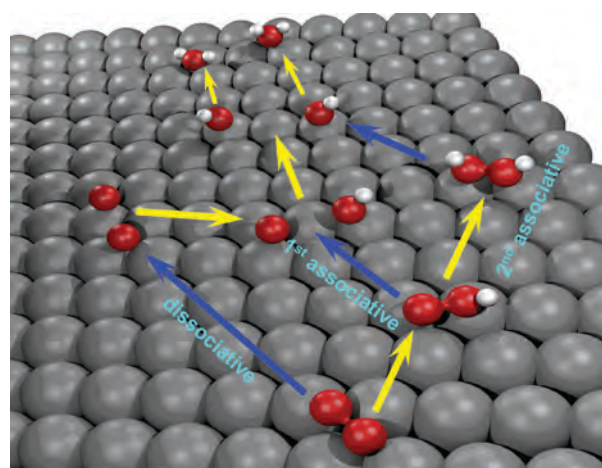
Fig. 1: *Proposed oxygen reduction reaction mechanisms.*

H_2O_2 cannot be detected in the electrolyte even if it is formed at the interface. In a peroxide-containing solution, the potential-dependent Pt surface state triggers the corresponding reaction: Upon interaction with reduced surface atoms at low potentials, H_2O_2 adsorbs dissociatively producing OH_{ads}, while upon interaction with an oxidized surface at high potentials, H_2O_2 gets oxidized to O_2 by reducing the surface [3]. The measured current is the sum of the two partial currents restoring the thermodynamically preferred surface state at a given potential. Quantum chemical *ab initio* calculations (Fig. 2) showed that
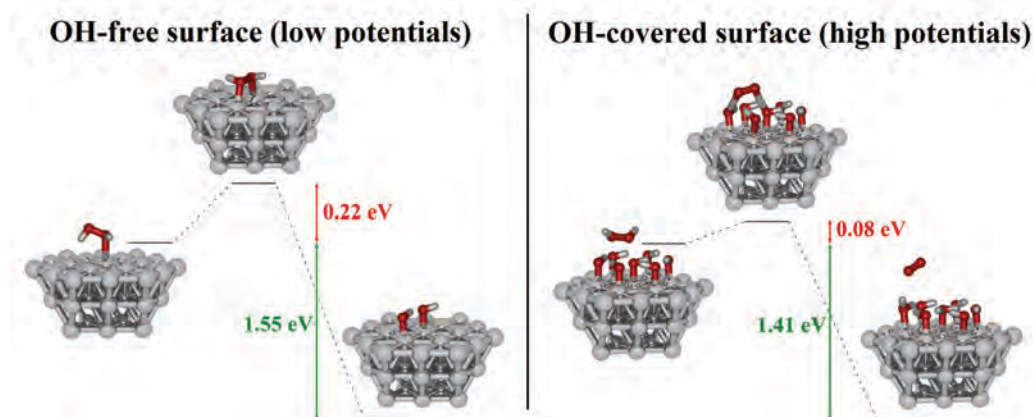
Fig. 2: *Energy diagram for the dissociation of H_2O_2 on a bare Pt(111) surface and for the oxidation of H_2O_2 on an OH-covered surface.*
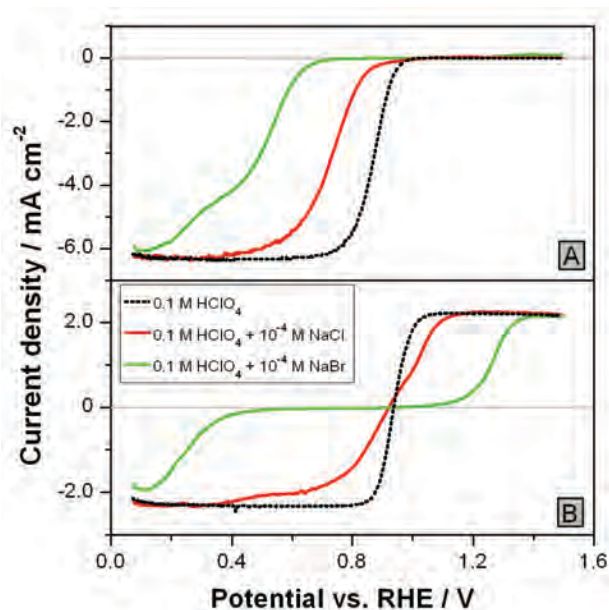
Fig. 3: *The impact of the halide ions on the background-corrected hydrodynamic voltammograms (1600 rpm) in (A) O_2-saturated electrolytes and (B) Ar-saturated electrolytes additionally containing 1×10^{-3} M H_2O_2. Scan rate: 0.1 V s^{-1}.*

the activation barriers for either H_2O_2 dissociation or oxidation are easily overcome by the thermal energy and the reactions will proceed with a high rate at room temperature [2].

Therefore, the kinetics of both reactions of H_2O_2 dissociation (at low potentials) and H_2O_2 oxidation (at high potentials) are very fast as long as there is sufficient availability of platinum sites capable of carrying out any of the two reactions. This condition is fulfilled in weakly adsorbing electrolytes, where the coverage from inhibiting adsorbates is low. In particular, at potentials relevant to the ORR (i.e. below 0.95 V_{RHE}) the barrierless cleavage of the O–O bond of H_2O_2 is not prevented by the adsorption of inhibiting adsorbates.

The adsorption of halide spectator species limits the availability of sites that can break the O–O bond of O_2 and H_2O_2 [4]. The effect becomes stronger the higher the concentration of the halides in the electrolyte. Chloride adsorption inhibits the dissociative adsorption of O_2 more strongly than

that of H_2O_2 (Fig. 3), implying that a larger number of adjacent Pt atoms is required to break the O–O bond of O_2, compared to H_2O_2. When a larger ion is added (such as bromide) the situation changes, and the inhibition of $H_2O_2$ reduction becomes stronger than that of O_2 (Fig. 3). This is because the O–O bond breaking is no longer possible for both O_2 and H_2O_2; however, there are still some single non-covered Pt atoms able to carry out the reduction O_2 to H_2O_2 without O–O bond cleavage. Therefore, depending on the extent of the inhibition of peroxide´s O–O bond breaking, the total rate of H_2O_2 decomposition may not be anymore limited by the mass transport of H_2O_2, which translates to a local H_2O_2 concentration higher than zero. In that case, during ORR under that conditions, the macroscopic detection of H_2O_2 as an intermediate of ORR will be possible at potentials where the coverage from the inhibiting spectators is sufficiently high.

In summary, H_2O_2 is unstable on Pt surfaces and it will immediately dissociate to OH if formed during ORR, unless the cleavage of the O–O bond is inhibited by adsorbed spectator species. The study of the interaction of H_2O_2 with Pt in conditions relevant to ORR, corroborates with previously reported data on the macroscopic H_2O_2 formation during ORR and can explain why hydrogen peroxide has been detected under certain conditions. Therefore, the differences in the proposed ORR pathways based on experimental data are an artifact and originate only from the changes in the interface structure caused by spectators.

References

1. Nørskov, J.K.; Rossmeisl, J.; Logadottir, A.; Lindqvist, L.; Kitchin, J.R.; Bligaard, T.; Jónsson, H.: J. Phys. Chem. B 108 (2004) 17886.

2. Katsounaros, I.; Schneider, W.B.; Meier, J.C.; Benedikt, U.; Biedermann, P.U.; Auer, A.A.; Mayrhofer, K.J.J.: Phys. Chem. Chem. Phys. 14 (2012) 7384.

3. Katsounaros, I.; Mayrhofer, K.J.J.; Chem. Commun. 48 (2012) 6660.

4. Katsounaros, I.; Schneider, W.B.; Meier, J.C.; Benedikt, U.; Biedermann, P.U.; Auer, A.A.; Mayrhofer, K.J.J.: "Understanding the oxygen reduction reaction pathways", J. Am. Chem. Soc., *submitted.*

SELECTED HIGHLIGHTS

Developing Design Principles for Stable Fuel Cell Catalysts by Studying Degradation Processes on the Nanoscale

J.C. Meier [1], C. Galeano [2], A. Kostka [3], V. Peinecke [4], F. Schüth [2], K.J.J. Mayrhofer [1]

[1] Department of Interface Chemistry and Surface Engineering
[2] Department of Heterogeneous Catalysis, Max-Planck-Institut für Kohlenforschung, Mülheim an der Ruhr, Germany
[3] Department of Microstructure Physics and Alloy Design
[4] The fuel cell research center ZBT GmbH, Duisburg, Germany

Proton exchange membrane fuel cells are among the most promising technologies to replace traditional combustion engines and thus offer a clean and sustainable energy supply for automotive industry (if combined with renewable energy sources). The state of the art fuel cell catalyst is based on platinum nanoparticles dispersed on a carbon support, providing a high electrochemical active surface area (ECSA) of platinum to catalyze the oxidation of the hydrogen fuel at the anode, as well as the necessary oxygen reduction at the cathode. Under certain operation modes, however, the electrocatalyst limits the lifetime of a fuel cell. Particularly on the cathode side during start up and shut down the catalyst faces most drastic conditions such as low pH values, elevated temperatures, high potentials as well as harmful potential fluctuations. As a consequence the catalyst degrades over time, resulting in a decrease in platinum surface area and a loss in overall performance of the fuel cell [1,2].

One major obstacle in the design of catalysts with improved stability is the lack of knowledge about the underlying degradation processes of fuel cell catalysts on the nanoscale. To address this issue we developed the identical location approach for transmission electron microscopy (IL-TEM) [3-5]. IL-TEM visualizes the same catalyst location before and after an applied degradation protocol, which has not been accessible before. An example of a catalyst location studied via IL-TEM is shown in Fig. 1.

Moreover, the identical location approach has been extended also to other electron microscopic techniques such as SEM, or even electron tomography, which add complementary information to a standard IL-TEM experiment [5]. While TEM only provides a 2D projection of a three-dimensional object, IL-tomography can visualize changes in a catalyst material due to an electrochemical aging test in 3D. An IL-tomography representation of a Pt/Vulcan catalyst is visualized in Fig. 2C and 2D (see next page) and compared to standard IL-TEM images of the identical catalyst location (2A, 2B). Particle growth due to agglomeration as well as detachment can be clearly observed for the standard Pt/Vulcan material. Additionally the breaking off of a complete carbon fraction from the catalyst aggregate was visualized. This carbon fraction was originally connected to the main aggregate via small carbon bridges, which corroded during the simulated start-stop conditions [6].

The knowledge about the strong contribution of detachment and especially agglomeration to the overall degradation of the standard Pt/Vulcan catalyst during start-stop – as disclosed by IL-TEM and IL-tomography – was applied in the design of a more stable catalyst. Namely, a hollow graphitic carbon sphere support (HGS) with a three-dimensional interconnected mesoporous network was synthesized and loaded with platinum. After a thermal treatment step a highly stable fuel cell catalyst with platinum particles in a size range of 3-4 nm incorporated in the mesoporous structure (Pt@HGS$_{900°C}$) is obtained. Measurements in an electrochemical half cell demonstrated standard activity and superior stability for this material. *In situ* fuel cell tests confirmed the results

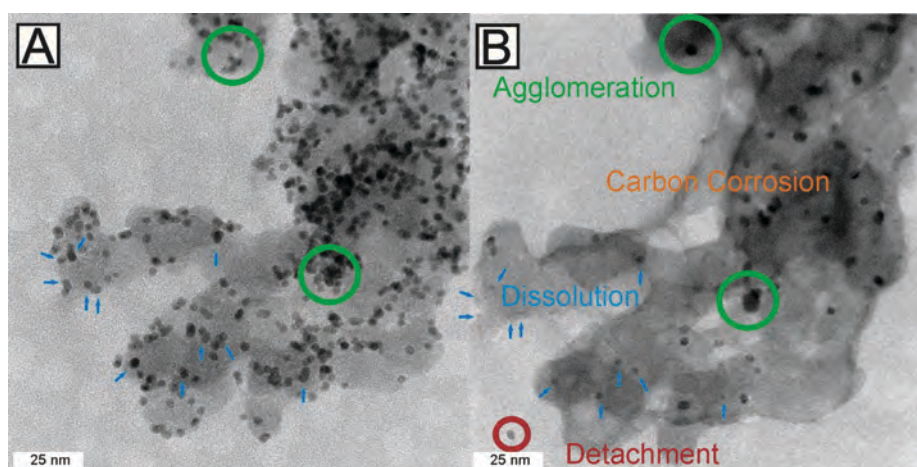**Fig. 1:** *IL-TEM micrograph a Pt/Vulcan catalyst before (A) and after (B) 3600 potential cylces between 0.4 and 1.4 VRHE in 0.1 M HClO4 at 1 Vs-1. Several overlapping degradation processes can be observed: Green circles indicate particle growth, the red circle highlights a detached particle, blue arrows point at dissolving particles (printed from our publications [6] with permission of ACS Catalysis).*
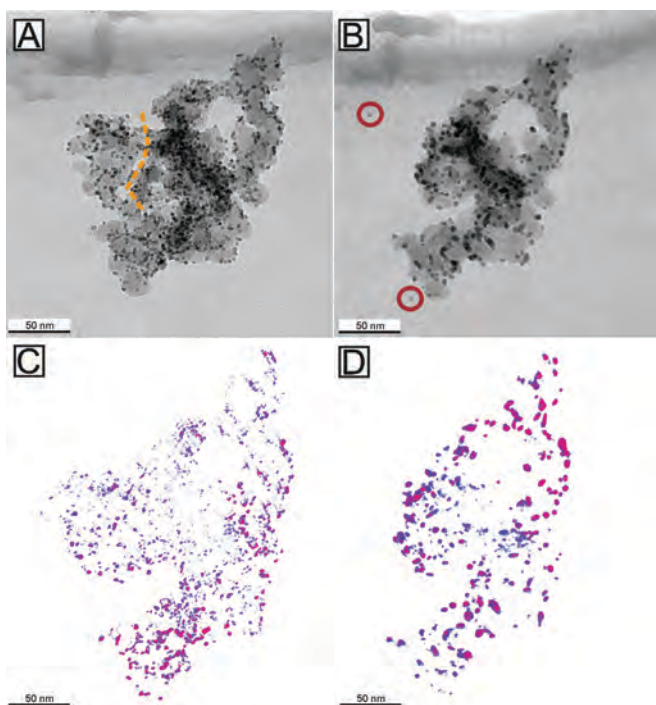
Fig. 2: *IL-TEM micrographs (A, B) and IL-tomography images (C, D) of Pt/Vulcan before (A, C) and after (B, D) 3600 potential cylces between 0.4 and 1.4 V_{RHE} in 0.1 M $HClO_4$ at 1 Vs^{-1} (printed from our publication [6] with permission of ACS Catalysis).*

the porous network are observed to vanish preferentially after the degradation test, while in total only about 14% of all particles are lost. Based on the combined IL-SEM and IL-STEM investigations it can be stated that particles located within the mesoporous network are stabilized as they are less likely to detach and agglomerate. This proves that stabilization due to confinement of platinum particles in a mesoporous network can be a valuable strategy to design more robust electrode materials.

In this study insights from IL-TEM and IL-tomography into catalyst stability were successfully employed for the synthesis of a more stable catalyst, which opens new perspectives for a more systematic design of stable electrode materials.

References

1. Mench, M.M., Kumbar, E.C.; Veziroglu, T.N.: Polymer Electrolyte Fuel Cell Degradation, Elsevier, Waltham, 2012.

2. Borup, R.; Meyers, J.; Pivovar, B.; Kim, Y.S.; Mukundan, R.; Garland, N.; Myers, D.; Wilson, M.; Garzon, F.; Wood, D.; Zelenay, P.; More, K.; Stroh, K.; Zawodzinski, T.; Boncella, J.; McGrath, J.E.; Inaba, M; Miyatake, K.; Hori, M.; Ota, K.; Ogumi, Z.; Miyata, S.; Nishikata, A.; Siroma, Z.; Uchimoto, Y.; Yasuda, K.; Kimijima, K.; Iwashita, N.: Chem. Rev. 107 (2007) 3904.

3. Mayrhofer, K.J.J.; Meier, J.C.; Ashton, S.J.; Wiberg, G.K.H.; Kraus, F.; Hanzlik, M.; Arenz, M.: Electrochem. Commun. 10 (2008) 1144.

4. Mayrhofer, K.J.J.; Ashton, S.J.; Meier, J.C.; Wiberg, G.K.H.; Hanzlik, M.; Arenz, M.: J. Power Sources 185 (2008) 734.

5. Meier, J.C.; Katsounaros, I.; Galeano, C.; Bongard, H.J.; Topalov, A.A.; Kostka, A.; Karschin, A.; Schüth, F.; Mayrhofer, K.J.J.: Energy Environ. Sci. 5 (2012) 9319.

6. Meier, J.C.; Galeano, C.; Katsounaros, I.; Topalov, A.A.; Kostka, A.; Schüth, F.; Mayrhofer, K.J.J.: ACS Catal. 2 (2012) 832.

of the half cell measurements: Pt@HGS$_{900°C}$ exhibits only minor losses in the cell voltage and therefore a superior stability under start-stop conditions compared to Pt/Vulcan, making it a highly promising material for application in real fuel cells.

Fig. 3A and 3B are an overlap of IL-SEM micrographs (green color) and IL-STEM micrographs (red color) before (3A) and after (3B) an accelerated aging test. The test reflects the high stability, as the HGS spheres stay intact and only few platinum particles are lost after electrochemical treatment. In contrary to the Pt/Vulcan catalyst no signs of agglomeration can be observed as the average particle size does not change. Particles on the surface of the spheres, which are not protected by
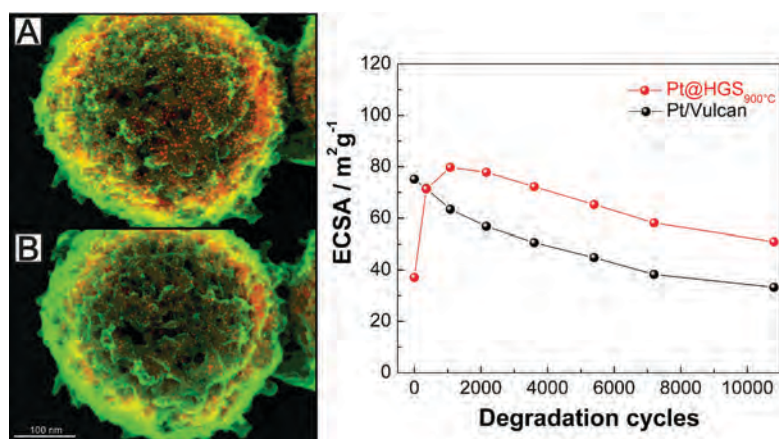

Fig. 3: *A is an image before, B after 3600 degradation cycles. A and B each show a complete carbon sphere. For both images a SEM micrograph (green) and STEM micrograph (red) were overlapped. The graph on the right demonstrates that Pt@HGS$_{900°C}$ is able to maintain a higher ECSA during an accelerated degradation test compared to Pt/Vulcan.*

In situ Investigation of Oxide Thin Film Evolution on Zinc

Y. Chen, P. Schneider, A. Erbe

Department of Interface Chemistry and Surface Engineering

Zn is one of the most important metals in applications. Due to its oxidation propensity, Zn is a very efficient sacrificial anode in cathodic protection, and used as metallic coating [1,2]. Corrosion products of Zn metal and its coatings normally include ZnO, Zn(OH)$_2$ and carbonates [1]. The electronic properties of the mostly semiconducting oxide layer have been found to play an important role in the corrosion behaviour of Zn [1,2]. Electronic structure calculations can be used to obtain detailed insight e.g. into the role of defect in different crystalline materials. On the other hand, they need to be complemented by experimental investigation of properties, such as thickness and band gap. The particular challenge in case of thin films forming in the initial stages of corrosion processes is that they are highly disordered, transient species. Formation and evolution of such structures can be conveniently analysed using optical reflection spectroscopy, as the optical absorption spectrum is directly related to the electronic structure of the film. Here, spectroscopic ellipsometry has been used to study the initial stages, as well as the evolution with time, of layer thickness and layer absorption spectrum, in controlled atmospheres and in electrolyte [3-5].

A novel method, based on a perturbation analysis [6], has been developed to extract the thickness without the need for an optical model for a layer with a thickness much smaller than the wavelength [5]. As the optical constants of zinc in the ultraviolet to visible spectral range behave Drude-like, light absorption from an ultrathin layer affects mainly the modulus of the amplitude reflection coefficient r_p for p-polarised light. The amplitude reflection coefficient r_s for s-polarised light is almost unaffected. As the ellipsometric experiment measures r_p/r_s = tan(Y) exp(i D), with i denoting the square root of -1 and the two experimental angles Y and D, a lower value of tan(Y) (or Y) compared to the metal without layer or with a non-absorbing layer follows [4]. This behaviour is demonstrated in Fig. 1.

Further, SE was used for *in situ* investigations of the Zn/electrolyte interface during both potentiostatic (chronoamperometry, CA) and potentiodynamic (cyclic voltammetry, CV) treatments of Zn in alkaline carbonate solution. During CV, the thinning of the oxide in the negative scanning and subsequent growth of oxide in the reversed positive scanning on Zn can be followed in a CV-like manner (Fig. 2).
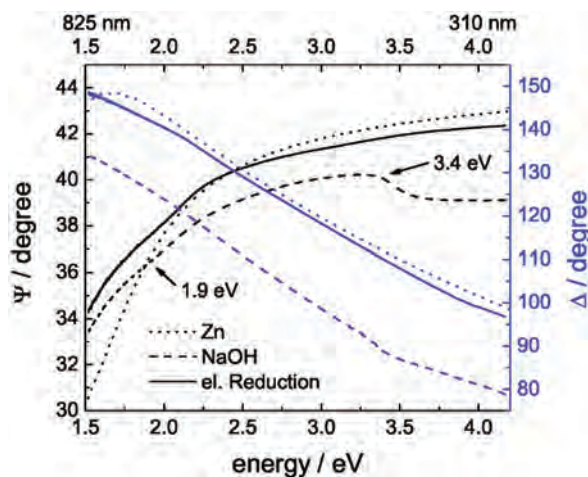
Fig. 1: *Ellipsometric spectra of zinc (dotted lines, simulated data on the basis of literature data). Treatment in NaOH (dashed lines) yields a layer with a thin oxide film, where the main electronic absorption of ZnO is visible as a downwards bend in Ψ. Electrochemical reduction results in a substantially different kind of oxide, judging from its light absorption characteristics.*

In the potential regime where the surface is oxide-covered, the layer thickness increases/decreases linearly with potential in anodic/cathodic scans, as reported for passive materials. Moreover, a rapid decrease/increase in the layer thickness in the reduction/oxidation peak has been found. Analysing the integrated currents show that oxide growth is accompanied by metal dissolution [5]. Future experiment in cooperation with experiments developed in the Electrocatalysis group should show more details about the relation between oxide formation and metal dissolution.
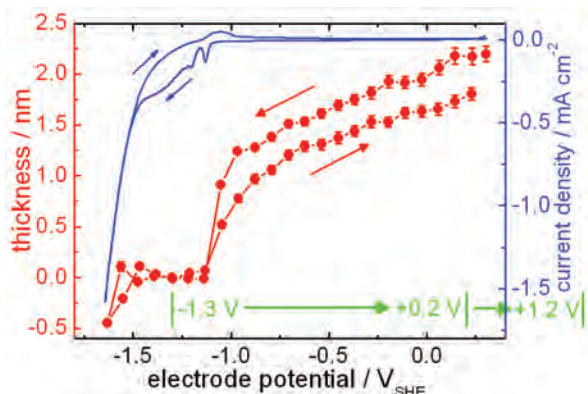
Fig. 2: *CV (blue) and ellipsometric thickness cyclic voltammogram (red) of zinc in 1 M Na$_2$CO$_3$ at 2 mV/s.*

Fig. 3: *Current densities (a) and oxide layer thickness (b) as result of chronoamperometric experiments with potential jumps. Electrode potentials were -1.3 V (0-60 min), +0.2 V (60-120 min) and +1.2 V (120-180 min).*

Fig. 4: *Spectra of Ψ during chronoamperometric experiments with potential jumps at 60 min and 120 min (as in Fig. 3). At the initial potential of -1.3 V, no oxide absorption is visible. After the first and second potential jump (to +0.2 V and +1.2 V, respectively), the slow development of the ZnO absorption at 360 nm (3.4 eV) is clearly visible.*

In the CV-type of experiments, an inspection of the layer absorption shows a behaviour which can only be understood as being due to changes with time, rather than due to changes with potential. Therefore, potential jump experiments were performed from a potential in the oxide-free region (-1.3 V), to a potential in the oxide-covered region (+0.2 V), followe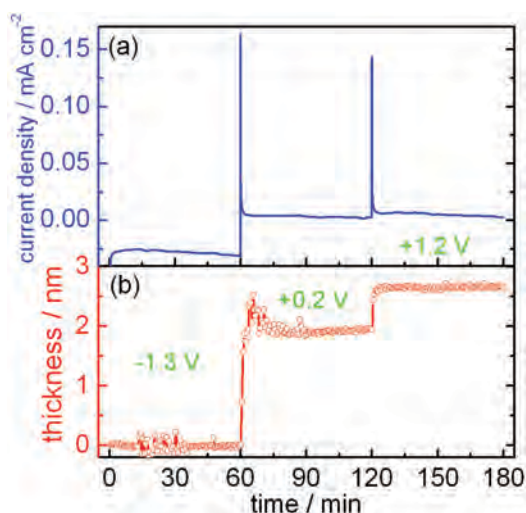d by a second jump to +1.2 V. The resulting current show a spike after the potential jump (Fig. 3a) while the thickness jumps to almost its final value within the first minute after the potential jump (Fig. 3b). On the other hand, Fig. 4 shows only a slow evolution of the electronic absorption of ZnO over ~30 min, before it remains constant until the next potential jump. Overall, these results show that the oxide layer takes time to mature. An initially formed layer is transforming slowly into ZnO. In the second phase of the layer evolution after 30 min, metal dissolution is still occurring, at a constant absorption spectrum (and hence, electronic structure) of the oxide layer. The kinetics of the layer evolution is independent of the electrode potential itself, as it behaves the same at +0.2 V as at +1.2 V [5].

While in carbonate electrolyte, the layer evolves to its final thickness faster than in 1 min while the electronic ZnO absorption evolves over ~30 min, the opposite behaviour is found when monitoring the oxide growth in argon, oxygen and air atmospheres of different humidities [4]. During atmospheric oxidation of zinc, the electronic absorption develops faster than the layer thickness. Interestingly, the oxide absorption is also fully developed after ~30 min, as in solution. The oxide layer thickness does, however, grow over hours even in argon. While oxide growth slows down with time, in most atmospheres now limiting behaviour of the growth is observed [4].

The two independent time scales for growth and ZnO electronic structure formation may be specific to zinc, which may form initial hydroxides. These hydroxides can slowly condense to finally form ZnO. On the other hand, such behaviour may be more general. Currently, oxide growth on other metals in investigated, with the aim of understanding charge transport through the layers, and the follow-up chemical reactions of the layers.

References

1. Zhang, X.: Corrosion and Electrochemistry of Zinc, Plenum Press, New York, 1996.

2. Schultze, J.W.; Hassel, A.W.: in: Encyclopedia of Electrochemistry, Vol. 4, Wiley-VCH, pp. 216-235.

3. Zuo, J.; Erbe, A.: Phys. Chem. Chem. Phys. 12 (2010) 11467.

4. Chen, Y.; Schneider, P.; Erbe, A.: Phys. Status Solidi A 209 (2012) 846.

5. Chen, Y.; Erbe, A.: Surf. Sci., *in press*, DOI: 10.1016/j.susc.2012.08.006.

6. Lekner, J.: Theory of Reflection of Electromagnetic and Particle Waves, Martinus Nijhoff, Dordrecht, 1987.

Self-Assembled Monolayers on Metals and Metals on Self-Assembled Monolayers

M.I. Muglali[1], P. Koelsch[2], A. Erbe[1], M. Rohwerder[1]

[1] Department of Interface Chemistry and Surface Engineering
[2] University of Washington, Seattle, USA

Self-assembled monolayers (SAMs) on metals can be used as low molecular models for polymers on metals. For studies of the metal/organic interface, they offer the advantage of a well-defined linkage between organic material and metal, as well as the well-known atomistic/molecular structure on both sides of the interface. Based on the long-term experience in surface modification and electrochemistry, we have investigated reactions at SAM/metal, as well as at metal/SAM interfaces in electrolyte. Electrochemical desorption/readsorption studies reveal important results concerning the nature of the interfacial interactions between a chemisorbed monolayer and a metallic substrate, besides defining the applicable potential range for SAM modified electrodes. These reactions can be seen as a molecular model for the destruction of a metal/polymer interface. Besides, they define the limit of applicability of SAMs.

Here a full investigation was carried out of the physical state of the desorbed molecules, and reactions concurrent to desorption, by combining spectroscopic techniques with electrochemisty. For these studies, Au(111) substrates have been modified by the highly ordered monolayers of 4-(4-(4 pyridyl)phenyl)phenylmethanethiol (PyPP1) [1]. The electroreductive desorption of PyPP1 SAMs shows unusual features in cyclic voltammograms (CVs). In alkaline solutions, the desorption behavior of the PyPP1 on Au is characterized by multiple reductive peaks in CVs. These peaks are, however, exceptionally large and contain one order of magnitude larger currents than expected for a simple desorption reaction (CV in Fig. 1). Based on rotating ring-disk electrode measurements, the origin of these excess currents have been found to be a concurrent rapid hydrogen evolution reaction (HER). The catalyzed HER currents appear as another peak in CVs, subsequent to thiol desorption. Confirmation of this phenomenon by *in situ* ellipsometric measurements hints to a transport mechanism in the electrochemical double layer region. *In situ* sum frequency generation (SFG) spectroscopy experiments (Fig. 1a) on PyPP1/Au(111) samples have demonstrated that PyPP1 SAMs preserve their two-dimensional order near Au during and even after the reductive desorption. Linking the voltammetric and spectroscopic results, a model was developed as shown in Fig. 1c, involving a structuring of water in the nanometer-sized reaction volume between desorbed SAM and Au electrode, by
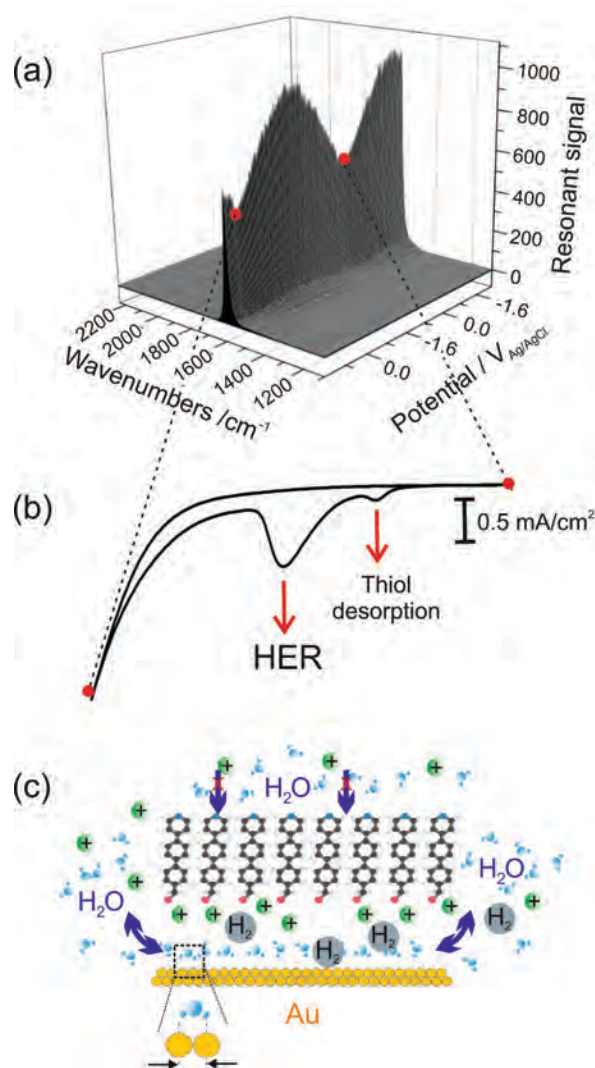
Fig. 1: *(a) SFG spectra of the pyridine ring vibration of PyPP1 on Au(111) during 1 1/2 CV cycles covering the reductive desorption potential of the SAM. No loss in order is observed at the desorption potential. (b) Cathodic peaks marking the reductive SAM desorption and associated rapid HER in a CV. (c) Schematic illustration of the proposed desorption mechanism. HER is catalyzed through optimum orientation of water molecules inside the gap between the desorbed crystalline thiolate film and the Au surface.*

the structurally extremely stable monolayer, leading to the observed catalysis of the HER [2].

In many cases, the actual use of SAMs bases on reactions occurring on the organic film. One specific case for such applications is the metallization of
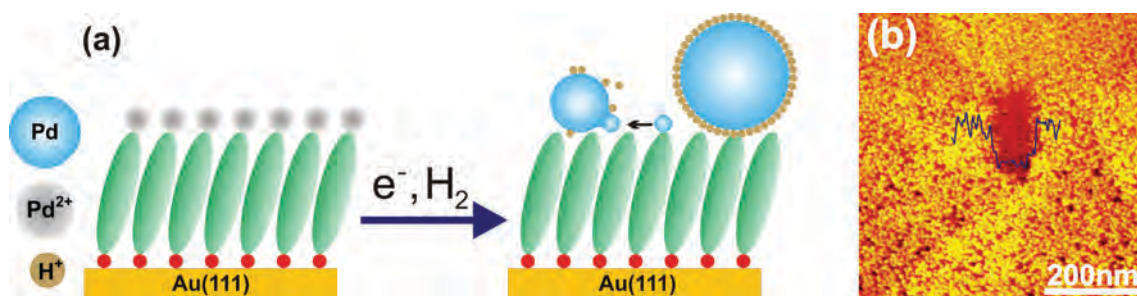
Fig. 2: *(a) Schematic illustration of metallization process through reduction by H_2 reduction of the SAM-coordinated Pd^{2+} ions. (b) Scanning tunnelling microscopy (STM) image of the deposited Pd adlayer with full coverage. The inter-action between SAM surface and Pd nanoclusters becomes weak after H_2 adsorption. This weak interaction enables a displacement of the nanoclusters with the STM tip as demonstrated in the center of the image after repetitive scans.*

SAM surfaces, needed for the development of metal/organic/metal junctions for organic electronics. However, the deposition of a top metallic layer onto a SAM is rather challenging.

For Pd deposition onto the well-characterized PyPP1 surfaces, we have demonstrated two strategies. The first one involves an electrochemical method [3], which has been the subject of several studies [4]. Further, a new electroless metallization method was introduced. This method bases on the reduction of the metal ions coordinated at the SAM surface by exposure to H_2 [5]. Its mechanism is schematically sketched in Fig. 2. The focus was on understanding the details of the deposition process. For instance, complexation kinetics of metal ions at the pyridine-functionalized SAM surface is discussed as a decisive process for understanding the coordination mechanism prior to the reduction step. Moreover, for the case of metallization by Pd, hydrogen adsorption on Pd during the reduction step has been studied. In agreement with theoretical work,

there is a strong interaction and modification of Pd adlayer through adsorbed hydrogen [6], for which experimental evidence is provided.

References

1   Muglali, M.I.; Bashir, A.; Terfort, A.; Rohwerder, M.: Phys. Chem. Chem. Phys. 13 (2011) 15530.

2.   Muglali, M.I.; Erbe, A.; Chen, Y.; Barth C.; Koelsch, P.; Rohwerder, M.: "Modulation of electrochemical hydrogen evolution rate by araliphatic thiol monolayers on gold", *submitted*.

3.   Baunach, T.; Ivanova, V.; Kolb, D.M.; Boyen, H.G.; Ziemann, P.; Buttner, M; Oelhafen, P.: Adv. Mater. 16 (2004) 2024.

4.   Muglali, M.I.; Liu, J.; Bashir, A.; Borissov, D.; Xu, M.; Wang, Y.; Wöll, C.; Rohwerder, M.: Phys. Chem. Chem. Phys. 14 (2012) 4703.

5.   Muglali, M.I.; Bashir, A.; Birkner, A.; Rohwerder, M.: J. Mater. Chem. 22 (2012) 14337.

6.   Kucera, J.; Gross, A.: Phys. Chem. Chem. Phys. 14 (2012) 2353.

Early Stages of High Temperature Corrosion in Steel Processing and Manufacturing

M. Auinger, A. Vogel, D. Vogel, M. Rohwerder

Department of Interface Chemistry and Surface Engineering

High temperature corrosion represents a vitally studied research field and fundamental understanding of the underlying mechanisms of material degradation is still a necessity to face upcoming challenges in modern energy politics.

Our current research activities in this field aim on a better understanding of the early stages of material degradation, especially on the changes of the surface conditions of the material under investigation. Many efforts have been undertaken to establish an accurate definition of process parameters to generate well-characterized exposures for a large variety of experimental possibilities.

Besides the unique combination at our institute, which makes this laboratory one of the flagship places in high temperature research worldwide, it amalgamates the benefits of rapid heating up to 30 °C s^{-1} (due to the use of an infrared-furnace), an oxygen impurity content of the used reaction gases below 3 ppm and a long-term stable dew-point (±0.2 °C). Thus the high temperature lab allows experiments covering a wide parameter field.

However, the *in situ* measurement of mass gain, especially during fast temperature cycles, which is a problem of significant practical importance, remained a problem that was experimentally unsolved. The reason for this is that due to fast changes of temperature in close vicinity to the sample surface, thermal drifts begin to dominate the thermobalance signal, making a clear scientific interpretation of the mass changes impossible. This problem is well known to the community for more than a couple of decades but a sound solution of such an issue has never been presented so far. Instead, trials to combine fast heating by infrared furnace with thermobalance were so far unsuccessful, i.e. results obtained with set-ups caused a lot of doubts and controversies and hence this combination is up to now only used for long-term exposures of several hundred hours.

In addition to coupling of IR-heating and thermobalance, it was therefore decided at MPIE to eliminate the content of inert gas – which often represents up to 95 % of the atmosphere – and to perform thermal exposures in a low pressure environment instead. By
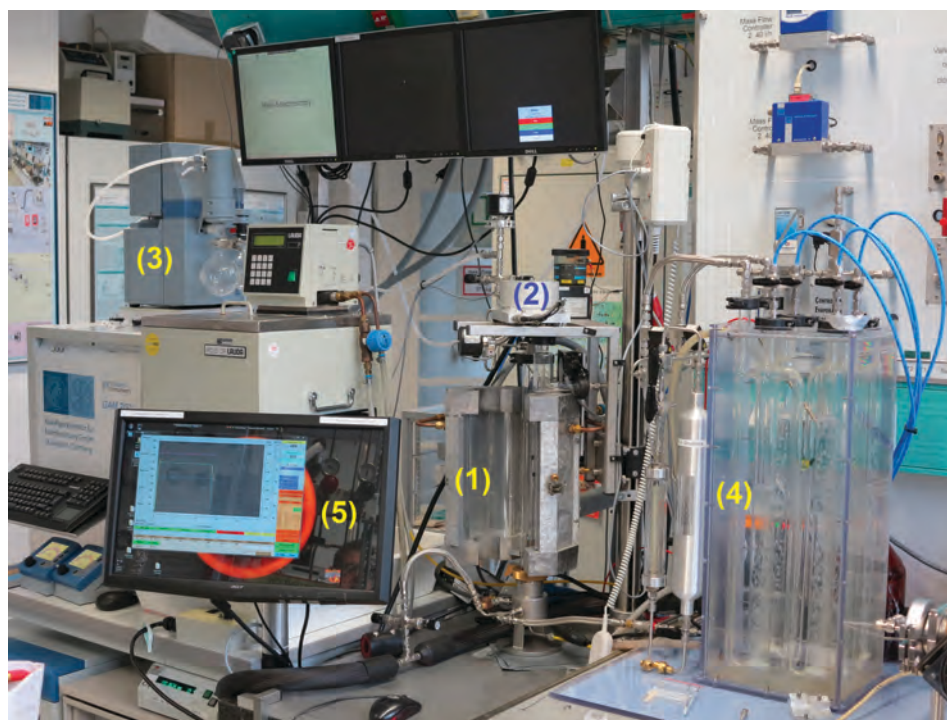
Fig. 1: *View of the novel thermobalance set-up for fast measurements showing an IR furnace (1) with thermobalance (2), a vacuum pump for adjusting the low-pressure conditions (3), gas humidification (4) and computer display for measurement results (5).*
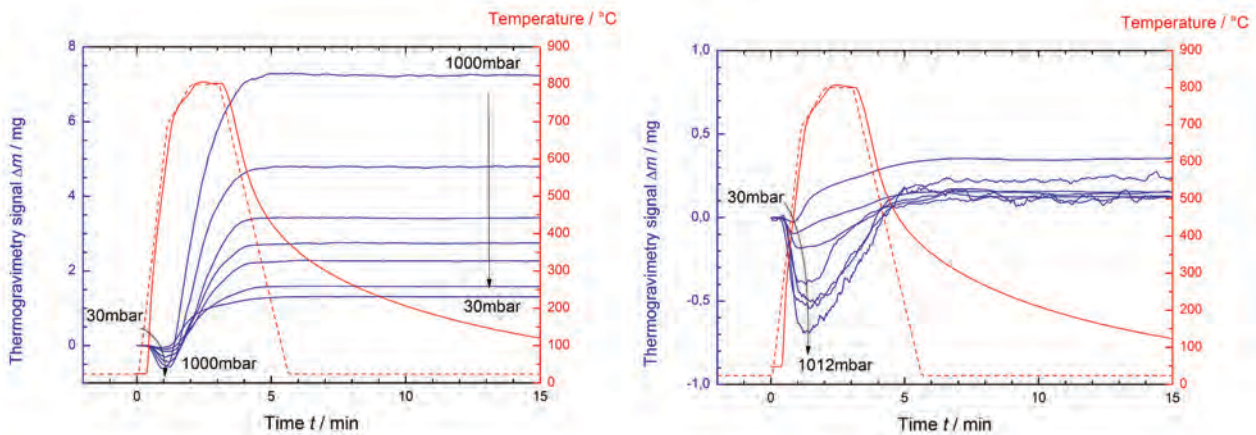
Fig. 2: *Pressure dependence of the thermogravimetric signal during a fast heating process in stationary argon atmosphere (left) and with continuous gas flow of 20 l h⁻¹ (right).*

this produce, we can still establish the same amounts of all reactive components and reduce the buoyancy effects by more than a factor of 10.

Initial tests with exposures of pure iron samples in an argon atmosphere, as illustrated in Fig. 2, prove the success of this technique. Whereas in both experiments a clear reduction of the initial drop in the recorded mass signal has been observed, the fluctuations in a steady gas flow could also be reduced by several orders of magnitude. This enables extremely accurate measurements of *in situ* mass changes down to 0.1 µg. Please note, that a low oxygen contamination in the argon gas causes a residual mass increase and that this can be clearly seen at 30 mbar (Fig. 2, left), whereas this is not possible at ambient gas pressures.

This method provides a unique contribution to elucidate the kinetics of oxidation in the early stages and closes the gap between experimental observations on a large time scale and other measurements of the initial stage behavior. Hence this technique represents an important scientific progress in the field and helps to shed light on early stage material degradation, both from a scientific point of view as well as for many industrial processes.

Biological D-Surface Structure: A Lesson from Nature on Photonic Crystals Design

X. Wu[1], A. Erbe[2], H. Fabritius[1], P. Ebbinghaus[2], M. Stratmann[2], D. Raabe[1]

[1] Department of Microstructure Physics and Metal Forming
[2] Department of Interface Chemistry and Surface Engineering

In the near future, photonic band gap materials are expected to play the same important role in photonics as semiconductors do in electronics [1]. Biological photonic crystals, particularly those of insects with their ability to display beautiful colours [2], provide models to learn the principles used by nature to open up photonic band gaps [3]. The small scales covering the beetle *Entimus imperialis* (Fig. 1a) are subdivided into irregularly shaped domains that mostly show striking colors, yet some appear transparent. Exposure of the photonic crystal using focussed ion beam (FIB) milling reveals that the photonic crystal is a bicontinuous cubic structure, where space is divided into two continuous subvolumes, namely, cuticular network and an air phase (Fig. 1b). The two phases are separated by a triply periodic intermaterial dividing surface (IMDS) generating a D-surface structure. Different observed colours correspond to different orientations of the same photonic crystal in each domain (Fig. 1b), making every scale act like a photonic polycrystal. Transparent domains contain the same structure as colored ones, but the air phase is substituted by a second solid phase (Fig. 1b). Transmission Fourier transform infrared (FTIR) spectra reveal the presence of two strong peaks at 1020 and 1091 cm^{-1} in transparent domains, which are typical for the most abundant four-fold coordinated silicon in SiO_2 [4] (Fig. 2). Together with the strong silicon peaks in energy-dispersive X-ray (EDX) spectra of transparent domains, this indicates that the beetle incorporates SiO_2 into its scales, which has never been observed before.

Using high-resolution scanning electron micrographs of all exposed domains, we morphometrically derived the parameters necessary to calculate a D-surface model that exactly reproduces the biological photonic
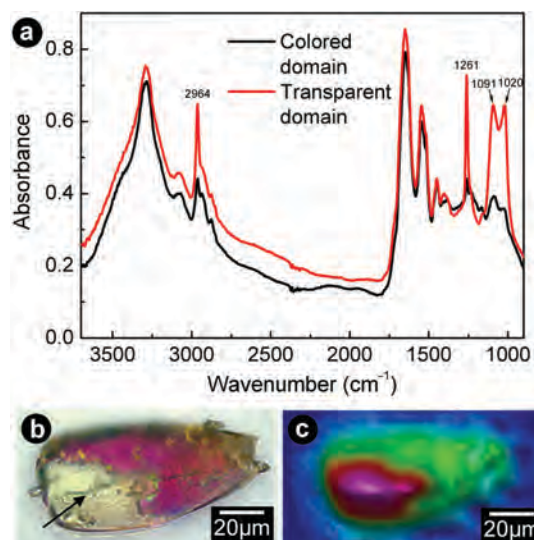
Fig. 2: *(a) Transmission FTIR spectra of the transparent (red line) and coloured (black line) domain. (b) Light micrograph of the analysed scale (arrow: transparent domain). (c) Spatial distribution of the integrated absorbance from transmitted light of the Si-O stretching mode spectral region (blue: weak integral absorbance, purple: strong integral absorbance).*

structure. The lattice constant was determined to be 407 (± 11) nm and the volume fraction of cuticular material amounted to 35% (± 1.5%) in all inspected domains. Adjusting visualizations of the D-surface model to match the appearance of the photonic crystal in the exposed domains (Fig. 1b) provided the Miller indices of the exposed lattice planes. The corresponding normal directions of the lattice planes oriented parallel to the scale surface (see Fig. 3a, next page) are close to the <111> direction in yellow domains, the <100> direction in green and light blue domains and the <110> direction in dark blue
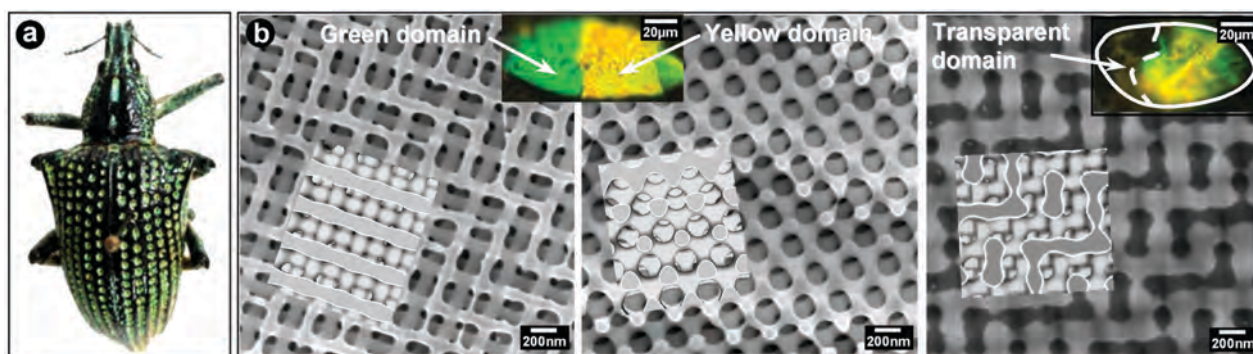
Fig. 1: *(a) The neotropic weevil Entimus imperialis (Coleoptera, Curculionidae). (b) Microstructure of the photonic crystal in coloured and transparent domains. The electron micrographs show the photonic crystal exposed parallel to the scale surface, the greyscale inserts corresponding visualizations of the D-surface model. The insert light micrographs show the exact probed locations on the respective scales.*

Fig. 3: *(a) Photonic band diagram for coloured and transparent domains. The probed locations (light micrographs) and the colour range of the band gaps (arrows) for the corresponding directions are shown as inserts. (b) Band gap width as a function of varying volume fractions of cuticular material. For three differently coloured domains, the band gaps obtain their widest frequency ranges at a volume fraction close to 35% (dashed line) as observed in the beetle. For transparent domains with low refractive index contrast, the band gaps are very narrow (circle).*
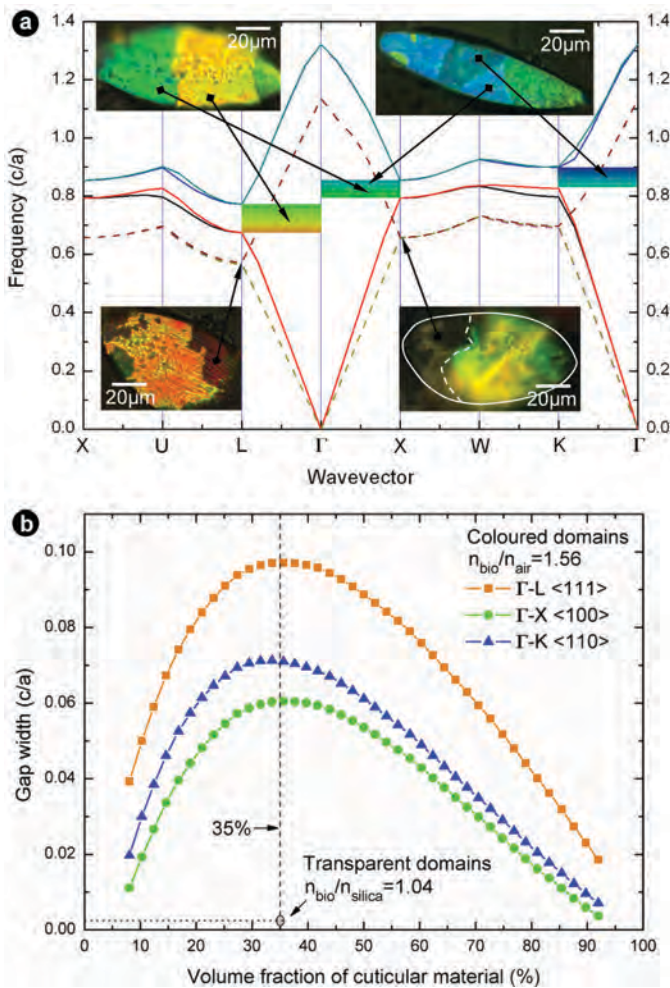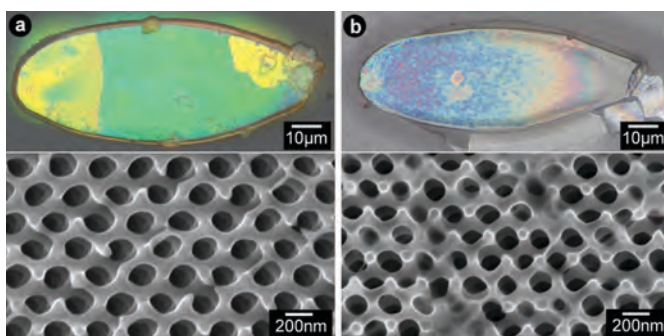

Fig. 4: *Comparision of appearance and microstructure of (a) a native scale and (b) its silica replica.*

domains. To validate the structural analysis of the photonic crystal in coloured and transparent domains of scales and compare their optical properties, we used the adjusted D-surface structure model to calculate the photonic band structure [5]. As refractive index of the cuticular network, we assumed 1.56 and we used 1.5 for the SiO_2 phase. The resulting photonic band diagram (Fig. 3a) shows partial band gaps in different directions. For coloured

domains, the wavelength range of band gaps are 527-603 nm for Γ-L <111> (yellow domain), 476-513 nm for Γ-X <100> (green and light blue domains) and 453-492 nm for Γ-K <110> (dark blue domain) (see Fig. 3a). The observed colours in differently oriented domains and the wavelength ranges of the band gaps in the corresponding directions are in good agreement (Fig. 3a). By varying the volume fraction of the cuticular material from about 8% to 92%, the band gaps calculated for all investigated coloured domains obtain their widest frequency ranges when the volume fraction is close to 35 %, the value we determined for the beetle (Fig. 3b). Optically, a band gap covering a wider frequency range not only means more hues included, but also implies that a larger fraction of the incident white light is reflected. Thus, the scales show a stronger reflection and appear more brilliant.

In contrast, the combination of the SiO_2 phase and the cuticular phase in transparent domains shows only very narrow partial photonic band gaps due to the very small refractive index contrast between them (Fig. 3b). These narrow gaps only allow a very small fraction of the incident light to be reflected while the rest is transmitting through the scale. This weak reflection is sensitive to scattering. As a result, the domain appears transparent and dull to the eye.

Modification of the photonic band gap width, and thus the optical appearance, by replacing the air phase of a 3D photonic crystal with a second solid phase was observed for the first time in a beetle and offers great opportunities for the fabrication of tuneable biomimetic photonic crystals.

In collaboration with the group of Prof. Zollfrank (TU München), this biological photonic crystal has been biomimetically transferred into identical silica replicas with tuneable structural parameters [6] (Fig. 4).

References

1. Joannopoulos, J.D.; Johnson, S.G.; Winn, J.N.; Meade, R.D.: "Photonic Crystals: Molding the Flow of Light", Princeton University Press, Princeton, 2008.

2. Kinoshita, S.: "Structural Colors in the Realm of Nature", Word Scientific Publishing, Singapore, 2008.

3. Vukusic, P.; Sambles, J. R.: Nature 424 (2003) 852.

4. Farmer, V.C.: "The Infrared Spectra of Minerals", Mineralogical Society Monograph 4, Mineralogical Society, London, 1974.

5. Johnson, S. G.; Joannopoulos, J. D.: Opt. Express 8 (2001) 173.

6. Van Opdenbosch, D.; Johannes, M.; Wu, X.; Fabritius, H; Zollfrank, C.: J. Photonics 10 (2012) 516.

SELECTED HIGHLIGHTS

Integrated Experimental-Numerical Analysis of Stress and Strain Partitioning in Multi-Phase Alloys

C. Tasan, D. Yan, S. Zaefferer, E. Demir, D. Raabe,
M. Diehl, F. Roters, P. Eisenlohr, B. Svendsen, R. A. Lebensohn

Department of Microstructure Physics and Alloy Design

Strain and stress partitioning is crucial in the behavior of multi-phase advanced high strength alloys, while its analysis is not possible using traditional experimental tools or by stand-alone numerical homogenization simulations. We therefore develop a novel integrated experimental-numerical methodology using experimentally obtained local deformation information to calibrate constitutive models for full-field crystal plasticity simulations.

The integrated methodology is as follows: Starting from large-area electron backscatter diffraction (EBSD) measurements conducted on a dual phase steel tensile test sample (Fig. 1a), representative microstructural regions are selected (Fig. 1b). The sample is imaged at increasing levels of strain (Fig. 1c) and local strains are measured using digital image correlation (DIC) (Fig. 1d). As final experimental step, orientation changes are measured using EBSD[1] (Fig. 1e). The simulations also start from

[1] Note that both EBSD mappings can also be used to evaluate geometrically necessary dislocation densities from the calculation of the full dislocation density tensor [1].

the EBSD analysis of the undeformed microstructure, which is used to create the model (Fig. 1b). The initial crystallographic information of each point is taken directly from the EBSD measurement, and the distinction of martensite and ferrite is carried out based on the grain average image quality. The inset in Fig. 1f shows the resulting phase distribution. Both phases, martensite and ferrite, are modeled using a phenomenological crystal plasticity model [2] fitted to experimental stress-strain curves. The polycrystal stress-strain-curves for both phases are shown in Fig. 1f. The simulation is carried out using a spectral solver as described in [3] that is particularly suited for high mechanical phase contrast composites. These solvers make use of Fast Fourier Transforms (FFT) and are much more efficient than the FEM when simulating so called Representative Volume Elements. They, therefore, offer an unmatched resolution for direct full-field crystal plasticity simulations.

The experimental results presented in Fig. 2a (next page) reveal that: (i) the ferrite regions carry
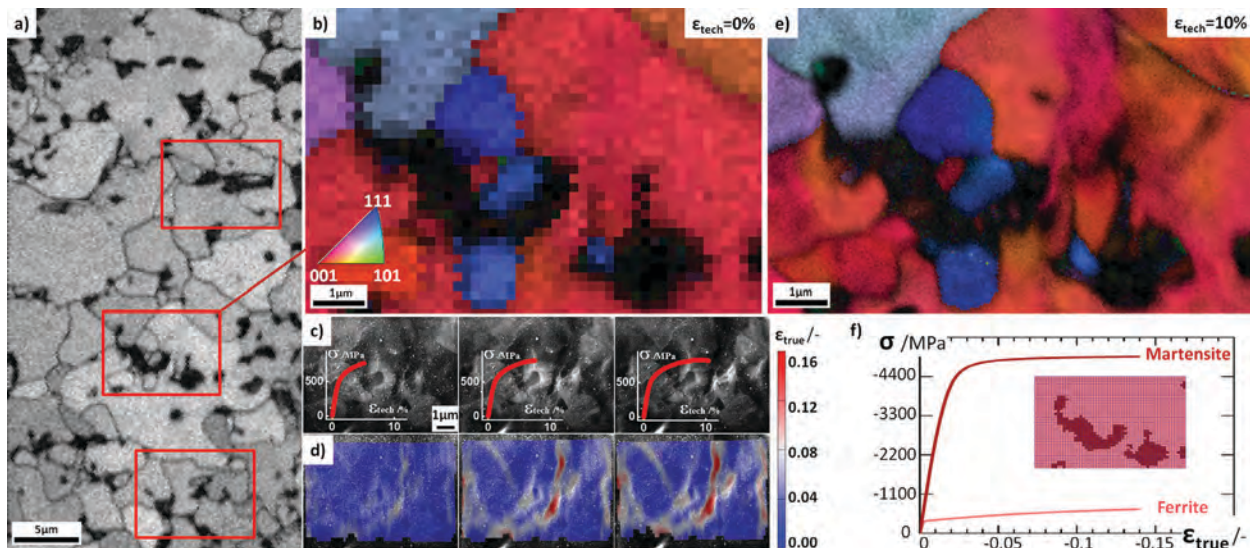
Fig. 1: *Experimental-Numerical Methodology: (a) Image quality (IQ) map obtained from a large area scan EBSD measurement, (b) Higher magnification IQ map of the selected region, with an inverse pole figure (IPF) overlay, (c) SE images, obtained during deformation in the horizontal direction, of the region shown in b (now covered by colloidal silica particles for DIC), with an overlay of the global stress and strain curve at the point of image acquisition, (d) local strain in the loading direction obtained from DIC analysis of the images shown in c, (e) IQ map and IPF overlay obtained from the area shown in b after deformation (f) Phase properties used in the numerical simulations, and an inset image showing the micromechanical model structure created from the EBSD measurement shown in b that serves as input to the full-field simulations.*
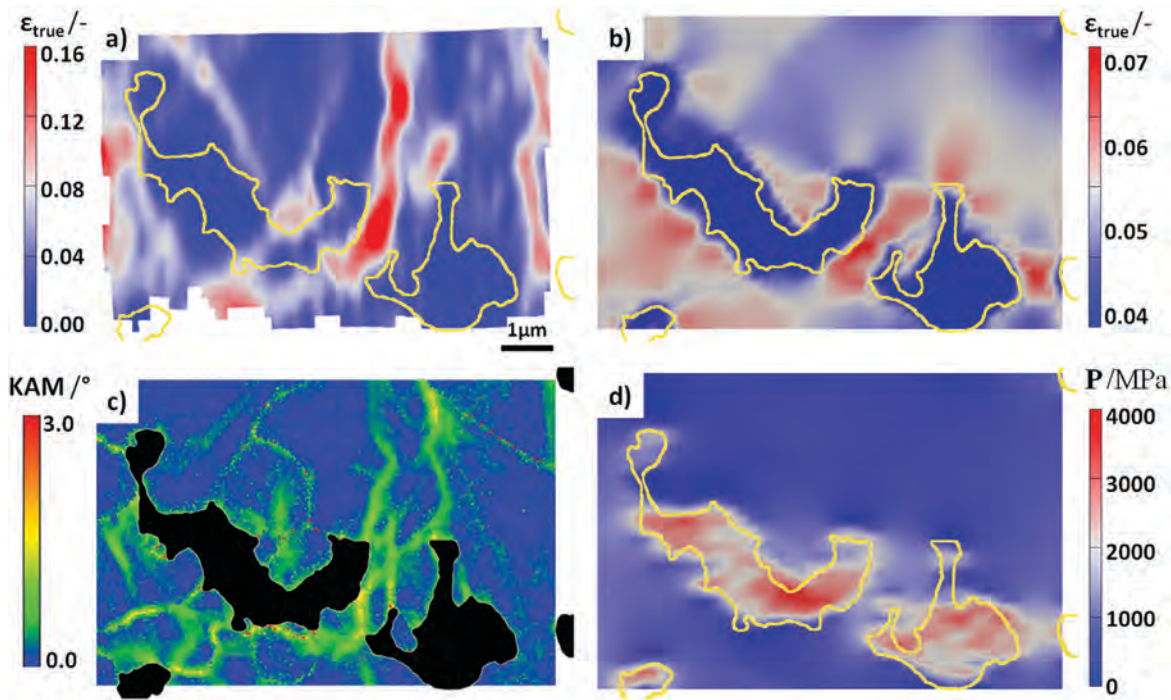
Fig. 2: *Experimental-numerical results of strain and stress distribution in the region shown in Fig 1b. Martensite islands are surrounded by a yellow line. (All strain and stress quantities are in the loading direction):* **(a)** *Local strain map obtained from DIC analysis,* **(b)** *Local strain map obtained from numerical simulation,* **(c)** *kernel average misorientation map obtained from EBSD data,* **(d)** *Local stress map obtained from numerical simulation.*

most of the strain while the martensite remains nearly undeformed; (ii) the strain distribution in the ferrite is very inhomogeneous. This micromechanical heterogeneity is confirmed by the kernel average misorientation map presented in Fig. 2c, showing a similar distribution for the local misorientation. The locations of the high-strain bands with respect to the martensite islands suggest that the martensite phase dispersion and morphology governs strain localization. More specifically, strain localization effects occur in regions where bulky martensite islands are separated by a narrow gap of ferrite in-between and where irregularities in martensite geometry cause local stress peaks.

The strain distributions obtained from the full-field crystal plasticity simulations (Fig. 2b) show good qualitative agreement with those obtained from experiments (mind the different scales in Fig. 2a and b) reproducing the majority of the deformation bands. Quantitatively however, the simulations reveal less pronounced strain partitioning, suggesting that the single phase properties used are not exactly matching those of the real constituents.

The stress distribution obtained from the simulations (Fig. 2d) shows that most of the stress in the material is carried by the martensite phase. More importantly, the detrimental effect of irregularities in the martensite morphology is also underlined: Highest stresses

occur in the narrow regions of the martensite islands. This correlates well with earlier observations showing that martensite sphericity plays an important role for its plastic deformation limits [4].

To conclude, a novel joint experimental-numerical micromechanical methodology is being developed that allows analyses of strain and stress partitioning in complex multi-phase materials. The preliminary results show a promising correlation between the experiments and corresponding full-field crystal plasticity FFT simulations. The results demonstrate the importance of martensite dispersion and sphericity in dual phase steels for the integral mechanical behavior. Current emphasis is placed on improving the quality of the simulations further by feeding in more realistic phase properties for ferrite and martensite.

References

1. Demir, E.; Raabe, D.; Zaafarani, N.; Zaefferer, S: Acta Mater. 57 (2009) 559.

2. Kalidindi, S.R.; Bronkhorst, C.A.; Anand, L.: J. Mech. Phys. Solids 40 (1992) 537.

3. Eisenlohr, P.; Diehl, M.; Lebensohn, R.A.; Roters, F.: Int. J. Plasticity (2012) DOI 10.1016/j.ijplas.2012.09.012.

4. Calcagnotto, M.; Adachi, Y.; Ponge, D.; Raabe, D.: Acta Mater. 59 (2011) 658.

Paramagnetic Phonons and Free Energies from *ab initio*:
A First-Principles Prediction of the Anti-Invar Effect in fcc Fe

F. Körmann, B. Grabowski, B. Dutta, T. Hickel, J. Neugebauer

Department of Computational Materials Design

Dynamic processes on the atomic scale determine the kinetics and thermodynamics of steels. Such processes are behind many technologically relevant mechanisms, but are often only poorly understood. An example is the anti-Invar effect in fcc Fe, i.e., a large and constant expansion coefficient for a wide temperature range. For theoretically describing the free energy of such mechanisms, the simulation of the dynamics is critical. These calculations require the computation of the forces acting on individual atoms. In the case of magnetic materials, however, the reduction of magnetic order makes current *ab initio* approaches often not suited for describing forces at finite magnetic temperatures. Using ordered magnetic states instead is for the chosen example fcc Fe not an option, since they yield dynamic instabilities.

Within in the last few years, several approaches based on dynamical mean field theory, non-collinear spin-spiral calculations, or spin MD were proposed to overcome this limitation. They have in common that they are not only computationally expensive, but also inhibit a conceptually increased level of complexity. As a consequence the prediction of thermodynamic properties of paramagnetic materials at finite

temperatures such as linear expansion coefficients or bulk modulus has not been achieved so far.

We recently introduced a scheme to compute atomic forces at finite magnetic temperatures, for which we developed a spin-space averaging (SSA) procedure [1]. In the proposed scheme the SSA forces are obtained by coarse-graining the magnetic configuration space. For example, the atomic forces in the high-temperature paramagnetic state, where the local magnetic moments are randomly distributed over the lattice, are obtained by statistical averaging over a sufficiently large set of magnetic structures, as sketched in Fig. 1. In practice the magnetic configurations are constructed using the concept of special quasi-random structures as obtained from the ATAT package.[1] The computational efficiency can be further improved by employing in addition the underlying crystal symmetries [1].

From the effective SSA forces the phonon spectra can straightforwardly be deduced. In Fig. 2 we demonstrate that the theoretical results of our new

---

[1] To simplify the modeling of the PM state we consider here collinearly disordered magnetic moments only. The proposed scheme itself is, however, very general and would, in principle, allow the incorporation of non-collinear structures.

Fig. 1: *Sketch of the SSA procedure. The effective forces at finite magnetic temperatures are obtained from a set of disordered magnetic configurations.*
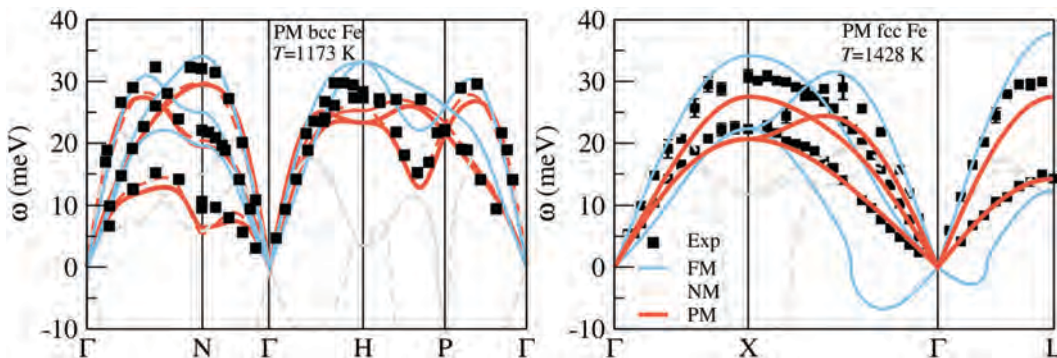

Fig. 2: *Phonon spectra of bcc and fcc Fe above the magnetic ordering temperatures. Computing the spectra with the SSA scheme to describe paramagnetism (PM) provides excellent agreement with experimental data in contrast to ferro- (FM) or non-magnetic (NM) calculations.*
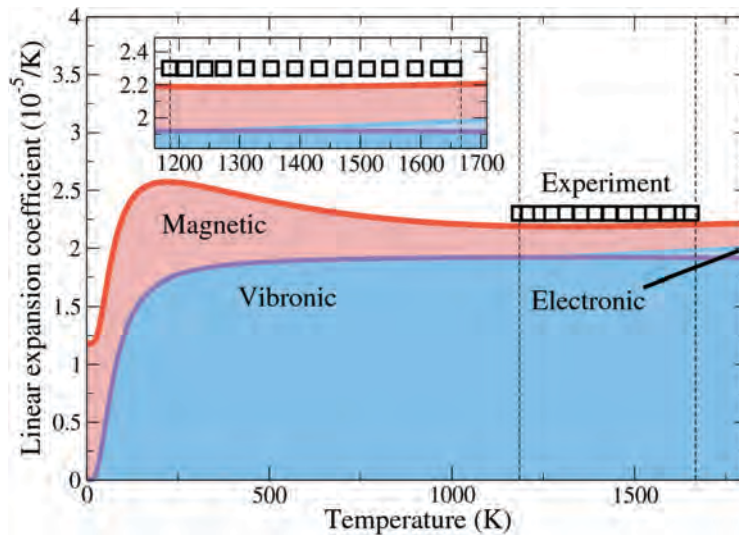
Fig. 3: *Comparison of the theoretical linear expansion coefficient for fcc Fe (red line) with experiment (black symbols [4]). The dashed vertical lines indicate the stability regime of fcc Fe. The inset provides a zoom-in into the fcc stability regime.*

scheme for bcc and fcc Fe agree very well with experimental data in the paramagnetic (PM) state. Even particularities such as the strong phonon softening for bcc Fe around the N-point (reflecting the infamous strong decrease in the C' and C_{11} elastic constants at higher temperatures) are reproduced. Furthermore, the dynamical instability of non-magnetic bcc Fe at 1173 K is lost in the PM state. For the present discussion more decisive is the fact that also in case of fcc Fe the magnetic disorder is sufficient to remove the dynamic instabilities, being present in ferro-/nonmagnetic calculations.

We can make further use of the clear advantages of the SSA scheme that it can be easily extended to compute vibronic free energy contributions with already existing statistical concepts such as, e.g., the quasi-harmonic approximation. Combining the SSA scheme for the vibronic entropy with explicit electronic and magnetic contributions [2] enables us to compute a completely *ab initio* derived free energy surface for fcc Fe. Only in this way is it now possible, to determine the linear expansion coefficient for fcc Fe. The comparison with available experimental data in Fig. 3 yields an excellent agreement. Within the new scheme it is even possible to reproduce and understand the (long debated) anti-Invar effect in fcc

Fe [3]. As can be seen from Fig. 3 the source of the high and constant expansion coefficient is mainly due to vibronic contributions revealing the significant impact of the volume dependence of paramagnetic lattice vibrations/phonons.

In summary, we have extended our previous methods [2] to account for the delicate interplay between atomic and magnetic degrees of freedom at high temperatures. The developed SSA procedure provides not only an excellent scheme to compute atomic forces at finite magnetic temperatures, but allows further, in combination with statistical concepts, the computation of free energy surfaces in the paramagnetic regime.

References

1. Körmann, F.; Dick, A.; Grabowski, B.; Hickel, T.; Neugebauer, J.: Phys. Rev. B 85 (2012) 125104.

2. Körmann, F.; Dick, A.; Hickel, T.; Neugebauer, J.: Phys. Rev. B 83 (2011) 165114.

3. Körmann, F.; Grabowski, B.; Dutta, B.; Hickel, T.; Neugebauer, J.: First-principles prediction of the anti-Invar effect in fcc Fe, *in preparation for* Phys. Rev. B.

4. Acet, M.; Zähres, H.; Wassermann, E.F.; Pepperhoff, W.: Phys. Rev. B 49 (1994) 6012.

Dual Scale Modeling of Phase Equilibria

D. Korbmacher[1], R. Spatschek[1], J. von Pezold[1], C. Hüter[1],
J. Neugebauer[1], S. Brinckmann[2]

[1] Department of Computational Materials Design
[2] ICAMS, Ruhr-Universität-Bochum

The basis for a theory guided design of new steels and other novel materials with superior properties is the development of a multiscale simulation chain, which transfers information from one lengthscale to the next. This is absolutely necessary also for understanding phenomena like hydrogen embrittlement [1] and other material failure mechanisms, as well as the finding of new battery materials [2]. It comprises the scale-bridging modeling of phase equilibria and transitions in complex materials, ranging from macroscopic dimensions down to the nanoscale. For this, an efficient and accurate matching between the atomistic simulations and formal thermodynamic and continuum concepts is critical. We have therefore studied approaches that seamlessly connect the atomistic and continuum scale, illustrated for the Ni−H system. Our approach provides important fundamental insights into the theory of phase equilibria in coherent solid-state systems such as nanodispersion strengthened or electrical steels, as it elucidates quantitatively the role of different energetic and entropic contributions.

The starting point of our study is the determination of the equilibrium spatial distribution of the interstitial H atoms in the metallic matrix, employing Monte-Carlo simulations and molecular statics. Depending on the H chemical potential dilute or condensed H distributions are obtained. The condensed hydride precipitates remain coherent and adopt characteristic shapes depending on the bulk H concentration, as shown in Fig. 1. The chemical potential of the hydrogen atoms, μ_H, as a function of the average concentration deviates significantly from its expected functional form based on the common tangent or Maxwell construction.

Our starting point for transferring this complex atomic scale behavior to the continuum level is the free energy for the single phase material, $F = F_{el} + \mu_0 N_H + F_c + F_{H-H}$, with the number of hydrogen atoms N_H and the elastic free energy F_{el}, the configurational free energy F_c and the hydrogen-hydrogen interaction F_{H-H}. μ_0 is the solvation energy needed to insert an isolated hydrogen atom into the (empty) matrix. The hydrogen-hydrogen interaction reflects the lattice mediated attraction between hydrogen atoms, which are dissolved in the matrix. The configurational contribution stems from the different combinatorial possibilities to occupy the octahedral sites with hydrogen. Together, they constitute the typical "van-der-Waals loop" (green curve in Fig. 1).

Phase coexistence on this level is described by Maxwell's equal area rule, which states that phase separation sets in at the intersection points of a horizontal line with the S-shaped van der Waals loop, cutting it into two equal areas above and below this Maxwell line (blue line).Obviously, at this level
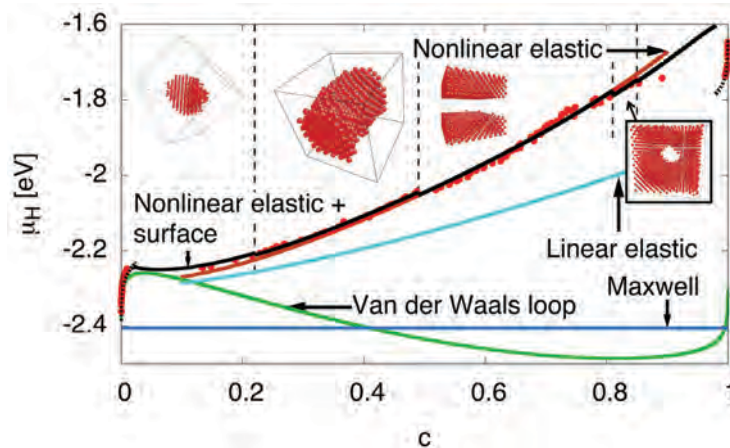
Fig. 1: *The chemical potential of hydrogen at T = 300 K. The red dots are the data from the Monte Carlo simulations, the green curve is the calculated van der Waals curve. Phase equilibrium without elastic and interfacial effects represented by the blue horizontal Maxwell line. Modifications due to cubic linear elasticity are given by the cyan curve. The chemical potential including nonlinear elastic effects (brown) is very close to the atomistic data, and together with interfacial effects (black) the agreement is even more convincing. The insets show the different concentration dependent patterns, the vertical dashed lines separating the concentration regimes.*
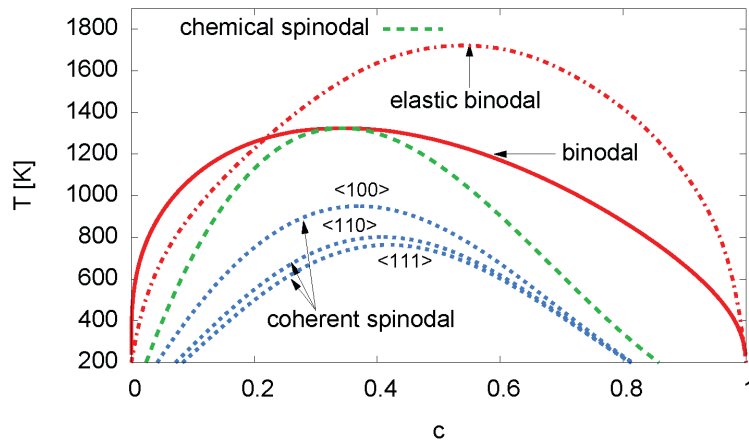
Fig. 2: *Phase diagram and spinodals of the Ni-H systems, based on parameters extracted from Monte Carlo simulations. The concentration is 1 if all octahedral sites are filled, i.e. equal number of Ni and H atoms. The solid red line is the binodal without consideration of elastic effects, whereas the dash-dotted line is the same with elastic effects for fixed volume. The chemical spinodal (green) ignores elastic effects and touches the binodal at the critical point, whereas the coherent spinodals (blue) take into account deformations for density variations in the given directions. Spinodal decomposition is possible below the curves.*

the agreement with the fixed volume atomistic data is not good at all. The large deviations between the atomistic data and the continuum model clearly indicate that elastic and interface effects are critical and cannot be neglected. The pure nickel and the hydride exhibit a substantial lattice mismatch, leading to the cyan curve shown in Fig. 1. Since we still observe a significant discrepancy to the Monte Carlo data, we therefore conclude that the consideration of linear elasticity is not sufficient to explain the slope of the chemical potential in the two phase region.

The reason for this discrepancy is the appearance of large compressive stresses for higher hydrogen concentrations implying that nonlinear elastic effects have to be taken into account. With them the continuum chemical potential shows now a much more satisfactory agreement with the Monte Carlo data (see the brown line in Fig. 1).

In a final step we take into account interfacial effects. Although they give only a small contribution, they determine the shape of the precipitates. For low concentrations we expect spherical hydride inclusions, followed by tubular and slab-like precipitates. For high concentrations, when instead the nickel phase nucleates inside the hydride, the arrangement is similar. In our atomistic calculations we indeed find all these structures in the correct ordering (see Fig. 1).

Including all energy contributions we are able to successfully transfer the atomistic onto the continuum scale. This allows us e.g. to predict the entire bulk phase diagram without and with elastic effects, see Fig. 2. We see the tremendous influence the elastic effects have on phase stability, with an enlargement of the two-phase region towards higher temperatures and the hydrogen rich side. This unusual reduction

in solubility - one would intuitively expect the suppression of phase separation since coherency stresses are energetically unfavorable - is due to deviations from Vegard's law.

Finally, our approach allows to predict the onset of spinodal decomposition, going beyond the purely static equilibrium concepts considered so far. In the spinodal regime the homogeneous mixture is unstable, whereas in the remaining two-phase region phase separation is initiated by nucleation processes, requiring an activation energy. Spinodal decomposition is suppressed since density fluctuations provoke elastic stresses, leading to the coherent spinodal regime, as shown in Fig. 2 for density variations in different lattice directions.

Altogether, the determination of phase diagrams nicely demonstrates the opportunities arising from the transfer of atomistic data to the mesoscale: We point out that the results shown in Fig. 2 are practically impossible to obtain accurately using atomistic simulations only, as this requires the modeling of very large systems and the clear distinction from nucleation events for the spinodal decomposition. The resulting description can then also directly be used in mesoscale simulations models like phase field.

References

1. von Pezold, J.; Lymperakis, L.; Neugebauer, J.: Acta Mater. 59 (2011) 2969.

2. Haftbaradaran, H.; Song, J.; Curtin, W.A.; Gao, H.: J. Power Sources 196 (2011) 361.

3. Korbmacher, D.; Spatschek, R.; von Pezold, J.; Hüter, C.; Neugebauer, J.; Brinckmann, S.: "Dual scale modeling of phase equilibria: the role of nonlinear elastic effects", Phys. Rev. B Rapid Comm., *submitted.*

Extending *ab initio* Simulations of Point Defects up to the Melting Temperature

A. Glensk, B. Grabowski, T. Hickel, J. Neugebauer

Department of Computational Materials Design

Many technologically relevant processes are ultimately connected to point defects. Prominent examples are thermodynamic phase stabilities governing phase transformations or diffusion processes determining the concentration profile and segregation kinetics. Point defects have also a strong impact on mechanical strength and ductility of structural materials by acting as pinning centers for dislocations or by enabling dislocation climb.

The natural quantity to characterize point defects is their Gibbs energy of formation, $G^f(T) = H^f(T) - TS^f(T)$. An experimental determination of the temperature dependence faces great difficulties as only a small high-temperature window is directly accessible (see Figs. 1 and 2). Differential dilatometry (DD), on the one hand, yields in the case of Cu from the melting point of 1360 K down to about 1200 K a smooth curve of data points. Below 1200 K, however, the scatter in the data indicates that the statistics is too poor to sufficiently resolve the vacancy related differences between an increase in the macroscopic length and in the lattice constant. Positron annihilation spectroscopy (PAS), on the other hand, allows one to assess a slightly lower concentration window, but is unable to resolve concentrations above 10^{-4} as saturation effects set in prohibiting accurate measurements.

For describing $G^f(T)$ it is therefore common practice to assume simplifying (i.e., Arrhenius like) temperature dependencies, $G^f = H^f - TS^f$, with constant H^f and S^f fitted to available high temperature data. However, these results show often only poor agreement with *ab initio* formation enthalpies of H^f, determined at T = 0 K, even for 'simple' elements like Cu or Al. As an additional complication, already small scatter in the high-temperature experimental data yields in the extrapolations over wide temperature ranges large uncertainties in the extrapolated H^f at $T = 0$ K. Finally, G^f seems to show for DD and PAS qualitatively different temperature dependencies. Two scenarios have been discussed in the literature to explain these inconsistencies. Scenario (A) assumes that G^f is non-linear with a temperature dependent $H^f(T)$ and $S^f(T)$. Alternatively, the change in concentration is explained in scenario (B) by a
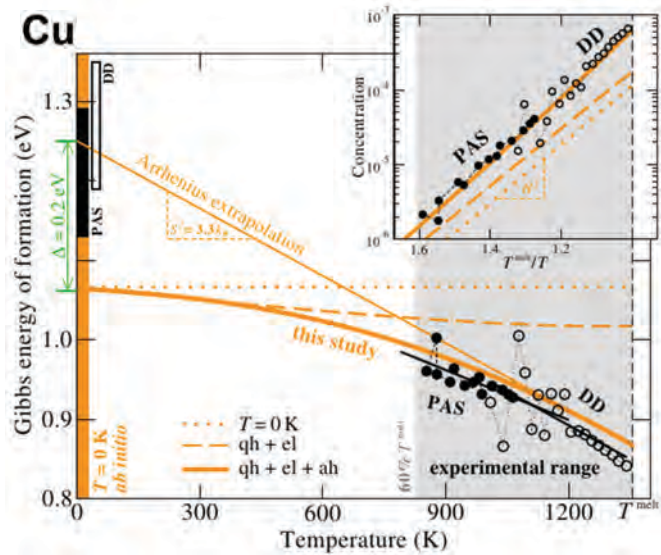
Fig. 1: *Experimental (black symbols, lines, and stripes) and ab initio (orange lines) vacancy formation energies in bulk-Cu. Experiments (PAS=positron annihilation spectroscopy [6], DD=differential dilatometry [7]) are limited to temperatures close to the melting point (gray shaded region). Extrapolations of DD and PAS data introduce uncertainties (filled and empty black stripes in upper left corner) hampering comparison with T = 0 K ab initio data. The present DFT study closes the gap between experiment and theory (bold solid orange line).*

Fig. 2: *Possibilities and limitations of the two most popular DFT exchange-correlation functionals, LDA and GGA. The example shows the properties of monovacancies in Al. While showing an almost constant shift (originating from differences in the T = 0 K results), the clearly non-linear temperature dependence is well described by both functionals. Experimental data are from Refs. [6] (●), [8] (□), and [6] (○).*

superposition of mono- and divacancies, the latter dominating the slope of G^f at high temperatures [1].

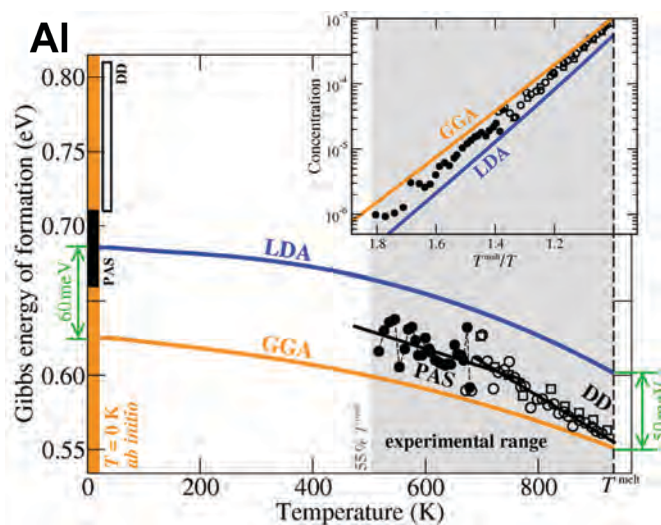In order to resolve this long standing debate, we have performed highly accurate temperature-dependent DFT simulations of mono- and divacancies in Al and Cu [2]. We apply our previously developed techniques to include a complete description of electronic and ionic finite temperature excitation mechanisms as well as their thermodynamic coupling. The often used simplifying assumption of non-interacting phonons is dropped: Phonon-phonon interactions are considered accurately yet efficiently by lattice dynamics employing our recently developed hierarchical coarse graining scheme. This scheme achieves a reduction from 10^7 configurations usually necessary to sample the configuration space to only 10^2 configurations at full *ab initio* accuracy [3].

Based on our calculations we can rule out that divacancies are the reason for the non-Arrhenius behaviour for Al and Cu as assumed in literature (scenario B). At T = 0 K, we find the divacancy to have only a small binding energy (~80 meV in the case of Cu). The small energy indicates that the divacancy dissociates into two isolated vacancies for high temperatures and characteristic concentrations. An even stronger argument to discard the divacancy is related to the slope of G^f at finite temperatures. In order to explain the difference between DD and PAS within the mono-divacancy scenario (B), a significantly larger S^f for divacancies has to be assumed. Our results disprove this assumption: The *ab initio* computed entropy of formation is very similar in magnitude for di- and monovacancies. As a consequence, the divacancy concentration is even at the melting temperature negligible (10^{-7}) for both Al and Cu with respect to the monovacancy concentration (10^{-3}).

We can therefore conclude that deviations from a linear (Arrhenius) behaviour of the monovacancy G^f are responsible for the experimental observations. Being able to compute all free energy contributions allows us to systematically check the agreement with the various levels of theory. The dotted line in Fig. 1 shows the T = 0 K *ab initio* value which, as mentioned earlier, does not agree with the value extrapolated from experiment. The dashed line additionally includes the influence of non-interacting but volume dependent phonons (quasiharmonic approximation) and it is clear that a significant discrepancy with experiment remains. The vanishing slope at high temperatures resembles vanishing entropy (S ~ 0.0 k_B). Electronic entropy effects are found to be negligible at this scale. Adding finally explicit

anharmonic contributions (bold solid orange line) an excellent agreement with experiment is found. In particular, the curvature of the Gibbs formation energy accurately captures the deviating slopes of PAS and DD data.

Having this formalism we systematically checked the performance of the various exchange-correlation (xc) functionals. Fig. 2 shows the results of such calculations for Al vacancies and the two most commonly employed functionals, the local-density (LDA) and the generalized gradient approximation (GGA). The two functionals bound the experimental data, a behaviour we consistently find also for other elements [4]. We further observe that the *ab initio* temperature dependence follows the experimental results remarkably close. Both observations further substantiate our earlier findings [5] that (i) DFT based thermodynamic properties are mainly limited by the accuracy at T = 0 K and that (ii) the comparison of several xc-functionals can provide a confidence interval for the accuracy of the *ab initio* results.

In conclusion, the almost universally applied assumption of temperature independent H^f and S^f (linear Arrhenius behavior) is not justified when extrapolating high-temperature data to T = 0 K. Using the correct temperature dependence, which was unknown before this study, we find corrections in the order of a few tenth of an eV for the vacancy formation energies and an order of magnitude for the entropies. The new formalism allows us to compute finite temperature point defect energies with hitherto unprecedented accuracy – being important for realistic applications as well as for improving the predictive power of DFT calculations, where these energies are often used as benchmarks.

References

1. Neumann, G.; Toelle, V.; Tuijn, C.: Physica B 271 (1999) 1533.

2. Glensk, A.; Grabowski, B.; Hickel, T.; Neugebauer, J.: Phys. Rev. Lett., *submitted*.

3. Grabowski, B.; Ismer, L.; Hickel, T.; Neugebauer, J.: Phys. Rev. B 79 (2009) 134106.

4. Nazarov, R.; Hickel, T.; Neugebauer, J.: Phys. Rev. B 85 (2012) 144118.

5. Grabowski, B.; Hickel, T.; Neugebauer, J.: Phys. Rev. B 76 (2007) 024309.

6. Hehenkamp, T.: J. Phys. Chem. Solids 55 (1994) 907.

7. Kluin, J.E.; Hehenkamp, T.: Phys. Rev. B 44 (1991) 11597.

8. Simmons, R.O.; Balluffi, R.W.: Phys. Rev. 117 (1960) 52.

Strong and Weak Magnetic Coupling in Chromium

F. Körmann[1], B. Grabowski[1], M. Palumbo[2], S.G. Fries[2], T. Hickel[1], J. Neugebauer[1]

[1] Department of Computational Materials Design, [2] ICAMS, Ruhr-Universität Bochum

Chromium is a key material in many practical applications and, in particular, a decisive ingredient for stainless steels. At low temperatures bcc Cr displays antiferromagnetic order in form of an incommensurate spin density wave (SDW), which disappears at a critical (Néel) temperature of T_N = 311 K. While this temperature regime is well understood today, several observed anomalies in the high-temperature thermodynamic properties of Cr leave many questions open [1]. We have collected results of various measurements from the last thirty years (literature research at ICAMS), which revealed peculiarities in the expansion, its coefficient, heat capacity and elastic moduli well above the Néel temperature (black symbols in Fig. 1). One example is the enormous increase in the linear expansion coefficient (Fig. 1b). It even strongly exceeds the ones of Mo and W, which are themselves known to have high coefficients due to anharmonic contributions. In the case of Cr, it was speculated that again anharmonic or alternatively magnetic contributions are responsible for the strong increase in the thermodynamic data [2]. In particular the latter attracted a lot of interest [1]. Due to the comparable low T_N, many theoretical approaches including well-established CALPHAD databases, assume rather weak magnetic contributions. On the other hand, several works provided indications for strong magnetic contributions (see e.g. [1]).

In order to clarify the role of the different contributions we performed state-of-the-art first-principles techniques including *ab initio* molecular dynamic simulations [3] and spin quantum Monte Carlo simulations [4] to treat the explicitly anharmonic lattice vibrations and magnetic free energies. Using our previously developed methodology [4,5], we parameterize an effective nearest-neighbor Heisenberg Hamiltonian by tuning the exchange
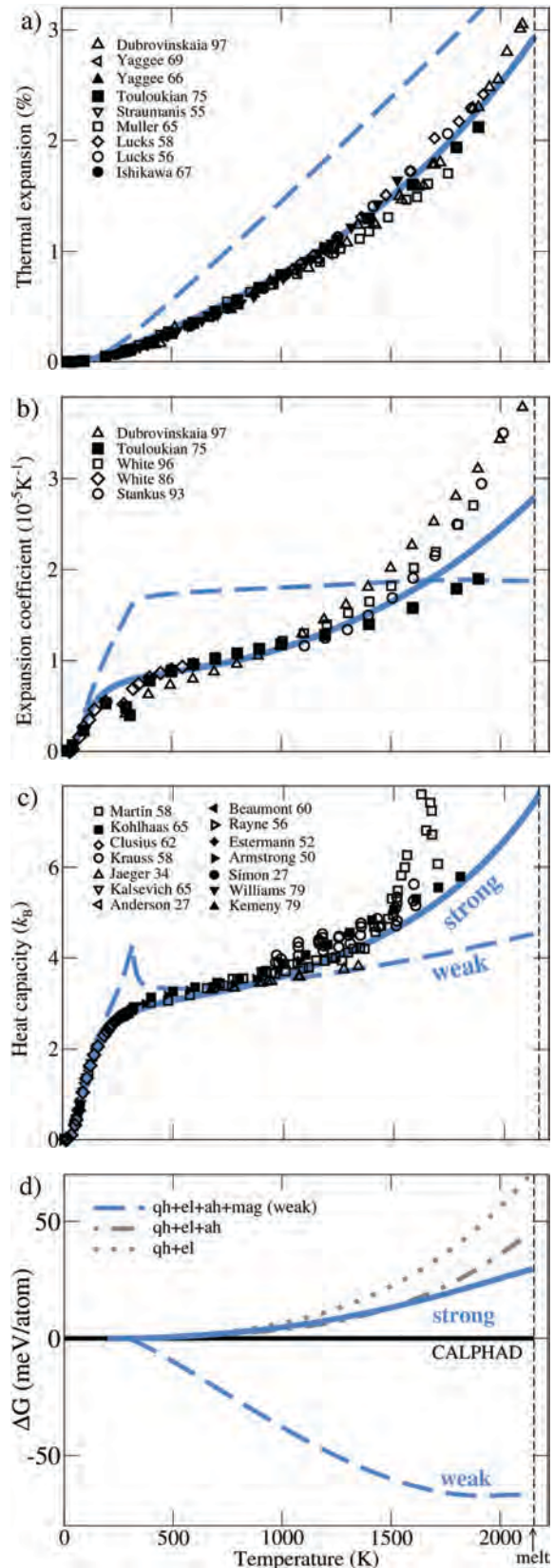
Fig. 1: *Temperature dependence of thermodynamic properties for bcc Cr: a) linear expansion, b) linear expansion coefficient, c) heat capacity, and d) Gibbs energy. Black symbols are experimental values and blue lines show our theoretical results. The dashed (solid) line corresponds to the weak (strong) coupling scenario. Vertical dashed lines indicate the melting point (2156 K). The Gibbs energy in d) is referenced with respect to values obtained from the CALPHAD approach (SGTE unary database). Additionally the dependence of the quasiharmonic and electronic (qh+el) contribution and the one of the quasiharmonic, electronic and anharmonic (qh+el+ah) contribution are shown.*

interaction to reproduce the experimental T_N = 311 K. The quasiharmonic and electronic free energy contributions have been obtained with two different DFT codes (VASP and Quantum Espresso) and yield consistent results. The anharmonic excitations have been computed for more than 30 volume-temperature points to systematically check this contribution over the full temperature range. The resulting thermodynamic properties are shown by the dashed lines in Fig. 1 and compared to the experimental data. The comparison reveals clear and consistently large deviations for all thermodynamic properties. Based on our analysis we conclude that, despite the low T_N, the picture of a weak magnetic coupling scenario in Cr is incorrect.

In fact, a number of experimental and theoretical approaches indicate that huge magnetic spin fluctuations may be present in Cr even well above T_N. As recently discussed by Jaramillo and coworkers, the origin is related to the intrinsic coupling of the SDW to a charge density wave [6]. Based on the involved electron-hole pseudo gaps shown by optical measurements, it was concluded that high energy excitations on an energy scale of ~$5k_B T_N$ are present in Cr. This coupling between charge and spin density waves can result in strong magnetic fluctuations. Jaramillo and co-workers provided an estimate of the magnetic exchange interaction of 140 meV, much larger than one would expect from T_N = 311 K (26.8 meV). Further, there are several experimental studies addressing the magnetic degrees of freedom directly. These studies indicate that Cr exhibits strong magnetic coupling effects: Spin wave excitations with energies up to 400 meV and spin wave velocities up to 1.5×10^5 m/s were found in $Cr_{0.95}V_{0.05}$ samples [7]. Neutron scattering experiments suggest strong magnetic interactions at least up to 600 K. Magnetic correlations were observed that extend over 11 bcc unit cells even at 700 K, i.e., temperatures well above the Néel temperature [1,8]. A general conclusion of all these studies is that the phase above T_N remains a highly correlated regime.

To clarify if a strong magnetic coupling provides an explanation for the observed anomalies in the thermodynamic properties, we pursued the following scenario [9]: The observed strong magnetic fluctuations are mimicked by assuming a large spin-interaction parameter in our magnetic model. More precisely the solid blue lines in Fig. 1 correspond to a value of 100 meV as compared to the 26.8 meV

belonging to the weak-coupling scenario (dashed lines). Note that all plotted dependencies for the resulting thermodynamic quantities, include again electronic, quasiharmonic, and anharmonic contributions.

The strong-coupling scenario provides a consistently good description over the whole temperature range for all thermodynamic quantities. This consistent description of materials properties is remarkable keeping in mind that the different thermodynamic observables explore rather different paths and derivatives on the complex free energy surface.

From these results we can conclude that the temperatures at which one can expect a magnetically fully disordered state are considerably higher than T_N. Furthermore, anharmonic contributions beyond the quasi-harmonic approximation are not the dominant source for the unusual thermodynamic behavior at higher temperatures. The excellent agreement with experiment up to the melting point implies that the temperature-dependent magnetic effects of bcc Cr can be accurately approximated by an effective Heisenberg Hamiltonian with strong magnetic coupling. The value of 100 meV identified here by a thermodynamic analysis is in striking agreement with a recent estimation of Jaramillo and coworkers [6], which probe the spin and charge order parameters using X-ray diffraction.

References

1. Fawcett, E.: Rev. Mod. Phys. 60 (1988) 209.

2. White, G.K.; Andrikidis, C.: Phys. Rev. B 53 (1996) 8145.

3. Grabowski, B.; Ismer, L.; Hickel, T.; Neugebauer, J.: Phys. Rev. B 79 (2009) 134106.

4. Körmann, F.; Dick, A.; Hickel, T.; Neugebauer, J.: Phys. Rev. B 83 (2011) 165114.

5. Dick, A.; Körmann, F.; Hickel, T.; Neugebauer, J.: Phys. Rev. B 84 (2011) 125101.

6. Jaramillo, R.; Feng, Y.; Lang, J.C. *et al.*: Nature 459 (2009) 405.

7. Hayden, S.M.; Doubble, R.; Aeppli, G. *et al.*: Phys. Rev. B 24 (1981) 1312.

8. Grier, B.H.; Shirane, G.; Werner, S.A.: Phys. Rev. B 31 (1985) 2892.

9. Körmann, F.; Grabowski, B.; Söderlind, P.; Palumbo, M.; Fries, S.G.; Hickel, T.; Neugebauer, J.: Phys. Rev. B, *submitted*.

Dangling-Bond Defects in Amorphous Materials

G. Pfanner, C. Freysoldt, J. Neugebauer

Department of Computational Materials Design

Defects crucially modify the electrical, optical, mechanical, and other properties of real materials. Whenever a material is processed, defects may be created or transformed. Theoretical insights into the relevant mechanisms promise to improve or even open completely new processing routes, and is therefore of great practical interest for innovation. On the atomistic scale, defects can be regarded as imperfections in the ideal crystalline order. Viable methods are nowadays available to calculate the relevant properties of such defects with highly accurate electronic-structure methods, notably density-functional theory [1]. But what if an ideal crystalline order does not exist because the material is amorphous? How can we then characterize a defect?

This conceptual question has been a guiding motif in the BMBF-funded EPR-Solar project on the dangling-bond defect in hydrogenated amorphous silicon (a-Si:H) during the past five years. a-Si:H has the largest market share in thin-film solar cells. Such thin film cells offer advantages in raw material use, production cost, availability of raw materials, and handling. The major drawback of a-Si:H-based solar cells is their limited efficiency, which is related to the inherent presence of dangling-bond (db) defects, i.e., singly undercoordinated silicon atoms. Unfortunately, the dangling-bond concentration is further enhanced by illumination (Staebler-Wronski effect), leading to a 30% relative loss in efficiency in the early lifetime of the solar cell [2].

Dangling bonds can be experimentally observed by electron paramagnetic resonance (EPR) as they contain in their neutral state an unpaired electron which aligns either parallel or anti-parallel in an externally applied magnetic field. In EPR, transitions between the corresponding energy levels are induced by microwave radiation. In the case of a-Si:H, EPR indicated a close connection of the db defect to the Staebler-Wronski effect. Despite tremendous research efforts in the past 40 years, it is still not fully understood and can be suppressed only in part. In the EPR-Solar project, leading experimental groups in EPR spectroscopy from Berlin, Munich, and Jülich joined up with the CM department of the MPIE to (figurally) shed more light on the dangling-bond defect in a-Si:H by a combination of advanced EPR measurements (multifrequency analysis, sub-µm spatial resolution, time-resolved spectroscopy) and theoretical modelling.

The EPR signal of the dangling bond consists of a broad feature corresponding to a Zeeman splitting g = 2.0055. At low magnetic fields (and thus low microwave frequencies), hyperfine satellites from the coupling to the central ^{29}Si isotope (5% natural abundance) become visible, with an average hyperfine coupling of ~180 MHz. This hyperfine coupling turns out to be 40% lower than dangling-bond-like defects in crystalline silicon (c-Si), e.g. at a Si/SiO_2 interface or in vacancy-impurity complexes. The full powder spectrum at different frequencies can be calculated from a model spin Hamiltonian
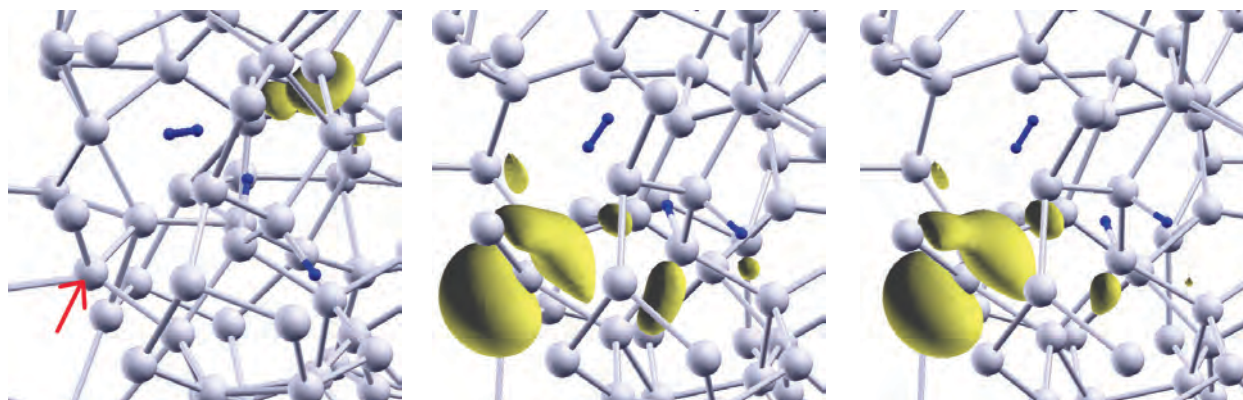

Fig. 1: *Spin density (yellow) of a dangling-bond system in a-Si:H (grey: Si, blue: H) for different strain states: -7%, 0%, and +8%. For strong compressive strain (left), the spin is no longer associated with the previously undercoordinated atom (red arrow). For tensile strain, the spin becomes more localized (right).*

with Gauss-broadened g- and hyperfine (A-) tensors. Conversely, by fitting the simulated spectrum to experiment, the hyperfine and Zeeman tensors can be extracted. The experiments carried out within the EPR Solar project revealed that the A-tensor shows an axial symmetry, whereas the g-tensor has three independent components, the lowest one being close to the g-value of the free electron (2.0023) [2].

We approached the problem of interpreting these experimental findings from two sides: first a systematic study of structure-property relationships in well-defined periodic model systems (some of them even known experimentally), and, second, by a statistical analysis of a defect ensemble in models of the amorphous structures. For the latter, defects were created at random positions in the network by abstracting a hydrogen atom from the defect-free model. The systematic study confirmed the well-known notion that the isotropic (Fermi contact) and anisotropic (dipolar) hyperfine couplings are mostly determined by the bonding geometry at the three-fold coordinated db atom: flat geometries lead to a dominant p-character of the dangling-bond orbital which contributes to the anisotropic, but (for symmetry reasons) not directly to the isotropic coupling. Tetrahedral geometries, on the other hand, admix an s-character and show larger isotropic, but lower anisotropic coupling. However, this effect is strongly overlaid by the effect of delocalization away from the central atom [3], which could not be observed in older cluster calculations. In c-Si, the delocalization correlates with the geometry since the orbital character determines the energetic position within the band gap (additionally altered by nearby impurities), and the energetic proximity to the valence band leads to a delocalized defect state. The g-tensor, on the other hand, is only weakly modified by geometrical variations and stays almost perfectly axial in all considered c-Si systems.

These fundamental mechanisms are also active in the amorphous matrix, but their relative importance varies depending on the specific surroundings of the defect. Surprisingly, delocalization is more important in the amorphous state despite the larger band gap and larger effective masses of the bulk material: apparently, the distorted geometries foster an electronic coupling to nearby fully coordinated atoms. These geometric distortions also explain the loss of symmetry in the g-tensor: in contrast to the hyperfine coupling, which is exclusively determined by the spin density and hence the orbital character at the dangling-bond atom, the g-tensor beyond the free-electron value (Δg) arises from induced spin currents, which sensitively react to disorder in bond lengths and bond angles. Quantitatively, our defect

ensemble reproduces well the peak values of the g-tensor distributions, with some overestimation of the variance [4]. For the hyperfine tensor, we demonstrated that the delocalization explains in part the experimentally observed red-shift. The remaining discrepancy is most likely due to a somewhat oversimplified selection of the theoretical defect ensemble: in experiment, defects will not appear at random positions, but will be filtered by thermodynamic equilibration and kinetic effects in the creation and diffusion. A broad analysis of various aspects of the amorphous model systems underpinned our conclusion that the dangling-bond defect in a-Si:H is a 'network defect' that cannot be conceptually separated from its immediate surrounding [5]. Its electronic, geometric, and spectroscopic characteristics sensitively react on variations in the environment as e.g. induced by strain (see Fig. 1). Dangling bonds can even merge into the network under moderate compressive strain, developing a floating-bond-type (overcoordinated) defect by forming a new bond.

Our strategy of combining a systematic analysis to discover fundamental mechanisms with a statistical modelling of a representative ensemble to capture the natural variability of disordered systems can be applied also to other cases. For instance, corrosion products of structural materials (transition metals) are typically off-stoichiometric, disordered, and sometimes even amorphous compounds consisting of cations in different oxidation states, and oxide and hydroxide anions (not to talk about anion vacancies). The ion transport across these films determines critically the speed of on-going corrosion, and it is ultimately linked to the diffusion of point defects. Therefore, disordered oxides will be addressed within an upcoming DFG Forschergruppe (in preparation).

References

1. Freysoldt, C.; Grabowski, B.;Hickel, T.; Neugebauer, J.; Kresse, G.; Janotti, A.; Van de Walle, C.G.: "First-principles calculations of defects in solids", Rev. Mod. Phys., *submitted.*

2. Fehr, M.; Schnegg, A.; Lips, K.; Rech, B.; Astakhov, O.; Finger, F.; Pfanner, G.; Freysoldt,C.; Neugebauer, J.; Bittl, R.; Teutloff, C.: Phys. Rev. B 84 (2011) 245203.

3. see e.g. Fritzsche, H.: Annu. Rev. Mater. Res. 31 (2001) 47.

4. Pfanner, G.; Freysoldt, C.; Neugebauer, J.: Phys. Rev. B 83 (2011) 144110.

5. Pfanner, G.: "The dangling-bond defect in silicon. Insights into electronic and structural effects from first-principles calculations of the EPR parameters", PhD thesis, Universität Paderborn (2012). Also: Pfanner, G.; Freysoldt, C.; Neugebauer, J.; Jarolimek, K.; Inam, F.; Drabold, D.: *to be submitted.*